SURFACTANT-MEDIATED GROWTH OF MESOPOROUS AND NANOSTRUCTURED FILMS

Corrected Copy

Thesis submitted for the degree of
DOCTOR OF PHILOSOPHY (SCIENCE)
in
PHYSICS

by

PARAMITA CHATTERJEE

Department of Physics
University of Calcutta
2014

To my father

Acknowledgement

The tenure of my thesis work which is one of the most happening period in my life have been greatly influenced by many people who have contributed either directly or indirectly to the making of this thesis. Before listing some of them, I would apologize to the persons whose names are not mentioned here. The selection made here is not meant to be valuing and omissions are inevitable due to space minimization.

Firstly I would like to express my heartfelt gratitude to my supervisor Prof. Satyajit Hazra for his sincere guidance, inspiration and patience from the very early stage of this research as well as giving me extraordinary experiences through out the work. He has taught me, both consciously and unconsciously, how good experimental physics is done and how a ordinary presentation can be made extraordinary. His intuitive but logical approach towards experiments and the critical view of the scientific observations have been of immense help in the development of my overall scientific thinking and attitude toward research problem. His moral support through thick and thins has been very hearting and inspiring. It is an honor for me to work with such a wonderful personality.

I would like to extend my sincere thanks to Prof. Bikas K Chakrabarti, Director of our Institute for providing the necessary facilities for my research work. I owe many thanks to the former Directors of our Institute Prof. Bikash Sinha and Prof. Milan K. Sanyal, for giving me the opportunity to work in the institute and utilize its resources.

I would like to acknowledge Prof. Manabendra Mukherjee for his constant support in using the Dynamic light scattering and X-ray Photoelectron Spectroscopy instrument. I wish to thank Prof. Alokmay Datta for his support in using the Ultraviolet-visible spectroscopy unit. I gratefully thank Prof. Satya Ranjan Bhattacharya, Prof. Tapas K.

Chini, Prof. Biswarup Satpati, Prof. Debabrata Ghose, Prof. Mrinmay K Mukhopadhyay, Prof. Purushottam Chakraborty, Prof. Sangam Banerjee, Prof. K.S.R. Menon and Prof. Satyaban Bhunia for their valuable questions and suggestions at the time various presentations of my work.

It is my pleasure to specially acknowledge Jayanta-da for helping me to figure out solutions for a number of lab-related as well as everyday-life problems. I would like to thank Ishani, Mala and Sruti who were always ready to lend a helping hand. The times spent in the lab and during the trips to DESY with Ishani and Mala will be memorable for me. I am extremely thankful to Subarna-di, Subhrangshu-da, Rupak-da, Maidul-da, Suman-da, Mojammel-da, Deba-da, Puneet-da, Smita-di, Mrinal-da, Sirshendu-da and Biswajit-da for their invaluable help and cooperation through all these years. I am also benefited through all these years by many insightful conversations with my batch mates Safiul, Bishnu, Sanjay, Abhisakh and Nupur-di. I also take the opportunity to thank Manjula, Tanusree, Pabitra-da, Jayanta, Shyamal, Sumona, Arpan, Suvankar and all others who remained very cooperative during my work in this division.

I thankfully acknowledge Mr. Susanta Banerjee, Mr. Avijit Das, Mr. Goutam Sarkar, Mr. Souvik Banerjee, Mr. Syamaprasad Mallik and Mr. Subir Roy for their help in solving different technical difficulties. I am thankful to Mr. Mukul Chandra Das and Mr. Subhasish Sanyal for their support in official matters. I will be ever thankful to Mantu-da, Haren-Da and Gobardhan-Da for their wholehearted support in several non-academic routine matters.

Apart from my divisional members I would like to extend my appreciation to Prof. PMG Nambissan and Soma Roy for their valuable help in using the the UV-Vis measurement. I wish to thank Prof. N. Roy for helping me in Contact angle measurement. I thankfully acknowledge the Electron Microscope Facility, SINP for the TEM facility and Mr. Pulak Roy for his contributions in TEM measurements. I would also like to extend my thanks to the Unit on Nano Science and technology, IACS, Kolkata, School of Materials Science and Engineering, Bengal Engineering and Science University, Shibpur and Center for Research in Nanoscience and Nanotechnology, University of Calcutta, Kolkata for providing me the TEM facility.

I will be ever thankful to Dr. H. Amenitsch, SAXS bamline, Elletra, Italy and Dr. Stefan. V. Roth, MiNaXS beam line (P03), PETRA III, Deutsches Elektronen-Synchrotron (DESY), Germany for my initial training in beamline experiments and

valuable discussion with them regarding my research problem. Financial support received under Indo-Italian POC to carry out GISAXS experiments at Elettra and Saha Institute of Nuclear Physics under the DST-DESY project to carry out GISAXS experiments at PETRA III are thankfully acknowledged

It is a pleasure to express my gratitude wholeheartedly to Prof. Alain Gibaud for valuable discussions with him regarding my research problem and results and also had the privilege of learning the fundamentals and applications of *evaporation-induced self assembly* (EISA) process.

The main motivations behind this effort has came from my family. I would like to express my deepest thanks to my family members for their continuous and remarkable support which helped me to maintain the interest in my research. Their cheerful faces have motivated me to overcome difficult times. Last but not the least I would like to specially acknowledge my husband Sudipta for staying with me in every crisis and give his complete support which brought my research to a fruitful conclusion. Without the care and love of my family and husband I could never have completed my work. This thesis mostly owes to them.

Paramita Chatterjee

Saha Institute of Nuclear Physics

Kolkata

August, 2014

Contents

1

Introduction

Nanostructured materials, having unique physical, chemical and biological properties, are becoming a subject of multidisciplinary research area. Such properties of the nanostructured materials are mainly arise from collective behavior of low-dimensional objects (nanoobjects) in a matrix and essentially depend on the size, shape and arrangement of the nanoobjects in the matrix. Nanoobjects are essentially materials whose dimension in one, two or in all three directions is reduced to nanometer length scale and accordingly can be nanolayers (2D), nanowires or nanorods (1D) and nanoparticles or nanodots (0D). The individual behavior or properties of such nanoobjects are sometime completely different from those of bulk one.[1,2] It is thus crucial to control the size and shape of the nanoobjects to get desire individual properties and also their organization to get desire structure and collective properties. Different synthesis and processing techniques have been developed in this direction ranging from lithographic techniques to chemical methods, among which, surfactant-mediated growth of nanostructured materials is now becoming a quite useful technique.

The self-assembly of surfactants is an elegant *bottom-up* method for fabricating nanostructured materials.[3] The self-assembly process can be defined as the spontaneous organization of individual components into an ordered structure without human intervention. In fact nature has fully evolved this self-assembly process to build up highly sophisticated macromolecules. These self assembled systems are further used as structure guiding media i.e., template. Similar to nature, the aggregates of surfactants and block copolymers such as, micelles, microemulsions, vesicles, lyotropic liquid crystalline

phases or the mesostructures offer a huge variety of microphase texture which may be used as structural templates. Templating is one of the most important techniques for the controlled synthesis of nanostructured materials. This powerful tool uses a pre-existing guide with desired nanoscale features to direct the formation of nanomaterials into forms that are otherwise difficult to obtain. As a result, templated synthesis is capable of producing nanostructures with unique structures, morphologies and properties. A wide variety of synthesis techniques are utilized to produce nanomaterials using template-based methods. In our research work, attention is mainly focus on synthesis of mesoporous oxides with well defined and ordered porous structure using surfactant or copolymer micelles as templates through sol-gel processing[4] and formation of metal nanoparticle templated by block copolymer micelles.[5] The micelles (or reverse micelles) of uniform size and shape in liquids can organized themselves in inorganic matrix to form interesting surfactant-templated mesostructures which results in mesoporous structure after removal of the surfactant. On the other hand, surfactants can act as both reducing and stabilizing agents which can be used to form metal nanoparticles of different shape and size or nanostructured materials.

In this chapter, we will first give an overview of surfactant and its self assembled structures. Subsequently we will give a brief review on the formation of mesostructured films on silicon surfaces and also a brief review on Si surface. Surfactants, which can act as both reducing and stabilizing agents to form metal nanoparticles, will be discussed next. The motivation behind the present research work and the outline of the thesis are included at the end of this chapter.

1.1 Surfactants and micelles

Surfactants are amphiphilic molecules, containing at least one hydrophilic (water-loving) head group and one hydrophobic (water-hating) tail group as shown in Fig. 1.1. The hydrophilic head group will be an ionic or highly polar group that can impart some water solubility to the molecule. The hydrophobic region of a surfactant is typically composed of one or more hydrocarbon chains that are either linear or branched. This portion of the surfactant has a weak interaction (in the form of dispersion forces and

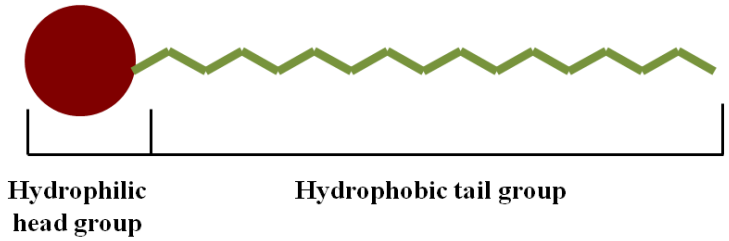

Figure 1.1: Example schematic of surfactant molecule.

hydrogen bonding) with water molecules in an aqueous environment. Based on the nature of the hydrophilic head group, surfactant can be classified in four categories: anionic, cationic, zwitterionic and non-ionic. The cationic surfactants are molecules with positively charged head groups. These surfactants are usually made of long-chain amines and long-chain ammonium salts. Anionic surfactants are molecules with negatively charged head groups. Examples include carboxylic acid salts and sulfonic acid salts (sulfonates). Zwitterionic surfactants are molecules with head groups containing both a positive group (ammonium) and a negative group (carboxylic or sulfonate). Nonionic surfactants are molecules with neutral head groups, such as polyethylene oxides.[6,7]

As the name surfactant (short for surface active agent) implies, the molecules are active at a variety of surfaces, especially at air-liquid and liquid-liquid interfaces. They have tendency to change their interfacial properties dramatically, such as surface tension, interfacial tension, surface diffusion etc. which are determined by unique intermolecular interactions: the hydrophobic interactions between the tail groups, and the hydrophilic and/or the electrostatic interactions between the head groups. Moreover, surfactant molecules play a critical role in a wide range of self-assembly phenomena often called micellization: a spontaneous and reversible process for the formation of micelle. Micelle is colloidal-size object with 2-20 nm diameter, formed in a cooperative process. In aqueous solution part of the initially added surfactant is adsorbed onto the air-liquid interface to significantly reduce the surface energy and forms an adsorbed monolayer. Since the space for the monolayer formation is limited at the surface, the rest of the molecules remain in the solution as a free form of molecules (monomers). At a certain concentration of surfactant, called critical micellar concentration (cmc), the surfactant molecules start to self-associate into micelles which is driven by the hydrophobic interac-

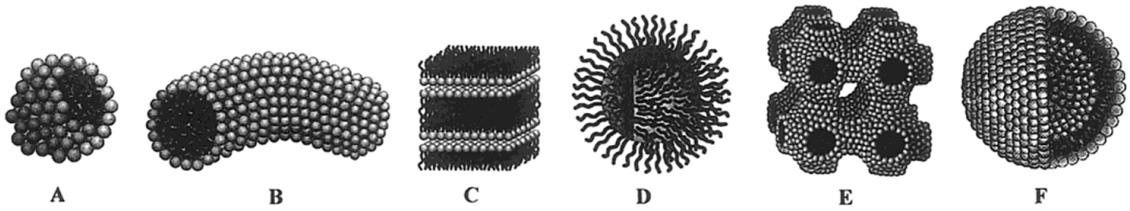

Figure 1.2: Micellar structures (A) sphere, (B) cylinder, (C) planar bilayer, (D) reverse micelles, (E) bicontinuous phase, (F) liposomes. Taken from literature.[9]

tion that arises from the tendency of water molecules to reduce contacts with surfactant alkyl chains. Micelles are thermodynamically stable species that are in chemical equilibrium with free surfactants. Micellization is actually a process toward the delicate balance between the attractive and repulsive intermolecular forces. Attractive forces directly act on surfactant molecules to bring them close together, while repulsive forces act against the molecules. Hence, the former can be defined as the driving force for the micellization, and the latter as the opposition force. No strong chemical bond such as a covalent bond is involved during this process. More specifically, the driving force for this process is usually the hydrophobic attraction and the opposition force is the electrostatic repulsion and/or solvation force. First, the long-range hydrophobic force acts as a main force to bring the surfactant molecules close together. As the process continues, the opposition forces such as electric double-layer repulsion or hydration forces start to impose. These forces originate from the charge-bearing or hydrated head groups, and are relatively short-range forces compared with the hydrophobic interaction. These two types of forces are variable as a function of intermolecular distance, but in opposite ways. Consequently, the attractive and repulsive forces should be balanced at a certain point of the process. Micelles are formed at this point, and the further growth of micelles is prevented. But, since there are no chemical bonds involved, the surfactant monomers in the micelles are free to be exchanged with the monomers in the bulk solution, depending on their molecular dynamic properties.[6,8]

Depending on many experimental parameters, spherical micelles, cylindrical micelles, hexagonally ordered crystals, cubic crystals, lamellar phases, inverse micelles, and inverse micellar liquid crystals can be formed as shown in Fig. 1.2. However, the change

from one phase to another is not random, but rather follows a consistent pattern. For example, as the surfactant concentrations are increased, the phases go through spherical micelles, rod-like micelles, hexagonal, cubic, and lamellar phases. There are many other parameters such as, surfactant chain length, addition of cosolvents, addition of salts and ionic species, etc. which are responsible for the transformation of micelle from one phase to another.

1.2 Mesostructured films

The development of porous materials in different forms, like bulk, fibre, powder, thin film etc. with large specific surface areas is currently an area of extensive research, particularly with regard to potential applications in areas such as adsorption, chromatography, catalysis, optics, sensor technology, gas storage, insulation coatings, ultra-low density materials, etc.[9] According to the classification made by IUPAC, porous materials can be grouped into three categories, depending on their pore diameter: microporous ($d < 2$ nm), mesoporous (2 nm $< d <$ 50 nm), and macroporous ($d > 50$ nm) materials.[8–10] Well-known members of the microporous class are the zeolites, which provide excellent catalytic properties by virtue of their crystalline aluminosilicate network. However, their applications are limited by the less accessibility of pores due to relatively small pore openings. This motivation sparks the proliferation of mesoporous materials.[9,10] Most of the studies about mesoporous materials have been performed on the bulk and powdery forms. On the contrary, far less attention has been paid to the thin film forms of this class of materials. This is probably because the synthetic techniques of thin films have not been well developed till now.[11] However, it is obvious that the thin films of mesoporous materials are highly interesting because of their great range of potential applications in molecular detection, membrane separation, environmental science, medicine, catalysis, optics and other still evolving fields of activities.[12] In this section, first we will briefly introduce the mesoporous thin films, which can be derived from mesostructured thin films and then present a literature review about the structural evolution of the films depending upon different processing parameters (i.e., pH, concentrations, temperatures, nature of the solvent, counterions, aging time).

Generally, the mesostructured films can be classified into two categories - random mesostructured films and ordered mesostructured films. Random mesostructures can be made by a variety of methods like, leaching a phase separated glass, anodic oxidation of thin metal foils in an acidic electrolyte, radiation-track etching and sol-gel processing whereas, ordered mesostructures are made with a combination of using self-assembled surfactants as template and simultaneous sol-gel condensation around the template. The pores in random mesoporous films could not be fully opened and as a result reagents and products could not easily pass through the pores, leading to coking in catalytic processes. Moreover, the pore sizes are widely distributed, and the arrangement of pores is disordered. On the other hand, ordered mesosporus films have uniformly sized and shaped pores with a very large pore volume (up to 70%) and very high surface area. Among all the mesoporous oxide films, silica film has a more structural and thermal stability which is very useful for the improvement of the circuit performance in semiconductor industry.[13] Before focus on the details of the surfactant mediated ordered mesoporous silica films, let us discuss about the synthesis of random mesoporous silica films using sol-gel process and its structural dependency on different solution parameters.

1.2.1 Sol-gel derived mesostructured silica films

The sol-gel process is a very well-known, remarkably versatile wet chemical route for the synthesis of mesoporous silica films.[14–16] The process offers many advantages for the fabrication of porous silica films including ease of compositional modifications, customizable microstructures at the chemical solution stage which results many unusual properties such as an adjustable refractive index, a high porosity, a low thermal conductivity, a low dielectric constant, and a high laser damage threshold.[17,18] Therefore, the films have been finding more and more applications in various areas such as optics, microelectronics, membranes and sensors.

The sol-gel process is primarily based on the hydrolysis and condensation reaction of organometallic compounds in alcoholic solutions to form an oxide network.[15] A sol consists of a liquid with colloidal particles which are not dissolved, but do not agglomerate or sediment whereas gel is a interconnected, rigid network formed by simultaneous

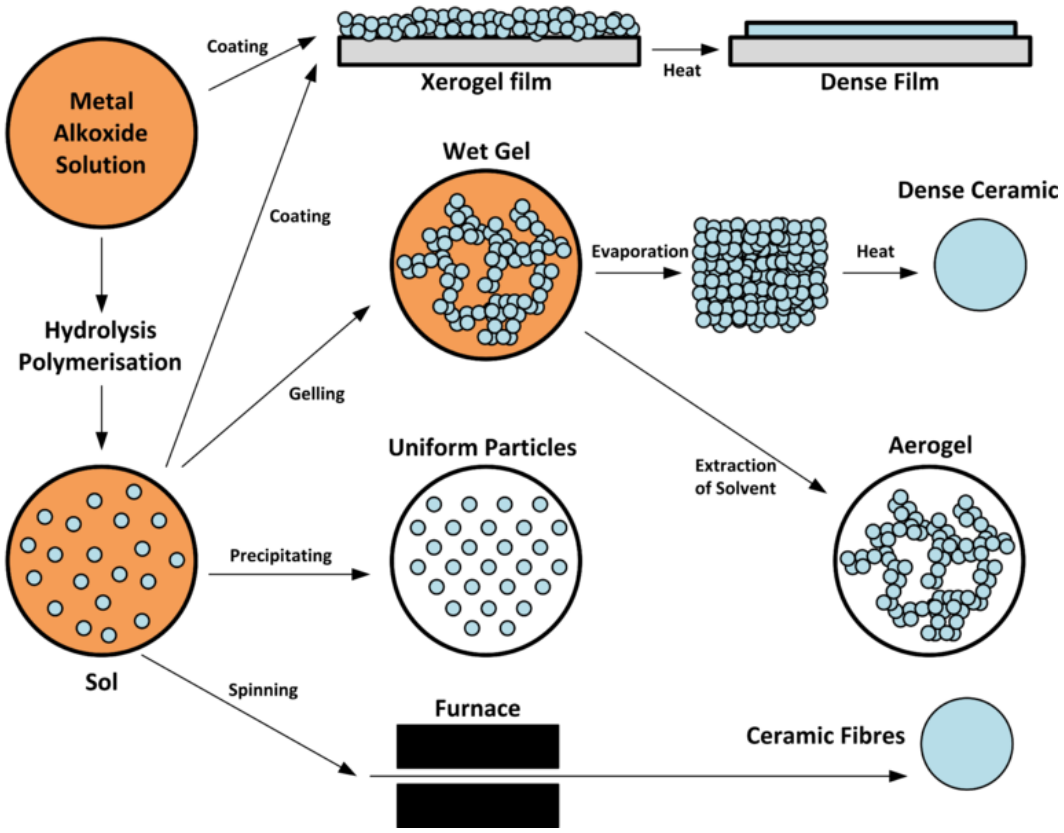

Figure 1.3: Sol-gel technology scheme.

hydrolysis and polycondensation reaction of the organometallic precursor with pores of submicrometer dimensions and polymeric chains whose average length is greater than a micrometer. For thin film production, the initial solution or sol containing the precursor is used to coat a substrate by a dip-coating or a spin-coating technique. The resulting film is dried at a temperature near room temperature to preserve the film porosity.[16,17,19,20]

Lots of work have been reported about the sol-gel kinetics of silica precursor and the effects of hydrolysis and condensation reactions on the sol-gel derived mesoporous structure.[14,21–24] Boilot et al. have studied the kinetics and mechanisms of the hydrolysis-condensation reactions, starting with tetraethyl orthosilicate (TEOS).[25] The polymerization is influenced by many experimental parameters like, the starting alkoxides, the use of gel precursors with different chain length, the variation of pH value which modify hydrolysis and condensation rates and the H_2O content. Garrido et al. have studied

the simultaneous effect of pH, ethanol/silica and water/silica molar ratios, and synthesis temperature on gelation time, textural and structural properties of sol-gel silica material.[26] They have observed that gelation time decreases with increasing temperature, water/silica molar ratio and pH. The time also decreases with lower ethanol/silica molar ratio. The porous texture is also affected by the synthesis conditions. Depending on solution pH value the sol-gel process can be classified into two different routes.[27] When the reaction takes place under basic condition larger particles with the size up to several hundred nanometers can be generated as long as the growing particles are stabilized by the repulsive surface interaction. On the other hand, a network structure with less branching points is formed when the reaction is carried out in an acidic condition. Thus, the reaction in the acidic condition results in chain extension consisting of small primary particles, which significantly differs from the basic system. But the sol-gel thin film processing differs from bulk gel processing.[16] Because drying stage overlaps the aggregation/gelation and aging stages establishing a brief time for further condensation reactions or ordering to occur. The fundamentals of sol-gel silica films prepared by dip-coating and spin-coating process have been studied in details by different researchers.[16,17,19,20] From their reports it is clear that the characteristics of sol-gel silica films are determined by a large number of processing parameters and it is important that the effects of these parameters should be well understood to make sol-gel a reliable and practical technology for device fabrication.

Chaudhury et al. have prepared sol-gel derived thin films from different compositions at low pH (∼2.0) containing varying concentrations of ethanol at constant water (H_2O)/silica ratio (R = 4) to investigate the influence of ethanol concentration in the microstructure of the sol-gel derived films.[28] They have found that increased concentrations of ethanol improved the quality of films. The effects of water on structure of acid-catalysed sol-gel silica films have investigated by Horowitz et al. [29] They have observed that the thickness, shrinkage, porosity and pore sizes all decrease with increasing R value (ratio of H_2O/silica). Moreover, increasing the amount of water yields films of higher homogeneity and surface uniformity along with finer texture and less tensile stress. Pantano et al. have also shown that the increasing H_2O/silica ratio exhibit

increasing density of the film.[30] Consequently, the amount of film shrinkage observed during thermal treatment in N_2 or NH_3 was decreased with increasing H_2O/silica ratio. Moreover, the microstructure of the films such as pore size and porosity can be tailored by controlling the molar ratio of inorganic tetraethyl orthosilicate (TEOS) and organic methyltriethoxysilane (MTES), shown by Pita et al.[18] They have reported that surface modifications of the films ensure that the films contain minimal silanol groups and render the films much more resistant to the moisture absorption, so the dielectric constant of the films can be kept low. The effect of annealing temperature on the structural and dielectric properties of the films have been systematically investigated by Goh et al.[13] With the increase of annealing temperature, porosity in the film increases while the dielectric constant of the films decreases. However, the pore size of the films does not change very much with annealing temperature in the range 300 to 450°C. Cheong et al. have also shown that the post-deposition annealing temperature has a great effect on the physical, chemical and electrical properties of the sol-gel films.[31] It is observed by Zhang et al. that the post treatment remarkably strengthens the structure of the porous silica films.[32] They have prepared silica films from both the base and base/acid two step catalyzed sols and then annealed in the mixed gas of ammonia and water vapor. From the results they have proposed that the strengthening mechanism is attributed to the cross-linking of silica particles by randomly branched or/and entangled linear chains in the sols, more Si-O-Si bonds formed by the mixed gas treatment and structural changes in the silica films. The stability of thin silica films in solution has been evaluated as a function of drying time and drying conditions (i.e., relative humidity) by Khramov et al.[33] They have found that the films dried for an extended period of time under low relative humidity are stable for several days.

1.2.2 Surfactant mediated mesostructured silica films

The preparation of mesostructured silica films took its origin from the pioneer works by Mobil scientists in the early 1990s on surfactant-templated materials [35,36] and was first reported by Ozin's and Brinker's groups.[4,37–39] In 1999, Brinker et al. reported a new approach, which resulted in crack-free, crystalline highly ordered mesostructured

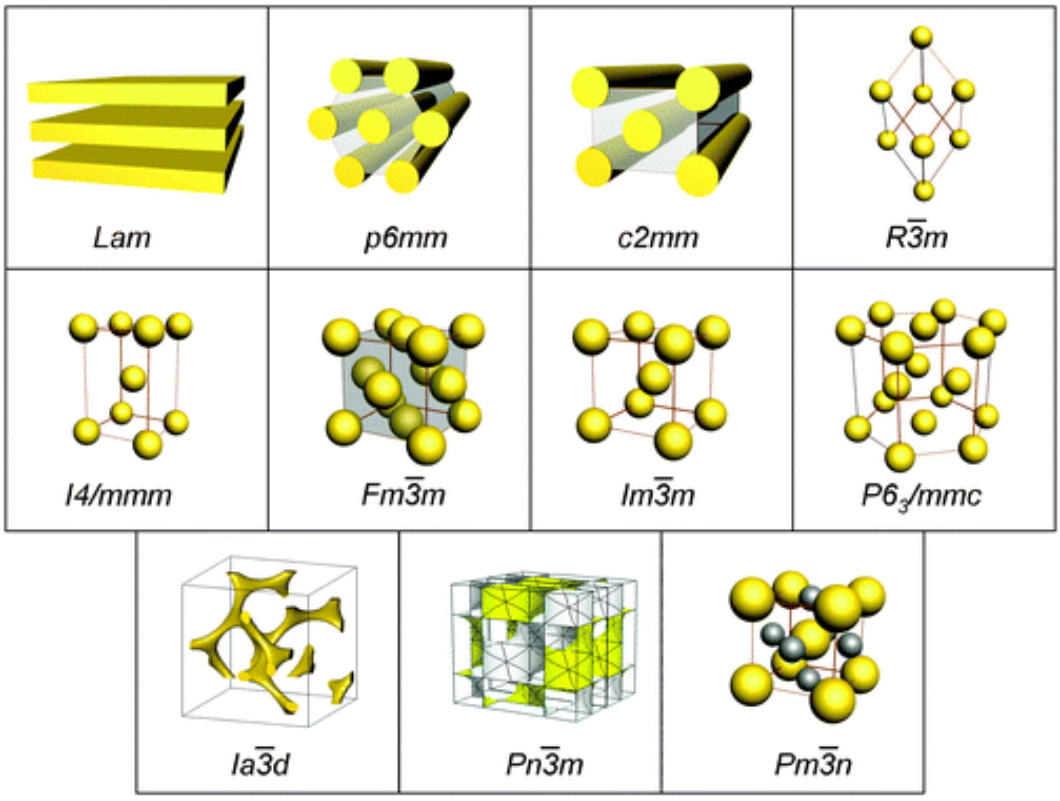

Figure 1.4: 2D (Lam = lamellar, $p6mm$, and $c2mm$), 3D ($R\bar{3}m$, $I4/mmm$, $Fm\bar{3}m$, $Im\bar{3}m$, $P6_3/mmc$, and $Pm\bar{3}n$) and bicontinuous ($Ia\bar{3}d$ and $Pn\bar{3}m$) pore structures obtained from silica mesostructured films.Taken from literature.[34]

thin films with a tunable film thickness on the scale of only several nanometers, called *evaporation induced self-assembly* (EISA).[4,39] Since then, extensive works involving various sol-gel precursors combined with various surfactants have been reported for a large number of mesostructures with mesopores dimensions ranging from 2 to 20 nm. This synthesis route presents several advantages such as the versatility of processability, a short mesophase formation (a few minutes) and the fact that it gives access to a large variety of mesophases. Moreover, this process permits control of the final mesostructure by adjusting both the chemical parameters (like, initial sol composition, pH, aging time) and the processing parameters (like, partial vapor pressures, convection, temperature).[12,40] Starting with homogeneous hydro-alcoholic solutions of soluble silica sources (monomeric and oligomeric silicic acid species), surfactant (initial surfactant concentrations $c_0 << cmc$) and, optionally, other organic and inorganic species, the preferential evaporation of alcohol that accompanies spin-coating, dip-coating, ink-jet

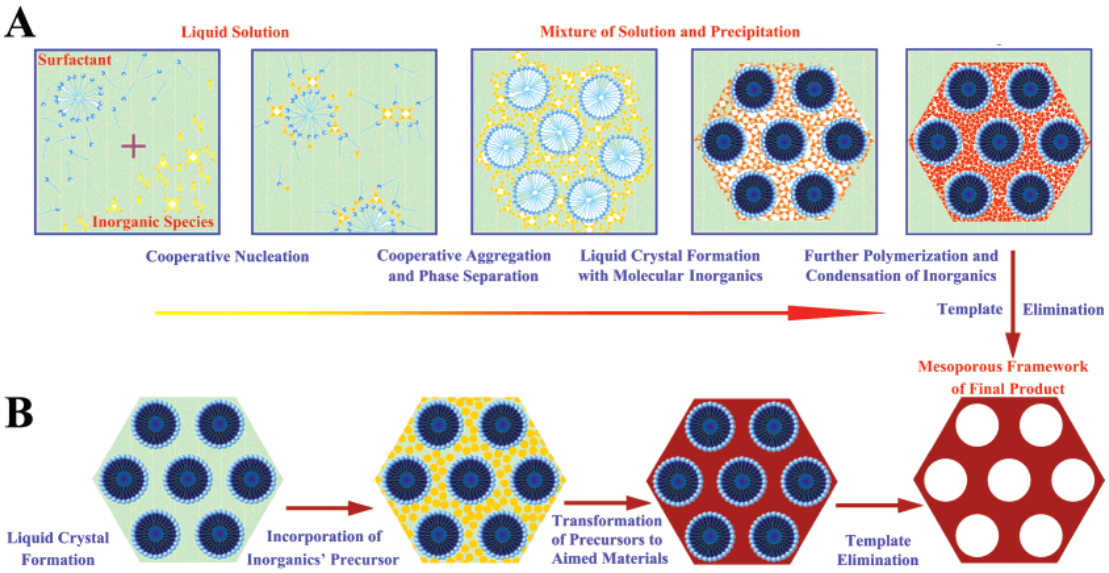

Figure 1.5: Two synthetic strategies of mesoporous materials: (A) cooperative self-assembly; (B) *true* liquid-crystal templating process. Taken from literature.[41]

printing, aerosol deposition, or selective dewetting drives silica/ surfactant self assembly into uniform or spatially-patterned thin-film mesophases. Through subsequent heating or exposure to catalysts or light or solvent extraction these films can be processed into mesoporous materials of potential utility for a diverse range of applications such as sensors membranes, catalysts, waveguides, lasers, nano-fluidic systems, molecular valves and low dielectric constant insulators (so-called low κ materials). This EISA process is useful because it enables rapid, efficient integration of well-defined nanostructures into microelectronic devices and microsystems, using readily available processing methods.[40] A large variety of mesoporous materials with different mesostructures like, 2D-hexagonal (of space group $p6mm$), 3D-hexagonal ($P6_3/mmc$), 3D cubic ($Pm\bar{3}m$, $Pm\bar{3}n$, $Fd\bar{3}m$, $Fm\bar{3}m$, $Im\bar{3}m$), bicontinuous cubic ($Ia\bar{3}d$), etc. and compositions (silica, metal oxides, metal sulfides, metals, and even polymers and carbons) as shown in Fig. 1.4 can be synthesized using this process.[34,41,42]

A large number of studies have been carried out to investigate the formation and assembly of mesostructures on the basis of surfactant self-assembly. Two main pathways, *true* liquid-crystal templating (LCT) process and cooperative self-assembly (CSA), seem to be effective in the synthesis of hybrid nano-organization of inorganic structures

with surfactants (shown in Fig. 1.5).[12,41] In LCT process the inorganic phase condenses around a stabilized surfactant mesophase. On the other hand, in CSA process surfactant molecules and inorganic species combine in a first step to form hybrid intermediate entities that behave as independent surfactant species-building blocks of hybrid structures. In practice, it is most likely that a combined effect of both mechanisms governs the synthesis of such hybrid materials, depending on the chemical and processing critical parameters for a given system. Further, mesostructured silica films can be synthesized by either the alkaline route or the acidic route.[43,44] In the alkaline route, surfactants (denoted as S^+) and silicates (denoted as I^-) organize by strong S^+I^- electrostatic interaction. On the other hand, the acidic route is interesting in offering versatile morphologies. In this route, the surfactant(S^+) - silica(I^+) interaction in $S^+X^-I^+$ is mediated by the counterion X^-. This interaction is weaker; thus, it can usually lead to many topological constructions.

In most cases, films were synthesized from a mixture containing the cationic surfactant cetyltrimethylammonium bromide (CTAB) and a silica sol prepared by hydrolysis of an ethanolic solution of alkoxysilane in acidic media. During the drying process, which implies rapid removal of solvents, the growth of micellar ordered domains progressively takes place from the air-sol interface to the interior of the films. In these dynamic conditions, the mesostructurization mainly depends on the chemical composition of the deposited solution and on the evaporation conditions of solvents. By simply changing the surfactant to silica ratio, different micellar structures lamellar, 2D-hexagonal, 3D-hexagonal, and cubic have been stabilized by the silica network formed at the gelation. Using CTAB as the structure-directing surfactant, Brinker et al. have characterized *in-situ* the evaporation induced self-assembly of a homogeneous CTAB-silica solution into a highly ordered surfactant-templated mesostructure.[45] They have monitored formation of a 2D-hexagonal ($p6mm$) thin film mesophase with cylinder axes oriented parallel to the substrate surface from an incipient lamellar mesophase through a correlated micellar intermediate. Boilot et al. have observed evolution of different mesostructures and the domains of stability of these structures in silica films depending on the CTAB/silica ratio and the aging time of the initial sol.[46] Due to successive drying and calcination

steps, these phases result from the unidirectional distortion of three micellar structures: the 3D-hexagonal ($P6_3/mmc$) structure formed by dense packing of spherical micelles, the cubic ($Pm3n$) structure, and the usual 2D-hexagonal ($p6m$) structure composed of cylindrical micelles. They have also shown that partial substitution of the silica precursor tetraethyl orthosilicate (TEOS) by an organosilica precursor, such as methyltriethoxysilane (MTES), leading to a significant modifications of the domain of stability along with reduction of the microporosity in the silica walls of mesostructured CTAB-silica film.[47] The effects of sol aging conducted before deposition, on mesostructured silica films organization has been also reported by Liu et.al.[42] It was observed that during the sol aging without stirring, there exists a disorder-order-disorder transition in mesostructured films with the increase of sol aging time. Further, understanding the elementary kinetics in the CTAB-silica system in acidic media, they were especially interested in developing the relationship of counterion binding and morphology of CTAB-silica mesostructured materials.[43] They have synthesized mesostructured silica films with well-ordered hexagonal structure by using various acid sources HX and found that the various X^- counterions follow the lyotropic series in their binding ability to the cationic micelles. The very important role of water from external humidity in the texturation of the hybrid mesostructure has been demonstrated by Sanchez et al.[48] They have obtained poorly ordered, 2D-hexagonal or 3D-cubic final structures depending on the relative humidity (RH), in agreement with the general physico-chemical laws of CTAB mesophases. Richardson et al. have examined the effect of different solution parameters like, concentrations of the silica precursor and the surfactant template (CTAB), water and the solution pH in the spontaneous formation of CTAB-templated mesostructured silica films.[49] Moreover, understanding the role of alcohol on those structures and their control is very important, as it is shown that alcohol can act as a cosolvent or cosurfactant and can modify the mesostructure accordingly.[50,51] Despite a large number of works on structural variation of CTAB-silica mesostructured films depending on different solution and processing parameters only a limited number of works has been carried out to study the influence of substrate surface on structure and ordering of mesostructured films. Klotz et al. have studied how the ordering of mesostructured films depends on

the surface roughness and surface forces.[52] Stucky et al. and Ozin et al. have shown the growth and formation of mesostructured silica film on hydrophilic mica and hydrophobic graphite surfaces, respectively.[53,54]

1.3 Substrate surface

Among different semiconductor substrates, Si is probably the most studied substrate for its versatile use in device fabrication. It is known that, substrate surface condition can be modified through different ways; by passivating with foreign atomic layer (such as H, Br, Cl, etc.)[55–57] or by growing self-assembled monolayer (of say silane). This essentially modifies the surface free energy or polarity of the surface and accordingly, wetting-dewetting or hydrophilic-hydrophobic nature of the surface can be tuned.[55–64] To modify the substrate particularly to become a hydrophobic surface prior to film deposition scientist mainly are used to deposit a self-assembled monolayer (of say silane) on the substrate surface except few studies, where they have followed the wet chemical process to make a surface hydrophobic. Hazra et al. and Mukhopadhyay et al. have deposited octadecyltrichlorosilane (OTS) in order to make the Si substrate hydrophobic before LB film deposition.[65,66] Schwartz et al. have done HF treatment to prepare a hydrophobic Si surface.[67] In the following we will give a brief review of such Si surface.

1.3.1 Si surface: Native oxide

There are many types of silicon oxides such as thermal oxide, chemical vapor deposition (CVD) oxide, native oxide and anodized oxide. In this section attention will be paid towards mainly on growth of native oxide on Si substrate. Native oxide is the oxide that grows spontaneously on a clean silicon surface exposed in an ambient environment such as air or water. The formation of native oxide, which is inert in most solutions, passivates the silicon surface allowing the silicon to be used as an electronic material in processing and application environments. The presence of native oxide degrades the low-temperature growth of high-quality epitaxial Si film, controls precisely the thickness and quality of very thin gate oxides and gives an increase in contact resistance. The control of native oxide growth rate on Si surfaces is of great importance in the

fabrication of ultra-large scale integrated devices, especially with a decrease in pattern dimension. Consequently, the understanding of the growth of native oxide layer has received increasing attention.[68–72]

Elemental semiconductor such as Si is characterized with purely covalent bonds. Each bond contains two spin-paired electrons. When a surface is created atleast one such bond per atom is cut. A cut bond which is dangle into the environment is called a dangling bond and contains less than two electrons. The lack of electron pairing makes dangling bonds unstable. Thus a cleaved, fresh or clean surface is normally very reactive towards the atoms, molecules or particles, impinging on the surface. In case of Si surface, highly electronegative oxygen (given in Table 1.1) available in the ambient condition reacts with these bonds to saturate them and to form a very thin native oxide layer. The stable thickness of native oxide films on silicon surface in water is similar to that formed in air, ranging from 5 to 10 Å. The growth rate of native oxide films is similar for lowly and moderately doped silicon substrates. An increased growth rate is observed with high dopant concentration $> 10^{19}/\text{cm}^3$ on both n- and p-type silicon substrates. Moreover, thickness or coverage and the growth rate of native oxides strongly depend on substrate surface condition and also on the environmental conditions regarding exposure. It is thus very difficult to prepare a native oxide of certain quality.

1.3.2 Si surface: Etching

Chemical etching known as wet etching is a process for removal of silicon oxides through the dissolution in solutions. It is a key processing step in practically all silicon-based microfabrication technologies. The premier practical application of this process is in the manufacture of integrated circuits, in wafer cleaning, and in pattern delineation. Also etching of silicon oxide as a surface micromachining process is utilized in the fabrication of precision quartz and silicon based micromechanical structures, where chemical etching provides a convenient method for removing undesired surface layers, and for surface micromachining of the desired microstructures.[73,74] On the other hand, etching of silicon oxide is also important in situations where the oxides are used as the masking material and etching of the oxides can be detrimental. The spatially preferential or nonplanar

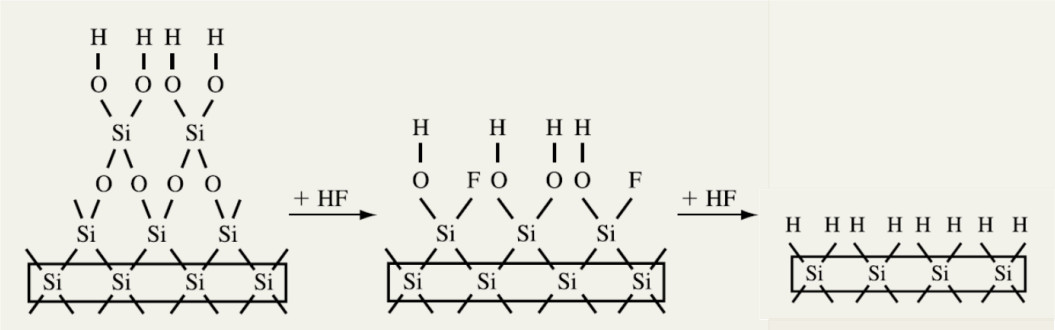

Figure 1.6: Schematic and simplified two-dimensional representation of oxide removal process followed by hydrogen passivation mechanism of Si (100) surface in HF solution.

etching caused by the effect of doping and crystal orientation, and also the surface roughness resulting from etching of Si substrate are widely utilized in device fabrications and Si technology.

Generally, chemical etching process involves multiple chemical reactions that consume the original reactants and produce new reactants. The wet etch process can be described by three basic steps - (i) diffusion of the liquid etchant to the structure that is to be removed (ii) the redox reaction between the liquid etchant and the material being etched away which entails the oxidation of the material then dissolving the oxidized material and (iii) diffusion of the byproducts in the reaction from the reacted surface. The two principal etching solution systems for Si substrate are HF solutions and alkaline solutions. This is because Si is inert in all aqueous solutions due to the formation of an insoluble surface oxide except for HF solutions or alkaline in which the oxide is soluble. In Fig. 1.6 the oxide removal by HF solution is schematically illustrated. A major difference between the two etching systems is that the etch rate of Si in HF solution is similar among the various crystalline orientations i.e., it is isotropic, whereas in alkaline solutions it strongly depends on the crystalline orientation i.e., it is anisotropic (shown in Fig. 1.7). The etch rates of the three major crystal planes vary only marginally in HF solutions.

Various chemical agents can be added to these two etching solutions so as to control the etch rate, etch selectivity, solution stability, and quality of the etched surface. It is to be noted that for chemical etching the rate of oxide removal is usually faster than the

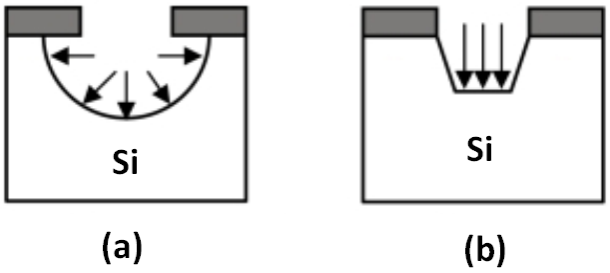

Figure 1.7: (a) Isotropic etching and (b) Anisotropic etching of Si surface.

rates for many dry etching processes and can easily be changed by varying temperature or the concentration of active species. In chemical etching process the etch rate of Si or its oxides in a given system depends on many operational parameters such as size and geometry of the sample, volume of the solution, stirring condition, ambient (light and air) condition, and etching time. Thus for a given Si material and solution composition, the etch rate may vary significantly when it is measured under different operation conditions.

1.3.3 Si surface: Cleaning

1.3.3.1 Ultrasonic cleaning

Ultrasonic cleaning is used to remove the organic contaminants from the substrate surface. In this process, the substrate is first kept into trichloroethylene or acetone (for about 10 min) and then into methyl alcohol (for about 10 min) solution separately and placed into the ultrasonic bath. It removes organic contaminants only, preserving the native-oxide layer on the surface.

1.3.3.2 RCA cleaning

The RCA (Radio Corporation of America) cleaning process is a standard set of wafer cleaning process which needs to be performed before any application in semiconductor technology. The basic procedure was originally developed by Kern and Puotinen in 1970. It involves the following chemical processes performed in sequence:
(i) removal of the organic contaminants (organic clean + particle clean),

(ii) removal of thin oxide layer (oxide strip),

(iii) removal of ionic contamination (ionic clean).

In the first step which is called SC1 (where SC stands for standard clean), a mixed solution of ammonium hydroxide [NH_4OH, Merck, 30%], hydrogen peroxide [H_2O_2, Merck, 30%] and Milli-Q water ($NH_4OH : H_2O_2 : H_2O = 1 : 1 : 5$, by volume) is boiled at 100°C for about 15 min. SC1 solution is designed to remove organic contaminants by both solvating action of the NH_4OH and the oxidizing action of the H_2O_2. The oxidizing agent H_2O_2 also forms a continuous thin silicon oxide layer on the substrate surface. Thus it is very effective in the removal of organic contaminants and as well as in the formation of continuous oxide layer. This cleaning makes the silicon surface completely hydrophilic. Moreover, the metal surface contaminants such as Au, Cu, Ni, Ag, Cd, Zn, Co and Cr are also oxidized by H_2O_2 and dissolved by the complexing effectiveness of NH_4OH.

In the second treatment step the rinsed wafer is exposed to a solution known as SC2, which is a hot mixture of H_2O_2 (30%), HCl (37%), and H_2O in the proportion of 1 : 1 : 6 to 2 : 1 : 8 by volume. This cleaning solution is designed to remove alkali ions and cations such as Al^{3+}, Fe^{3+}, and Mg^{2+} that form NH_4OH-insoluble hydroxides in the alkaline solution.

1.3.4 Si surface: Passivation

Chemical passivation of silicon surfaces is highly desirable to prevent contamination between processing steps. In passivation technique, the Si surface is rendered chemically *passive* by terminating the bonds on the surface with selective atoms or groups like, -OH, -H, -Cl , etc. A variety of routes to passivate Si surface have been explored including gas phase reactions in ultra high vacuum (UHV) condition and wet chemical process. The latter one is most easy and popular because of many applications in semiconductor industry. Due to the presence of *broken bonds* at the surface, Si substrates are extremely sensitive to the environment. Just after exposing the clean Si surface into the air it readily covered by very thin native oxide layer. Many schemes for working with Si, especially those operating in ambient conditions, rely on the fact that the high

Table 1.1: The covalent atomic radii (R_a), the electronegativity (δ) in Pauling scale, the bond-energy (D_B) with Si and the bond-length (L_B) with Si for different elements, as obtained from online sites.[75,76]

Element	R_a (Å)	δ	D_B (kJ/mole)	L_B (Å)
Si	1.11	1.90	222	2.33
Cl	0.99	3.16	381	2.02
O	0.73	3.44	452	1.63
H	0.37	2.20	318	1.48
F	0.71	3.98	565	1.60

reactivity of the clean surface can be dramatically lowered by saturating the surface with monovalent atoms such as H, Br or Cl. Such passivated surfaces are expected to be unreactive since all surface atoms achieve nearly ideal coordination. But after certain times these surfaces start to react with oxygen in ambient condition.

It should be mentioned here that passivation with different materials and their stability not only depends on the relative electronegativity (δ) and bond-energy (D_B) with Si, but also on the atomic size (R_a). Values of such parameters, obtained from the online sites,[75,76] which are essential in the description of passivation mechanism, are listed in Table 1.1.

1.3.4.1 Hydrogen passivation

H-passivated Si surface has a good resistance to chemical attack and a low surface recombination velocity which indicates a surface with a very low surface-state density. Hydrofluoric acid (HF) etching terminates the surface with a single hydrogen layer that effectively prevents oxidation and chemical contamination of Si substrate. In this process first the native oxide layer on Si surface is removed and then the surface is predominantly terminated by hydrogen atom. The ideal (100) surface tends to be terminated by SiH_2 and (111) by SiH or SiH_3 due to the difference in the number of dangling bonds between the two surfaces. Practically, the Si(111) surface can be made atomically smooth with an ideal H termination in buffered HF solutions, while the technologically important Si(100) surfaces becomes atomically rough upon HF etching, with coexistence of mono-, di-, and even trihydride species, and are found to be less stable towards contamination/reoxidation in air.[63,77]

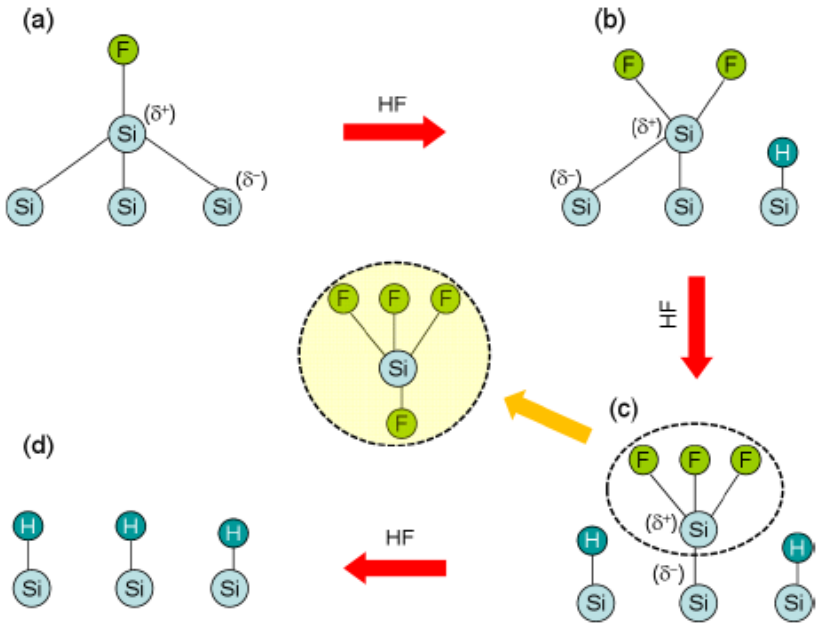

Figure 1.8: Schematic presentation of hydrogen passivation mechanism of Si surface by HF solution.

Since the late 1980s it has been well accepted that a Si surface is H-terminated instead of having F- bonded to the Si atoms when immersing in HF solution. Although the mechanism is not completely understood, it is known that the etching of SiO_2 from a Si surface occurs in following steps: In first step, the oxide layer is rapidly dissolved and forms SiF_6^{2-} ions in HF solution, making the surface temporarily F-terminated. Though the Si-F bond energy (D_B, given in Table 1.1) is very large but F-termination is not stable. Because of the large electronegativity of F compared to Si, Si-F bond polarizes the Si-Si back bonds.[63,78] This polarization allows the insertion of HF into the Si-Si bond leading to fluorination of the surface silicon and hydrogenation of the second-layer silicon. The sequence is completed resulting H-terminated Si surface as shown schematically in Fig. 1.8 with removal of the surface silicon atom as SiF_4.

The hydrophobic nature of freshly prepared H-passivated Si substrate is very well-known fact.[63] Moreover, the stability of H-terminated Si(100) and (111) surfaces stored in air has been studied by many groups.[77,79,80] They have confirmed that water present in air is predominantly involved in the oxidation of surface Si atoms having Si-H bonds, and native oxide starts to grow when most of the surface Si atoms are oxidized.

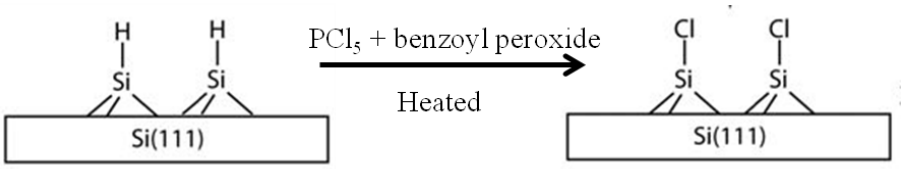

Figure 1.9: Schematic presentation of chlorine passivation mechanism of Si(111) surface by wet chemical process.

1.3.4.2 Chlorine passivation

Halogen-terminated especially, Cl-terminated Si surfaces are more reactive alternatives to the hydrogenated silicon surface for functionalization reactions.[81,82] Chabal et al. investigated three different methods for chlorination of H-terminated Si substrates: (a) exposure to a saturated solution of phosphorus pentachloride (PCl_5) in chlorobenzene; (b) exposure to chlorine Cl_2 gas and (c) exposure to Cl_2 under UV illumination.[83,84] During chlorination process, H-terminated Si surfaces are exposed to atomic Cl and the Cl atoms abstract H atoms from the Si surface, producing HCl and leaving behind Si *dangling bonds* that can then react with additional Cl radicals to produce Cl-terminated surfaces. The relatively strong electronegativity of the Cl atom, listed in Table 1.1, helps to replace the H atom, leaving the surface Cl-terminated. Ruan et al. and Silvestrelli et al. have tried to find out the initial nature of Cl-terminated Si surface, whether it is hydrophilic or hydrophobic.[85–87] The outcome of these studies provides contradictory or incomplete information about the nature of the surface, at least on the microscopic level. Furthermore, the reactivity of the Cl-passivated Si surface with water vapor and air has been studied by Chabal et al., Eves et al. and Lewis et al.[88–90] They have found that the surfaces are surprisingly stable upto 300°C, withstanding substantial exposures to water vapor and exhibiting slow oxidation in lab air. Using infrared absorption spectroscopy, high resolution electron energy loss spectroscopy (HREELS) and soft X-ray photoelectron spectroscopy (SXPS) they have identified the presence of silicon oxide on the surface and its growth with time.

1.4 Surfactant-mediated growth of nanostructures

Nanoscale materials such as nanospheres, nanorods, nanocubes, nanoplates and nanoprisms can serve as building blocks for the synthesis of advanced materials, in a way analogous to that of atoms or molecules forming the basic constituents of matter. Metal nanoparticles, particularly gold nanoparticles (AuNPs) have attracted significant attention due to their fascinating optical, magnetic, electronic and catalytic properties which is vital for fundamental science and also for wide ranging technical applications like catalysis, photonics, information storage, electronic and optical detection systems, therapeutics, diagnostics, photovoltaics and biology.[5,91–96] These unique properties of AuNPs are strongly dependent on the chemical composition, morphology (size and shape) and surface/colloidal properties of the particles and depending on the applications they are being synthesized for, using different synthesis process and then dispersion as well as stabilization of the nanoparticles is achieved by covering them with different macromolecules such as surfactants (micelles), polymers and proteins through various interactions like covalent bond, hydrogen bond, electrostatic forces, and so forth.[92–95]

Generally, AuNPs are synthesized using solution-phase method by chemical reduction of precursor gold ions involving organic solvents and then chemically attached with organic molecules that counterbalance the van der Waals attraction occurring between the nanoparticles. For example, in the widely used Brust method for AuNP synthesis, $AuCl_4^-$ is transferred into toluene or chloroform using tetraalkylammonium bromide and is reduced there with sodium borohydride in the presence of alkylthiols. The AuNPs thus synthesized are covered with strongly bound ligands that render them difficult to disperse in water and may hinder further surface modification and functionalization of particles for particular applications. Compared to such a synthesis method, another environment-friendly process where AuNPs can be synthesized in aqueous media from the chemical reduction of gold ions by reducing agents such as citric acid and ascorbic acid in the presence of one or more water-soluble polymers or surfactants as capping agents, and with the support of externally supplied energy like, photoirradiation, ultrasound irradiation, or heating is developed [97,98]. But in this process also the colloidal stability of the nanoparticles via the chemical binding of ligands at the surface of the

nanoparticles, may alter the properties of the nanoparticles through a modification of their electronic density and the dielectric constant of the surrounding medium. To maintain the intended properties of nanomaterials, a strategy based on the physical adsorption of ligands on the surface of the nanoparticles may be preferable [5,93].

Recently lots of work is going on to develop simple, versatile and economically viable methods to prepare AuNPs in a size- and shape- controlled manner by chemical reduction of gold ion in aqueous media with utilization of the ligands for stabilization. The ligands used to achieve an efficient physical stabilization are usually surfactants or macromolecules, such as linear or hyperbranched polymers. Sakai et al. have introduced a single step process to synthesize AuNPs at ambient temperature by reducing gold ion in aqueous solution of triblock copolymer which acts as both reducing and stabilizing agent.[5,99–101] This synthesis proceeds fast to completion (in less than 2 h), and is environmentally benign and economical since it involves only water and non-toxic, commercially available polymers. The colloidal gold dispersions can remain highly stable for several years. Further, the same starting materials can lead to a variety of nanoparticle morphologies (e.g., spheres, plates, prisms, icosahedra) depending on the polymer composition, molecular mass, and concentration. There are additional potential benefits emanating from the use of TBPs, not only as structure-directing agents but also as templating or structuring media. TBP templates can form matrices that afford processability, mechanical and chemical stability, and morphological versatility, as well as novel properties of the resulting nanoparticles.

In the following, first we will give a brief introduction of triblock copolymer and its properties and then there will be a review about the formation of AuNPs in aqueous triblock copolymer solution.

1.4.1 Triblock copolymer and its properties

Copolymers are a special type of polymers of high molecular weight which have two or more different monomer units linked by covalent bonds. Triblock copolymer (TBP) belong to a special category of water soluble nonionic surfactants with two dissimilar moieties, hydrophilic polyethylene oxide (PEO) block and hydrophobic polypropylene

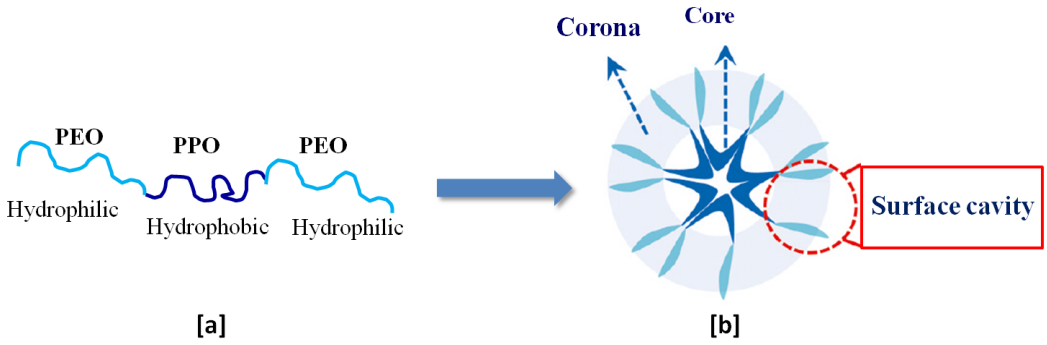

Figure 1.10: (a) The schematic diagram of a TBP molecule. (b) A TBP micelle with the core occupied by PPO units and the corona constituted by PEO units.

oxide (PPO) block, within the same molecule. These TBPs (with the commercial name of Pluronics) possess a symmetrical structure $(PEO)_x$-$(PPO)_y$-$(PEO)_x$, where x and y denote the number of ethylene oxide and propylene oxide monomers per block, respectively, and are available in a range of x and y values in the form of pastes, flakes and liquids. A TBP becomes predominantly hydrophilic when the number of PEO units exceeds the number of PPO units but acquires a predominantly hydrophobic nature when the reverse happens.[102–104]

In aqueous solution, the TBPs self assemble to form polydisperse micelles of various forms and size ranging from a few to several hundred nanometers. The hydrophobic blocks of the TBP (PPO) form the core of these micellar aggregates, whereas the hydrophilic ones (PEO), with the surrounding water molecules, form the corona. The shape transitions of the micelles are closely associated with a number of factors such as the molar masses of the PEO or PPO units, salt additives, the nature of the solvent, concentration, and temperature. Predominantly hydrophilic TBPs are prone to the formation of compound micelles, but predominantly hydrophobic TBPs usually produce well-defined micelles. Micelles undergo several structure transitions (i.e., micelles $\rightarrow$ threadlike micelles $\rightarrow$ vesicles, etc.) with concentration and temperature variations. Because of the stability, chemical and structural diversity, controllable molecular weight, useful mechanical properties, and most importantly their environmentally friendly nontoxic nature, pluronic TBPs have been used extensively to prepare various self-assembled biomimicking organized structures like micelles, mixed micelles, and vesicles (polymer-

somes), depending on the experimental conditions like temperature, concentration, composition and solubilizing media for various applications. These confined model systems are now being applied in medicinal chemistry as vehicles of drug carrier, catalytic reaction media, and templates for nanoparticles synthesis.[105,106]

1.4.2 Formation of AuNPs in TBP solution

Sakai and Alexandridis have shown that the PEO-PPO-PEO TBPs can act as very efficient reductants as well as stabilizers in the single-step synthesis and stabilization of AuNPs from hydrogen tetrachloroaureate hydrate ($HAuCl_4.3H_2O$) in air-saturated aqueous solutions, at ambient temperature, and in the absence of any additional reductants or energy input.[5,99–101] This is due to the amphiphilic character (dual nature) of the PEO-PPO-PEO block copolymers. Sakai et.al. have proposed the formation mechanism of AuNPs in aqueous PEO-PPO-PEO TBP solutions on the basis of systematic studies on the TBP concentration dependence of absorption spectra, the time dependence (kinetics) of the gold ion $HAuCl_4$ reduction, and the TBP concentration dependence of particle size. The mechanism is described by three main steps:
(i) *initial reduction of metal ions in aqueous TBP solution*: The PEO in PEO-PPO-PEO TBPs forms cavities (pseudo-crown ether structure) that can bind gold ions and reduction of bound $AuCl_4^-$ ions can proceed via oxidation of the oxyethylene and oxypropylene segments by the metal center.
(ii) *absorption of TBPs on gold clusters and further reduction of metal ions on the surface of these gold clusters*: Due to amphiphilic character of the PEO-PPO-PEO TBPs, they adsorb on the surface of gold clusters and form pseudo-crown ether structures that can bind with $AuCl_4^-$ ions and facilitate their reduction.
(iii) *growth of AuNPs and stabilization by TBPs*: The reduction of $AuCl_4^-$ ions and formation of gold clusters (step 2) is repeated on the surface of AuNPs, and therefore the particles grow.

The PEO corona are arranged in the form of surface cavities which are in direct contact with the aqueous solution and constitute the micelle-solution interface of a TBP micelle. In the initial reduction process (step 1), PEO block is more dominant than

PPO block, though both PEO and PPO units of TBPs contain ether oxygens, which act as mild reducing agents. PPO would help TBP adsorption on gold clusters and the subsequent reduction of $AuCl_4^-$ ions by both PEO and PPO blocks on the surface of the gold clusters takes place (step 2). Thereby the reduction of $AuCl_4^-$ ions would be enhanced on the surface of gold clusters and/or particles (step 3). So, it is expected that any change in the micelle environment (PEO/PPO block length, molecular weight of TBP, concentration of TBP solution, temperature of TBP+gold mixed solution) cause a significant change in the reduction, growth, morphology and also stabilization of nanoparticles.

Recently, researchers have paid attention to reveal the influence of different solution and processing parameters in the formation and growth mechanism of AuNPs, but still it is necessary to carry out more systematic investigation. Ray et al. have examined the synthesis of AuNPs using TBP Pluronic P85 at different concentrations as a function of hydrogen tetrachloroaureate (III) hydrate in aqueous solution.[107] The number density of TBP micelles increase almost linearly with the concentration, which is related to result in higher numbers of nucleation centers of AuNPs formation and therefore increase in the yield of AuNPs. The fact that increase in the number density of nanoparticles also increases the chances of aggregation and this tends to decrease the stability of nanoparticles at higher TBP concentration. To enhance the concentration of stabilized nanoparticles they have added an additional reductant (trisodium citrate) in TBP solution and also introduced step-addition method where the gold salt is added in small steps in the TBP solution.[102,108] Khullar et al. have used three block polymers, L31, L64, and P123, for the synthesis of AuNPs to monitor the effect of their micelle size, structure transitions, and environments on the mechanism of the reduction process leading to the overall morphology of AuNPs.[106] By simultaneous measurement of ultraviolet-visible (UV-vis) spectroscopy they have monitored the aqueous phase reduction with time at constant temperature and under the effect of temperature variation from 20 to 70°C. Moreover, they have detected significant differences from the mechanistic point of view in the synthesis of AuNPs when predominantly hydrophilic F68 and hydrophobic P103 are used.[105] Liu et al. have used different TBPs of different PEO and PPO block units

to study the effect of hydrophobicity of TBPs on the formation and stabilization of AuNPs.[91]

It is known that the reactivity of the gold complexes, reflected by their reduction potential, changes markedly by varying pH. Peng et al. have studied the growth kinetics and temporal size/shape evolution of AuNPs by citrate reduction in boiling water, and results reveal that the size variation and overall reaction mechanism were mostly determined by the solution pH that was in turn controlled by the concentration of sodium citrate (Na_3Ct).[92] Liu et al. have tried to understand the reaction pathway of the AuNPs formation in TBP aqueous solution of different pH values.[109] They have found that in low pH region the reduction of gold ion is very slow and results in unstable large aggregated nanoparticles of various shape, whereas with increase of pH value of micellar solution, the reduction process of gold ion is accelerated and highly-stabilized nanoparticles with small average diameter and narrow size distribution are formed. The attention was mainly focused to observe the final shape and size of the nanoparticles formed at different pH values using UV-vis spectroscopy together with Transmission electron microscopy (TEM) and dark field optical microscopy.

1.5 Motivation and objective of the thesis

The motivation behind the present thesis, which originates from the above review of Si surface, sol-gel films, mesostructureed films prepared by EISA process and surfactant-mediated growth of nanostructures are the followings:

According to the review, most of the chemical composition used to synthesize sol-gel silica film usually yield films with a thickness of submicron to a few microns, which do not suit many applications, where coatings of a few nanometers are required. Moreover, from the review it is not clear that how the sol-gel material is attached with silicon substrate to form thin film and how this attachment depends on different solution compositions and experimental conditions. So one of the objectives is to understand and control the different process parameters for the preparation of sol-gel silica thin films on Si substrates. Recently developed X-ray reflectivity (XR) technique, which will be discussed in chapter 3, is specifically help us to get information about the film-substrate

interface and also about the microstructure i.e., the thickness and average density or porosity of the film.

From the review of mesostructured silica film it is not clear how different treatment or passivation of Si surface control the overall structures of the mesostructured film and their stability with time at ambient condition. In most of the studies scientists have used grazing incidence X-ray scattering (GISAXS) technique to know the overall mesostructure of the film and TEM measurements for direct imaging. GISAXS measurements although provide both in-plane and out-of-plane information of a film, but the information about the film-substrate interface e.g. attachment of the film with the substrate, shape of the micelle at substrate surface etc. can not be obtained. On the other hand, by direct deposition on the TEM grid we observed the in-plane structure of the film that grows on carbon surface. Substrate effect can not be observed by preparing films directly on grids, rather we have to scrap the films from the substrates and have to prepare grids. This is a destructive process and at the same time this may change the actual structure of the films. So the main objective is to use complementary X-ray scattering techniques, namely XR and GISAXS (which will be discussed in chapter 3) to monitor the structures (especially interfaces) and their evolution in non-destructive manners. Using scattering techniques, the structural evolution of different mesostructured silica film as a function of surfactant/silica molar ratio and formation of mesoporous silica films by removing the surfactant template from such mesostructured films have been studied in chapter 3. Also the effect of substrate surface nature (hydrophilic/hydrophobic) and excess alcohol on the 2D-hexagonal surfactant-silica mesostructured films is another important topic that will be discussed in the same chapter.

As discussed in the review of Si surface, the initial nature of a Cl-terminated Si surface whether it is hydrophilic or hydrophobic, is still a subject of contradiction. Moreover, though researchers have studied the growth of oxide layer on Cl-Si surface as a function of time, but the change in wetting behavior i.e., hydrophilic/hydrophobic behavior of such surface with time is not discussed at al. It is well accepted that the wetting/nonwetting i.e., hydrophilic/hydrophobic nature of a surface is better understood by contact angle (CA) measurement, which gives the information in macroscopic

levels. Macroscopic level information may not match with microscopic level information.[87] Such limitation of CA can be overcome by depositing mesostructured silica film on Cl-terminated Si substrates and determining its structure using XR and GISAXS measurements, which are exactly our objectives. The mesostructured silica film has not been used before as a tool to explore the hydrophilic-hydrophobic (polar/nonpolar) nature of a surface and to understand the stability-instability information of surface, from the point of view of hydrophilic-hydrophobic nature, whcih we have used along with the conventional CA measurements.

The review about the formation of AuNPs in aqueous TBP solution suggests that different solution condition of TBP micelle influence alot in the formation and growth of AuNPs. One of such important parameter is the pH value of aqueous TBP micellar solution in the synthesis of AuNPs. Liu et al. have tried to investigate the effect of pH of micellar solution on the synthesis of AuNPs,[109] but during reaction, how the reduction of gold ion and then formation, growth and stabilization of AuNPs in the solution are influenced by the pH value of micellar solution is not discussed in details. Also, during reaction, the time evolution of other absorption bands arising due to TBP micelles, ligand-to-metal charge transfer (LMCT) complex etc. in UV-vis spectra at different pH value is not well understood till now. Moreover, the influence of addition of gold ion in aqueous TBP solution i.e., how the morphology of the TBP micelle is changing when it acts as reducing and stabilizing agent at different pH value is still unknown. All these understandings are of prime importance, which we have tried to address in the thesis.

1.6 Our work and outline of the thesis

This dissertation presents some of the recent important experimental findings based on the study of structural variation of surfactant templated mesostructured films depending on different substrate surface conditions and formation and growth mechanism of surfactant mediated AuNPs. This thesis has been divided into seven chapters.

In chapter 1 we have introduced the subject followed by a brief review of growth and structure of surfactant mediated nanostructures, with special emphasis on mesostructured films on Si substrate and synthesis of AuNPs and finally the motivation and goal

of the thesis has been presented. Processes, which are responsible for the change in the nature of Si substrate surface, are also discussed.

Chapter 2 is devoted to the brief description of the experimental techniques and instruments used during the synthesis and characterization of surfactant templated mesostructured silica thin film and surfactant-mediated growth of AuNPs. This includes the basic working principle and a brief description of the instrumentation.

Chapter 3 describes the influence of different solution parameter and processing condition on the structure (porosity, electron density) of sol-gel derived spin-coated silica films. The films are characterized by XR technique which not only provide the out-of-plane microstructural information of the films but also the information about the film substrate interface i.e., the initial attachment of the film with the substrate can be obtained from this technique. Analysis of the XR data suggests that all the films are probably made of woolen ball like porous nanostructures of silica network and poor attachment of the films with the substrate is a characteristic feature of all the films, though the attachment of the film with the substrate and its porosity can be tailored by varying the ethanol concentration in the solution and also changing the duration of aging time of the solution prior film deposition.

Chapter 4 is devoted to monitor structural evolution of CTAB-silica mesostructured films with respect to different synthesis conditions like CTAB/silica molar ratio and solvent concentration and influence of substrate surface condition on the growth and structure of the films with different thickness. The removal of surfactant template to prepare mesoporous silica film from mesostructured silica film is also described in this chapter. In the first section, formation of different mesostructured films, with 3D-hexagonal structure of $P6_3/mmc$ space group, constituted from a dense packing of spherical micelles and 2D-hexagonal structure of $p6m$ space group, constituted from cylindrical micelles is observed by varying only the surfactant concentration in the initial solution. The second section is based on understanding the role of such substrate surface conditions i.e., hydrophilic and hydrophobic nature of the substrate on the initial attachment of silica coated surfactant molecules, which can not only control the initial mesostructure of the film, but also the final mesostructure through subsequent

drying. The cylindrical shaped micelles, which are initially circular on a hydrophilic OH-terminated Si substrate in order to form a perfect 2D-hexagonal structure, become elliptical (extended along the in-plane) on a hydrophobic H-terminated Si substrate to form a slightly compressed 2D-hexagonal structure due to a different attachment of the film to the substrate. Moreover, it is found that alcohol can act as a cosolvent or cosurfactant in mesostructure formation and can modify the mesostructure accordingly. The removal of surfactant using solution extraction method from different mesostructured film is achieved to prepare mesoporous silica film is described in section three. It is found that the overall structure of the film remains same though the shape of the pores becomes less spherical as a result of successive treatments.

Chapter 5 is devoted to determine the initial nature (hydrophilic/hydrophobic) of a Cl-terminated Si surface prepared by a wet chemical process and to investigate the stability-instability of such surface under ambient condition. In the first section, the wetting behavior of Cl-terminated Si surface is investigated on the macroscopic level as well as on microscopic or molecular level. On macroscopic level the nature of Cl-Si surface can be obtained from conventional contact angle measurement and to investigate the behavior on microscopic or molecular level the structure of CTAB-silica 2D-hexagonal mesostructured thin films deposited on Cl-Si surface along with hydrophilic OH-Si and hydrophobic H-Si surface has been examined using XR and GISAXS techniques. The molecular level information agrees well with the macroscopic level information suggesting weak hydrophilic nature of Cl-Si surface. The second section reveals the stability-instability information of the Cl-Si surface at ambient condition from the point of view of hydrophilic-hydrophobic nature of the surface on both macroscopic level and molecular level using contact angle and X-ray scattering measurements, respectively. The structure of CTAB-silica 2D-hexagonal mesostructured thin films deposited on different time-evolved Cl-Si surface is monitored using XR and GISAXS techniques which suggests the transition of nature of Cl-Si surface from weak-hydrophilic toward weak-hydrophobic with time.

Chapter 6 is based on synthesis of AuNPs in TBP aqueous solution at ambient condition. The influence of pH value of TBP aqueous solution on reduction of gold ion

and also on formation and growth of AuNPs is investigated by observing not only the final state of the solution containing AuNPs and TBP micelles but also studying the temporal evolution of ternary mixture of TBP+ precursor gold salt+ water. The results suggest that though the size and shape of TBP micelles remain unaltered at different pH values, but the formation mechanism of AuNPs and the final morphology i.e., shape and size of the AuNP-micelle nanocomposite is highly influenced by the pH value of aqueous TBP solution. At low pH value (6.5 - 9), the rate of reduction of gold ion is slow and AuNP with larger size and different shape is formed. On the other hand, at high pH value (9.5 - 12) reduction rate of gold ion is accelerated along with formation of well dispersed small AuNPs with ordered structures.

Chapter 7 concludes the thesis with a brief summary of the major experimental findings from our experiments.

2

Experimental details

The sample preparation processes and their characterization techniques along with the instruments used in our experiment are described in the following sections. Mesostructured silica films on differently-terminated Si surfaces were prepared by spin-coating technique, while gold nanoparticles (AuNPs) were synthesized in aqueous triblock copolymer (TBP) solutions. The mesostructured films have been characterized by two complementary X-ray scattering techniques - X-ray reflectivity (XR) and grazing incidence small angle x-ray scattering (GISAXS), whereas the AuNPs in aqueous TBP solution have been characterized using dynamic light scattering (DLS), ultraviolet-visible spectroscopy (UV-vis) and transmission electron microscopy (TEM) techniques. Differently-terminated Si surfaces were characterize using contact angle (CA) measurement and X-ray photoelectron spectroscopy (XPS) techniques. Different preparation and characterization techniques along with the instruments used in our experiment are described in the following sections.

2.1 Sample preparation

2.1.1 Surfactant templated mesostructured silica films

Mesostructured silica films were prepared by spin-coating the silica-surfactant solutions on differently-terminated Si surfaces.

2.1.1.1 Solution preparation

Silica-surfactant solution was prepared using tetraethyl orthosilicate [TEOS, $Si(OC_2H_5)_4$, Sigma Aldrich, 99.999%] as silica source, cetyltrimethylammonium bromide [CTAB, $C_{16}H_{33}N(CH_3)_3Br$, Fluka, $\geq$99%] as structure directing surfactant agent, ethanol [C_2H_5OH, Merck, absolute] and Milli-Q water (resistivity 18.2 MΩ cm) as common solvent and hydrochloric acid [HCl, Merck, 35%] as catalyst. The precursor solution was prepared in two steps by selecting fixed ratio of CTAB and silica. In the first step, a silica sol was prepared by hydrolysis and condensation of TEOS in acidic condition. For that, silica sol was prepared in the molar ratio of TEOS : C_2H_5OH : H_2O = 1 : 4.5 : 1 and finally added the required amount of HCl to the the solution to keep the pH value $\sim$1. The solution was then stirred for 1 hour at room temperature. In parallel, a second solution was prepared by dissolving 0.348 g of CTAB in ethanol and water of molar ratio 3.66 : 1. In the second step, second solution was added to the first one to get the final solution in the molar ratio of TEOS : CTAB : C_2H_5OH : H_2O = 1 : 0.19 : 20 : 5.5, which was then stirred for another 1 h and aged for 2 h. The concentration of the surfactant in the solution was kept above critical micelle concentration (cmc) and a particular molar ratio of surfactant and silica was chosen such that 2D-hexagonal mesostructure with the $p6m$ space group, constituted from cylindrical micelles could be prepared. Different diluted solutions were then prepared by adding excess ethanol to the stock solution.

2.1.1.2 Substrate preparation

Substrate preparation is an important part of our experiment. This means modification of the Si surface using different wet-chemical processes, which essentially modifies the surface free energy, polar-nonpolar (hydrophilic-hydrophobic) or electrostatic nature, surface defect states and the reactivity of the Si surface. In this section preparation process of four differently passivated Si substrates (X-Si, where X = O, OH, H and Cl) will be discussed.

2.1.1.2.1 O-Si substrate: The Si substrates were cleaned in an ultrasonic bath, first using trichloroethylene solution for about 10 min and then using methyl alcohol

solution for another 10 min to remove the organic contaminants present on the substrate surface. Native oxide covered such substrates are labeled as O-Si.

2.1.1.2.2 OH-Si substrate: After removing the organic contaminants, Si substrates were boiled at 100°C for about 15 min in a mixed solution of ammonium hydroxide [NH_4OH, Merck, 30%], hydrogen peroxide [H_2O_2, Merck, 30%] and Milli-Q water ($NH_4OH : H_2O_2 : H_2O = 1 : 1 : 5$, by volume). The substrates were then rinsed thoroughly with Milli-Q water. This makes the substrates OH-terminated and labeled as OH-Si.

2.1.1.2.3 H-Si substrate: The OH-terminated Si substrates were used to prepare H-terminated Si substrates. During the H-passivation process, the OH-Si substrates were etched in a solution of hydrogen fluoride [HF, Merck, 10%] for 30 s at room temperature (25°C) and then rinsed with Milli-Q water. In the case of Si(111) substrates, they were subsequently etched in ammonium fluoride [NH_4F, Merck, 40%] solution for 2 min at room temperature and then rinsed with Milli-Q water to prepare H-Si(111) substrates. Such H-terminated Si substrates are labeled as H-Si.

2.1.1.2.4 Cl-Si substrate: The H-Si substrates were chlorinated through a wet-chemical method. A chlorinating solution was prepared by dissolving phosphorus pentachloride [PCl_5, Merck] in chlorobenzene [C_6H_5Cl, Merck] to form a near-saturated solution (typically 0.6 M). The solution was heated at ∼60°C for 1 h for complete dissolution of the PCl_5. Immediately before use, a few grains of benzoyl peroxide (∼300 mg) were added to the stock solution (∼80 ml). The H-Si samples were then immersed into the solution and heated to 90-100°C for 45 min. Finally, the samples were rinsed with anhydrous tetrahydrofuran and anhydrous methanol. These substrates are labelled as Cl-Si.

2.1.1.3 Film preparation

Surfactant-silica mesostructured films were deposited on differently-terminated Si substrates using spin-coating technique. In the following, first we will briefly discuss about

the spin-coating technique followed by the instrumental specification and the deposition conditions.

2.1.1.3.1 Spin-coating technique: Spin coating is a well-established and easy technique in microfabrication to form highly uniform thin film on flat surface with adjustable thickness over large area. Spin coating takes very small time (a few minutes) and the thickness control (from several microns to a few nanometers) is better than that provided by dip coating or drop casting techniques. One of the reasons for this technique to be popular in coating applications is its merit to produce highly uniform and homogeneous films with very low interfacial roughness (of a few angstroms). In this technique films can be prepared by applying a thick layer of solution onto a rotating flat substrate and then drying by fast evaporation of the solvent. The basic mechanism governing the spin coating process as elucidated after the pioneering work on the flow of Newtonian fluids on a rotating disk by Emslie, Bonner and Peck in 1958,[110] which was further extended by Acrivos, Shah and Petersen for non-Newtonian fluids.[111] Later on, Meyerhofer introduced the evaporation of the solvent as an important controlling mechanism in the process.[112]

A spin coating process is usually composed of four distinct stages: deposition, spin-up, spin-off and evaporation.[15] In the first step, a drop of colloidal suspension is deposited at the center of a fixed substrate. In the spin-up step, the substrate is accelerated to a certain rotational speed and most of the solution is thrown off the substrate immediately, leaving a thin layer which spreads radially outwards from the center of the substrate under the action of centrifugal force. The topmost layer of the fluid encounters highest radial velocity which decreases gradually towards the substrate, the fluid layer in contact with the substrate has zero radial velocity. In the spin-off stage, the thickness of the film reduces due to equilibrium between centrifugal force and viscous shear force. Finally, evaporation of the solvent dominates in the fourth stage, where the film thickness reduces. The transition between the third and fourth stage depends notably on the volatility of the solvent. To get homogeneous films, several important factors such as (i) evaporation rate of the solvent, (ii) viscosity of the fluid, (iii) concentration of the solution, (iv) angular velocity (spinning speed) and (v) spinning time have to be

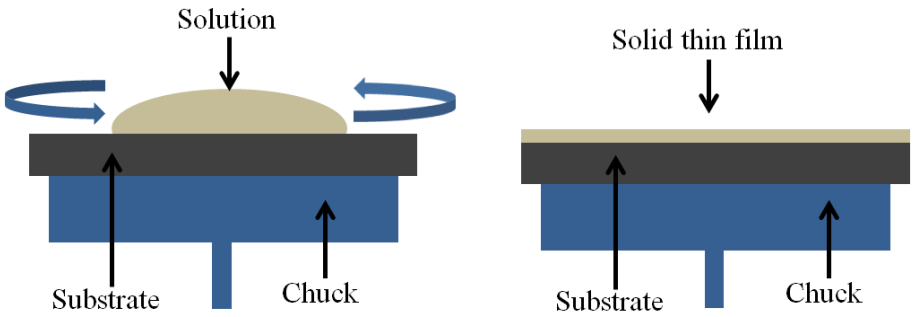

Figure 2.1: Schematic diagram representing thin film preparation by spin-coating technique

considered. The spin-coating process is schematically shown in Fig. 2.1.

Generally, the final thickness d_f of the film depends on the fluid viscosity, the spinning speed of the turntable and the total time t that the sample is rotated. To determine this dependence, it is necessary to solve the force balance equations of hydrodynamics during the spin coating process using the model developed by Emslie et al.[110] This model is applicable for Newtonian fluid i.e., the fluid has the constant viscosity throughout the process and not for non-Newtonian fluids (polymers), where the viscosity of the solutions is a function of time due to the constant evaporation of solvent during spinning. Now according to the hydrodynamics, the two opposite forces, the centrifugal force and the viscous force, act between the adjacent fluid layers, and the force balance equation in cylindrical coordinates for the Newtonian fluids is given by

$$\eta \frac{\partial^2 v(z)}{\partial z^2} = -\rho \omega^2 r \tag{2.1}$$

where η is the viscosity of the solution, $v(z)$ is the radial velocity at height z from the substrate, ρ is the solutions density, ω is the angular speed of rotation and r is the radial distance from the axis of rotation z. Solving this equation along with the continuity equation given by:

$$\frac{\partial h}{\partial t} + \frac{1}{r}\frac{\partial}{\partial r}(rq) = 0 \tag{2.2}$$

where q is the radial flow of fluid per unit length of circumference, we obtain the instan-

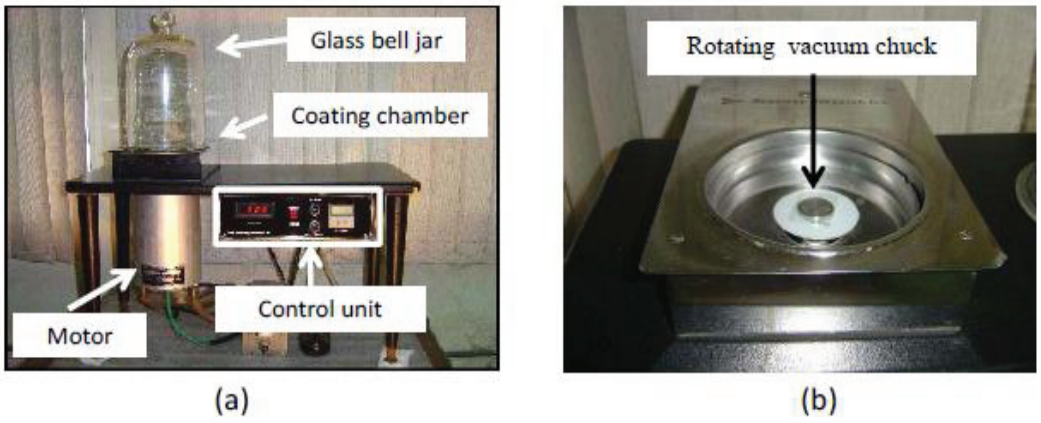

Figure 2.2: (a) The spin-coating unit (EC101, Headway Research Inc., USA, EC101) used in our experiments. (b) A close view of the coating chamber used in spin coating unit.

taneous thickness of the film $h(t)$ as

$$h(t) = h_0/(1 + 4\rho\omega^2 h_0^2 t/3\eta)^{1/2} \tag{2.3}$$

where h_0 is initial film thickness and t is time. However, practically the various operating conditions may not satisfy the assumption required by this equation.

2.1.1.3.2 Instrumental specification: The spin-coating unit (EC101, Headway Research Inc., USA) used in our experiment for thin film preparation is shown in Fig. 2.2(a). It has a coating chamber which is mounted on a stage. The chamber houses a vacuum chuck, which can be rotated with a high speed motor (maximum rotation speed ∼10000 rpm) attached below the horizontal stage. A close view of the vacuum chuck is shown in Fig. 2.2(b). An array of grooves are present on the upper face of the chuck to create a vacuum between the substrate and the chuck so that the substrate is attached tightly with the chuck during spinning. A rotary vacuum pump (not shown in the figure) sucks the air between the chuck and the substrate. During film preparation the coating chamber is covered with a transparent *glass bell jar* to avoid contamination form the atmosphere. To adjust the spinning speed, acceleration and time duration of spinning, a electrical control unit is attached with this spin-coating unit. The timer can be set to rotate the chuck for a given span of time and the spinning speed is displayed

on the panel of the control unit.

2.1.1.3.3 Deposition conditions: Films were prepared from differently diluted solutions on differently-terminated Si surfaces using the spin-coater at a speed of 4000 rpm. The duration of spin-coating was 1 min and during spin-coating, the ambient temperature and relative humidity were 25-30°C and 70-75%, respectively.

2.1.2 Surfactant mediated growth of AuNPs

2.1.2.1 Solution preparation

AuNPs were prepared from mixed aqueous solution of TBP surfactant and hydrogen tetrachloroaureate (III) trihydrate ($HAuCl_4.3H_2O$, Sigma-Aldrich) at room temperature, by the method developed by Sakai et al.[99–101] As TBP we used Pluronic P123 [$HO(CH_2CH_2O)_{20}(CH_2CH(CH_3)O)_{70}(CH_2CH_2O)_{20}H$, Sigma-Aldrich, M_w=5800] and Milli-Q water was used as solvent for all solution preparation.

As a first step, aqueous P123 solution of concentration 3.33% w/v (5.75 mM) was prepared by magnetic stirring for 2 h and then aqueous $HAuCl_4$ solution of concentration 2 mM was prepared. It is to be noted that during synthesis of AuNPs the concentration of aqueous solution of P123 and $HAuCl_4$ were kept fixed. Finally, 45 ml of P123 solution is mixed with 5 ml of $HAuCl_4$ solution and stirred for about 10 min. Then the mixed solutions were kept at ambient condition (∼25°C and ∼40%) for 3 h without any disturbances. The transparent colorless solution of P123 became colorful with time due to the AuNPs formation. The color remained almost same after 3 h suggesting possible stabilization.

2.2 Characterization

2.2.1 X-ray scattering

X-rays can interact with matter through different mechanisms.[113,114] However, in this discussion, we shall consider only Thomson scattering, where a charged particle is accelerated by the oscillating electric field of the incident radiation and then the particle

re-radiates the energy gained. The scattering is more efficient for the light electrons than the heavy nuclei (actually it is proportional to inverse of mass). When the frequency of the electromagnetic radiation is much larger than the characteristic atomic frequencies, which is the general case for X-rays and the light atoms of soft materials, the electrons can be considered as free electrons and the materials can be simply characterized by its electron density ρ.

X-ray scattering techniques are a family of non-destructive analytical techniques which reveal information about the crystallographic structure, chemical composition and physical properties of bulk materials and of thin films. These techniques are based on observing the scattered intensity of an X-ray beam hitting a sample as a function of incident and scattered angle, polarization and wavelength or energy. There are various types of X-ray scattering techniques, called - X-ray diffraction (XRD), grazing incidence diffraction (GID), small angle X-ray scattering (SAXS), grazing incidence small angle X-ray scattering (GISAXS), X-ray reflectivity (XR), diffuse scattering, etc. In this section, we have mainly concentrated on the basic formalism and instrumentation of XR and GISAXS techniques.

2.2.1.1 Basic formalism

For X-ray radiation, the refractive index n, of a homogeneous medium with multiple species can be written as[115]

$$n = 1 - \delta(r) + i\beta(r) \tag{2.4}$$

where $\delta(r)$ and $\beta(r)$ are dispersion and absorption terms defined as[116]

$$\delta(r) = \frac{\lambda^2}{2\pi} r_e \rho(r) \tag{2.5}$$

and

$$\beta(r) = \frac{\lambda}{4\pi} \mu(r) \tag{2.6}$$

ρ is the electron density of the medium, $\mu(r)$ is the linear absorption coefficient of the medium, λ is the X-ray wavelength and $\mathrm{r}_e = e^2/mc^2 = 2.814 \times 10^{-5}$ Å is the classical electron radius. For X-rays, the dispersion term $\delta = 10^{-6}$, and the absorption β is

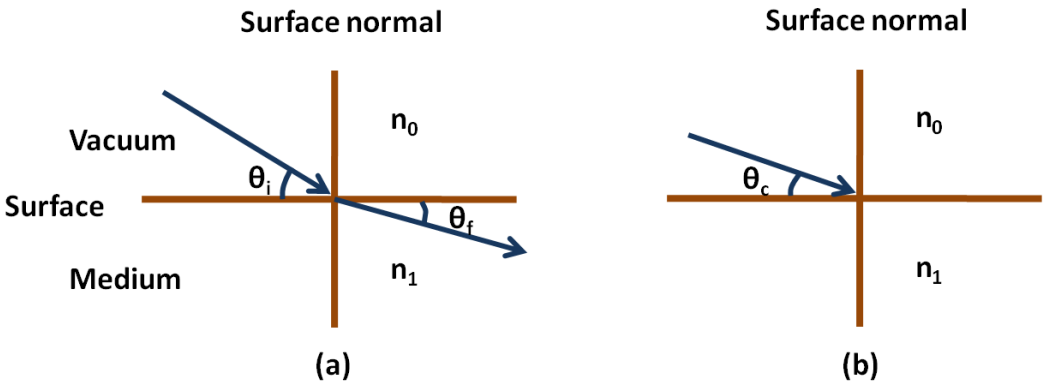

Figure 2.3: (a) Schematic representation of X-ray refraction by an interface with a grazing incident angle θ_i. (b) the critical angle of incidence θ_c for the total external reflection.

usually one or two orders of magnitude smaller. Therefore, for X-rays the refractive index of the medium is slightly less than unity.

According to the laws of optics, X-rays suffer total external reflection when propagation through a medium of higher refractive index to a surface of a material having lower refractive index.[114,117,118] The condition to observe total external reflection is that the ray incident at an angle θ_i is less than the critical angle θ_c. The critical angle θ_c can be obtained applying the law of refraction (Snell's law) for a single vacuum /medium (n_0/n_1) interface which is shown schematically in the Fig. 2.3(a). The Snell's law gives

$$n_0 \cos\theta_i = n_1 \cos\theta_f \tag{2.7}$$

The critical angle is defined as the angle of incidence $\cos\theta_i = \cos\theta_c$ at which the angle of refraction $\theta_f = 0$, and at that time only an evanescent wave propagates along the surface as shown in Fig. 2.3(b). At this condition X-rays do not penetrate far into the medium, and all incoming radiations are reflected with small loss due to the absorption of the medium. Assuming absence of absorption ($\beta = 0$) in Eq. 2.4, Eq. 2.8 yields,

$$\cos\theta_c = n = 1 - \delta \tag{2.8}$$

Since δ is of the order of 10^{-6}, the critical angle for total external reflection is

extremely small. In the case of small angles, cosθ_c can be approximated as,

$$\theta_c = 2\delta = \lambda\sqrt{\frac{r_e\rho}{\pi}} \tag{2.9}$$

The total external reflection of an x-ray (or neutron) beam is therefore only observed at grazing angles of incidence below about $\theta < 0.5°$.

2.2.1.2 X-ray reflectivity

Specular X-ray reflectivity (XR) is a surface-sensitive analytical technique used in chemistry, physics and material science to characterize surfaces, thin films, and multilayers and has emerged as a powerful tool for the investigation of the structural properties of thin films.[114,116,119] The basic idea behind the technique is to reflect a beam of X-rays from a flat surface and then measure the intensity of X-rays reflected in specular direction (reflected angle equal to incident angle). The theory of XR is valid under the assumption that electron density is continuous. Under this approximation, the reflection is treated like in optics, and the reflection and transmission coefficients can be derived by writing the conditions of continuity of the electric and magnetic fields at the interface. If the interface is not perfectly sharp and smooth then the reflected intensity will be deviate from that predicted by the law of Fresnel reflectivity. The deviation can be analyzed to obtain the electron density profile of the interface normal to the surface.

In XR technique, a well collimated monochromatized X-ray beam is allowed to be incident on a surface/interface at a grazing incidence θ_i (starting from a few milliradians) and the reflected intensity is recorded in the plane of incidence ($\phi = 0$) at an angle θ_f. If the angle of incidence of impinging X-rays is sufficiently small (less than θ_c), the penetration depth and the scattering is limited to the near interface region. XR data is generally taken at angles considerably larger than the critical angle of total external reflection and therefore penetration depth is of the order of hundreds of nanometers. There is interference of X-rays coming from layers with different electron densities at different depths in the material and after properly recording and fitting the data, one can estimate the electron density profile of the material across its depth with a fairly high degree of accuracy.

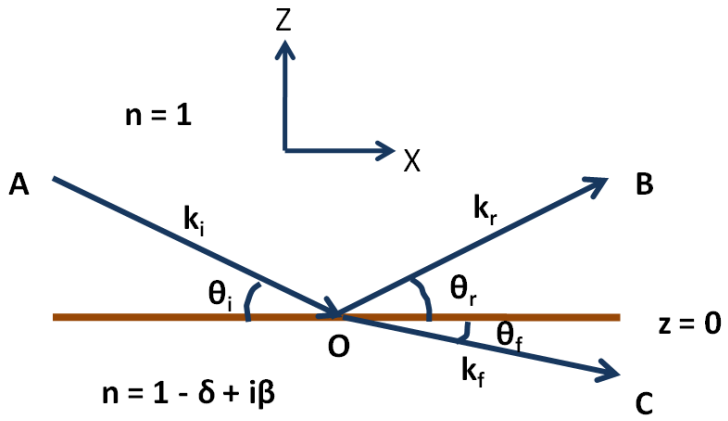

Figure 2.4: Reflected (OB) and transmitted (OC) beams of a plane electromagnetic wave incident (AO) at an interface separating two media.

Specular reflectivity, defined as the square of the modulus of reflection coefficient is conventionally written as the ratio[114]

$$R(\theta) = I(\theta)/I_0 \quad \text{or } R(q) = I(q)/I_0 \tag{2.10}$$

where $I(\theta)$ or $I(q)$ is the reflected intensity for an angle of incidence θ (or wavevector transfer q), and I_0 is the intensity of the incident beam.

Now considering the situation shown in Fig. 2.4, the reflectivity of a perfectly smooth vacuum/medium interface will be calculated. Let a plane wave in vacuum, $\mathbf{E}_i(r) = A_i \exp(i\mathbf{k_i}.\mathbf{r})$, with incident wave vector $\mathbf{k}_i = k(\cos\theta_i, 0, -\sin\theta_i)$ and amplitude A_i, is incident on the medium of refractive index $n = 1 - \delta + i\beta$ at an angle θ_i. Partly the ray will be reflected by the medium and transmitted into the medium, and using the law of refraction, the reflected and transmitted fields may be described as $\mathbf{E}_r(r) = A_r \exp(i\mathbf{k_r}.\mathbf{r})$, with reflected wave vector $\mathbf{k}_r = k(\cos\theta_r, 0, \sin\theta_r)$ and amplitude A_r, and $\mathbf{E}_f(r) = A_f \exp(i\mathbf{k_f}.\mathbf{r})$, with transmitted wave vector $\mathbf{k}_f = (k_{f,x}, 0, k_{f,z})$ and amplitude A_f. Now the law of refraction i.e., Snell's law and the Fresnel equations are obtained by applying the boundary conditions that the wave and its derivative at the interface $z = 0$ must be continuous.[114,116,118,119] These require the relation of amplitude as

$$A_i = A_r + A_f \tag{2.11}$$

and

$$A_i k_i = A_r k_r + A_f k_f \tag{2.12}$$

The wavenumber in vacuum and in the material is denoted by $k = |\mathbf{k}_i| = |\mathbf{k}_r| = 2\pi/\lambda$, and $nk = |\mathbf{k}_f|$ respectively. Now considering the specular condition i.e., $\theta_i = \theta_r$, the components of $\mathbf{k}$ parallel and perpendicular to the surface can be written as

$$(A_i + A_r)k\cos\theta_i = A_f(nk)\cos\theta_f \tag{2.13}$$

and

$$(A_i - A_r)k\sin\theta_i = A_f(nk)\sin\theta_f \tag{2.14}$$

respectively. Using Eq. 2.12 and Eq. 2.14 Snell's law can be derived as

$$\cos\theta_i = n\cos\theta_f \tag{2.15}$$

Since θ_i and θ_f are small, expanding the cosine functions gives,

$$\theta_i{}^2 = \theta_f{}^2 + 2\delta - 2i\beta = \theta_f{}^2 + \theta_c{}^2 - 2i\beta \tag{2.16}$$

where the value of n has taken from equation 2.4. Using Eq. 2.12 and Eq. 2.15 one can obtain the equation

$$\frac{A_i - A_r}{A_i + A_r} = n\frac{\sin\theta_f}{\sin\theta_i} \cong \frac{\theta_f}{\theta_i} \tag{2.17}$$

from which the reflected amplitude r and transmitted amplitude t can be written as,

$$r = \frac{A_r}{A_i} = \frac{\theta_i - \theta_f}{\theta_i + \theta_f} \tag{2.18}$$

and

$$t = \frac{A_t}{A_i} = \frac{2\theta_i}{\theta_i + \theta_f} \tag{2.19}$$

In the case of specular reflectivity, $\theta_i = \theta_r = \theta$ and only non-vanishing wave-vector transfer component $q_z = k_{f,z} - k_{i,z} = \frac{4\pi}{\lambda}\sin\theta$. So, Eq. 2.19 and Eq. 2.20 can be written

in terms of wave-vector transfer q_z as,

$$r_{01} = \left| \frac{q_{z,0} - q_{z,1}}{q_{z,0} + q_{z,1}} \right| \tag{2.20}$$

$$t_{01} = \left| \frac{2q_{z,0}}{q_{z,0} + q_{z,1}} \right| \tag{2.21}$$

where $q_{z,0}$ is the wave vector transfer in vacuum (or air) and $q_{z,1}$ is the wave vector transfer in the medium which can be written as, $q_{z,1} = \sqrt{q_{z,0}^2 - q_c^2 - \frac{32i\beta\pi^2}{\lambda}}$. Now, the Fresnel reflectivity is defined as,

$$R = r_{01}.r_{01}^* \tag{2.22}$$

In terms of q_z, the reflectivity can be written as,

$$R(q_z) = \left| \frac{q_z - \sqrt{q_{z,0}^2 - q_c^2 - \frac{32i\beta\pi^2}{\lambda}}}{q_z + \sqrt{q_{z,0}^2 - q_c^2 - \frac{32i\beta\pi^2}{\lambda}}} \right| \tag{2.23}$$

For the large wave vector compared to q_c, i.e.; $q_z > 3q_c$, the Fresnel reflectivity follows an asymptotic behavior given by,

$$R(q_z) = \frac{q_c^4}{16q_z^4} \tag{2.24}$$

Therefore, for high value of q_z, the reflectivity for an ideally sharp interface will vary with q_z^{-4}.

In case of stratified media or multilayers, the reflectivity is calculated by applying the boundary conditions for electric and magnetic fields at each of the interfaces between the slabs of constant electron density. For example, in the case of a thin film of finite thickness d, there are two interfaces, namely film-air (at $z = 0$) and film-substrate (at $z = d$) interfaces (shown in Fig. 2.5). Applying boundary conditions at these two interfaces we obtain the reflection coefficient for the film-substrate interface as,

$$r_{23} = \frac{q_{z,2} - q_{z,3}}{q_{z,2} + q_{z,3}} exp[-iq_{z,2}d] \tag{2.25}$$

where the extra phase factor comes from the applying boundary condition at $z = d$.

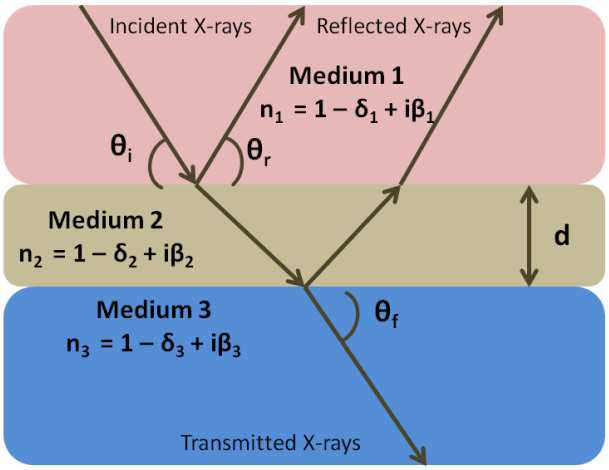

Figure 2.5: Schematic representation of incident, reflected and refracted X-ray beam from a thin film sand-witched between air and substrate.

Now using matrix method[114] or by solving the simple algebra noting the fact that r_{21} = -r_{12} the reflectance from this thin film-substrate system can be written as,

$$r_0 = \frac{r_{1,2} + r_{2,3}}{1 + r_{1,2}r_{2,3}} \tag{2.26}$$

The above formalism is easily extendable for the estimation of reflectivity for a system having N such thin films (stratified media) of thickness d_n having smooth interfaces (shown in Fig. 2.6). A set of simultaneous equations similar to Eq. 2.27 is solved to arrive at a recursive formula given by,[120,121]

$$r_{n-1,n} = \frac{r_{n,n+1} + F_{n-1,n}}{1 + r_{n,n+1}F_{n-1,n}} exp[-iq_{z,n}d_n] \tag{2.27}$$

where

$$F_{n-1,n} = \frac{q_{z,n-1} - q_{z,n}}{q_{z,n-1} + q_{z,n}} \tag{2.28}$$

To obtain the specular reflectivity of this system, one solves this recursive relation given by Eq. 2.28 from the bottom layer with the knowledge that $r_{n,n+1} = 0$, since the thickness of this medium (substrate thickness) can be taken as infinite and also the thickness d_0 of vacuum or air is infinite. The calculation of reflectivity for stratified homogeneous media having smooth boundary using the above formalism is not only used

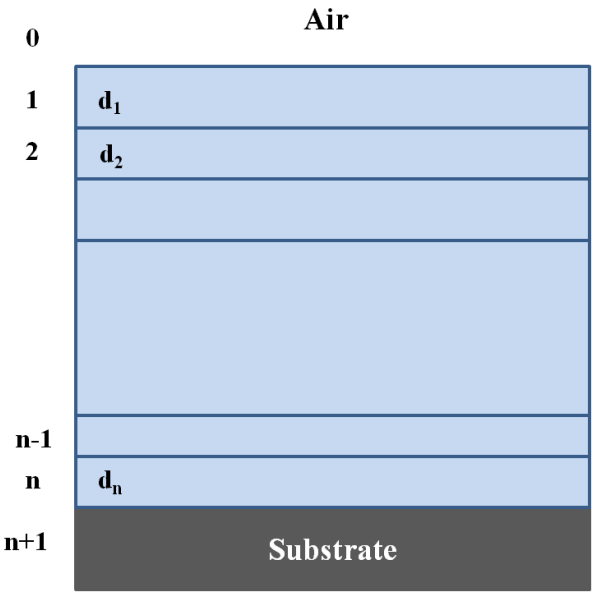

Figure 2.6: Illustration of propagation of X-ray in stratified medium.

extensively for the multilayer films, but also widely used to approximate realistic continually varying electron density profiles simply by subdividing the continuous electron density of the film into series of discrete layers.[117]

The approach so far is based on the assumption of infinitely smooth surfaces and interfaces, but the formalism needs to be modified to include the concept of roughness. The roughness is a measure of the texture of a surface. It is quantified by the vertical deviations of a real surface from its ideal form. However, it is to be noted that roughness is different from waviness of a/an surface/interface which is clearly evident when the variation of electron density is plotted as a function of depth (z-axis). In the length scale probed by X-ray (few Å), the density profile for rough surface will be a slowly varying function but the profile for the surface having waviness will be sharp one. Roughness for solid films can vary from few tens of Å for a very rough film to few Å for films grown in molecular beam epitaxy technique.

For rough surfaces or interfaces it is known that reflectivity is smaller than the smooth surface and this deviation increases with q_z. One can calculate the effect of roughness by approximating the electron density profile with a series of discrete layers as discussed above and using iterative scheme of equation. For most of the case,

the scattering profile can be approximated as a Gaussian function and by using Born Approximation[122] the reflectivity of a rough surface can be written as,

$$r_{n-1,n} = r^F_{n-1,n} exp[-iq_{z,n-1}q_{z,n}\sigma^2_{n-1,n}/2] \tag{2.29}$$

The parameter σ_n is the measure of the roughness between $(n-1)^{th}$ and n^{th} interfaces, and it is seen that roughness acts as a Debye-Waller like factor.[119] σ_n is actually the Root Mean Square (RMS) fluctuation of the interface with respect to the average interface. Equation also explains the observation that the reflectance of rough surface $r_{n-1,n}$ deviates more from the reflectance for smooth surface $r^F_{n-1,n}$ as $q_{z,n-1}$ and $q_{z,n}$ increases with $q_{z,0}$ or q_z. For a surface separating two media as shown in Fig. 2.4 can be simplified as[123]

$$R_{rough} = R_f exp[-q_z^2\sigma^2_{1,2}] \tag{2.30}$$

where R_F is the Fresnel reflectivity given in equation and $\sigma_{1,2}$ represents surface roughness at the interface of the two media. In general, the roughness of the film surface brings down the reflectivity curve faster while the roughness of the interface of the film and the substrate reduces the amplitude of multilayer peaks.

Resolution function: It is assumed in the calculation of reflectivity from flat surfaces in stratified medium that the beam is perfectly monochromatic; has no wavelength dispersion, the beam has no angular divergence and the detector is the point detector. But in the experimental reflectivity data all these factors are taken into account before going into rigorous analysis. In order to do so, the calculated reflectivity profile has to be convoluted with a resolution function.[120] The resolution mainly depends on the wavelength dispersion ($\Delta\lambda/\lambda$), the angular divergence of incoming beam ($\Delta\theta_i$) and the acceptance of the outgoing beam ($\Delta\theta_f$). In the usual geometry of XR experiments, the aperture of the detector slits perpendicular to the scattering plane is kept wide open so that the scattered intensity in the q_y direction is integrated out. With reference to Fig. 2.4, the wavevector transfer q can be resolved into two components in the x-z system

of coordinates as,

$$q_x = 2\pi/\lambda(\cos\theta_r - \cos\theta_i) = k_0(\cos\theta_r - \cos\theta_i) \tag{2.31}$$

$$q_z = 2\pi/\lambda(\sin\theta_i + \sin\theta_r) = k_0(\sin\theta_i + \sin\theta_r) \tag{2.32}$$

where $k_0 = 2\pi/\lambda$. Differentiating the equations with respect to θ_i and θ_r, we obtain

$$dq_x = k_0(\sin\theta_i d\theta_i - \sin\theta_r d\theta_r) - dk_0(\cos\theta_i - \cos\theta_r) \tag{2.33}$$

$$dq_z = k_0(\cos\theta_i d\theta_i + \cos\theta_r d\theta_r) + dk_0(\sin\theta_i + \sin\theta_r) \tag{2.34}$$

where dk_0 = -$k_0 d\lambda/\lambda$.

With the assumption that $d\theta_i$ and $d\theta_r$ are randomly distributed, the resolution widths in q_x and q_z are given by

$$\Delta q_x^2 = k_0^2(\sin^2\theta_i \Delta\theta_i^2 + \sin^2\theta_r \Delta\theta_r^2) + \Delta k_0^2(\cos\theta_i - \cos\theta_r)^2 \tag{2.35}$$

$$\Delta q_z^2 = k_0^2(\cos^2\theta_i \Delta\theta_i^2 + \cos^2\theta_r \Delta\theta_r^2) + \Delta k_0^2(\sin\theta_i + \sin\theta_r)^2 \tag{2.36}$$

In the specular condition i.e., $\theta_i = \theta_f = \theta$ and neglecting the effect of the wavelength dispersion as compared to the angular spread, the above equation are given by

$$\Delta q_x = k_0 \sin\theta[(\Delta\theta_i^2 + \Delta\theta_r^2)]^{1/2} \tag{2.37}$$

$$\Delta q_z = k_0 \cos\theta[(\Delta\theta_i^2 + \Delta\theta_r^2)]^{1/2} \tag{2.38}$$

Defining $[(\Delta\theta_i^2 + \Delta\theta_r^2)]^{1/2}$ as the half-width at half-maximum (HWHM), σ_d, of the direct beam, we can write

$$\Delta q_x = q_z \sigma_d/2 \tag{2.39}$$

$$\Delta q_z = k_0 \sigma_d \cos\theta \tag{2.40}$$

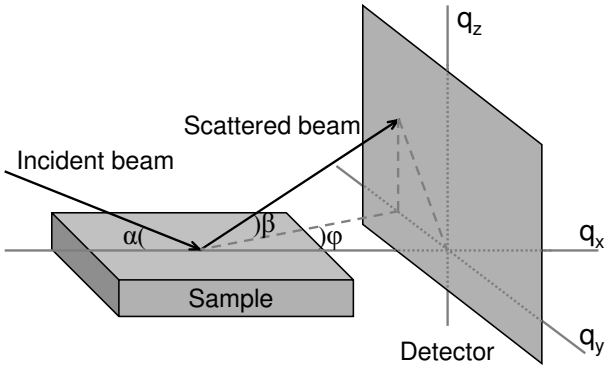

Figure 2.7: Schematic of the scattering geometry used to perform GISAXS measurements.

2.2.1.3 Grazing incidence small angle x-ray scattering

The grazing incidence small angle x-ray scattering (GISAXS) geometry used for characterization of the samples is shown schematically in Fig. 2.7. The surface of the sample is in the $x-y$ plane and the incident x-ray beam (of wavelength λ) is in the $x-z$ plane. α is the incident angle with the $x-y$ plane and β and φ are the exit angles with the $x-y$ and $x-z$ planes, respectively.

In GISAXS technique, we can measure the diffuse scattering around the specularly reflected beam at fixed incidence angle α. The scattering angles (β and ϕ) are related to the components of the wave vector transfer,[114] $\overrightarrow{q}(q_x, q_y, q_z)$, by the following relations

$$q_x = (2\pi/\lambda)(\cos\beta\cos\varphi - \cos\alpha) \tag{2.41}$$

$$q_y = (2\pi/\lambda)(\cos\beta\sin\varphi) \tag{2.42}$$

and

$$q_z = (2\pi/\lambda)(\sin\beta + \sin\alpha) \tag{2.43}$$

In a conventional GISAXS experiment, the recorded data as function of β and ϕ are labeled and analyzed as a map of the (q_y, q_z) reciprocal plane. A typical GISAXS pattern is made of two sharp peaks due to the transmitted and specularly reflected beams, of an intense specular rod and of diffuse scattering. The $z = 0$ sample surface is called the horizon while an enhancement of scattering, the so-called Yoneda peak, is

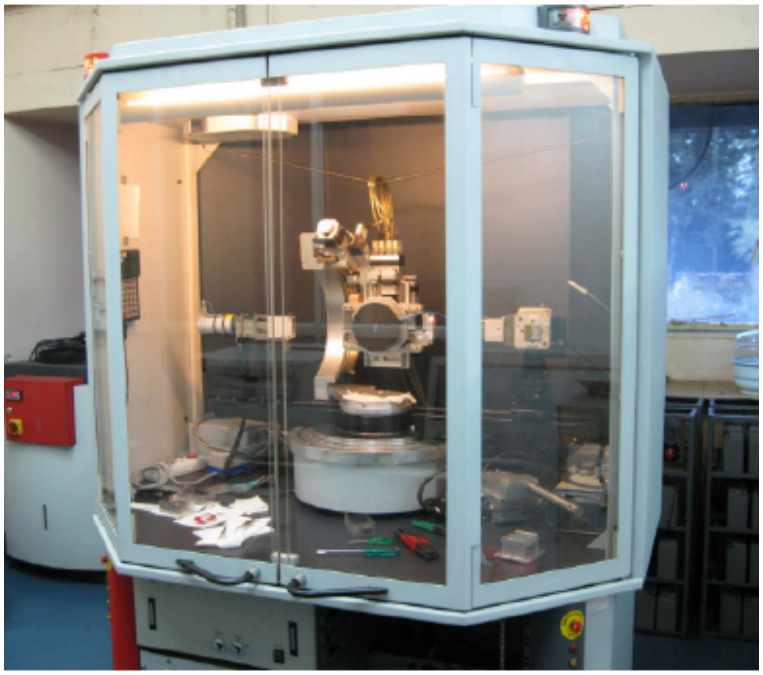

Figure 2.8: The VXRD instrument used in our experiment for XR measurements.

found at an exit angle β close to the angle of total external reflection α_c. Most often, a GISAXS experiment does not consider the specular reflection and focuses only on the diffuse scattering.

We are mainly interested to find out the in-plane structure of the mesostructured film which can be derived from the Bragg spot present in the $q_y - q_z$ reciprocal space in GISAXS pattern. To locate the exact position of Bragg spot does not need any theoretical calculation related to GISAXS. So we don't go details into the calculation.

2.2.1.4 Facility: Laboratory source

XR measurements were carried out with versatile X-ray diffractometer (VXRD) (D8 Discover, Bruker AXS, Germany) which is shown in Fig 2.8. In VXRD, a Cu sealed tube generates X-rays of the required radiation energy, focal spot and intensity by bombarding the target sample with electrons generated from the filament (cathode). The focal spot (also called focal spot on target) and takeoff angle are critical features in the production of X-rays by sealed tube. The area bombarded by electrons is called focal spot on target and the angle between the primary X-ray beam and the surface is called

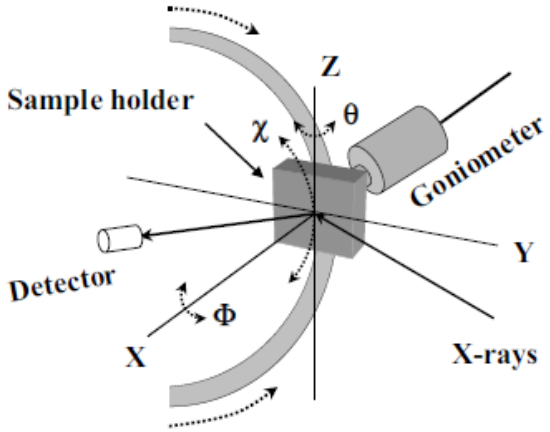

Figure 2.9: Rotation geometry of the θ, ϕ and χ motors in VXRD setup with 1/4 Eulerian cradle.

takeoff angle. The takeoff angle can be set from 3° to 7°. In this system the normal emission angle is 5°. Sealed tube normally has 2 to 4 beryllium windows through which X-rays exit. The focal spot is typically rectangular in shape with a length-to-width ratio of 10 to 1. The projection along the length of the focal spot at a takeoff angle from the anode surface is called spot focus. For fine focus the focal spot size at anode is 0.4×8 mm^2 and spot focus size is 0.4×0.8 mm^2. The emerging primary X-rays then passes through the beam optics components consisting of a monochromator, a pinhole collimator and a Göbel mirror. A graphite crystal monochromator is typically used which gives the strongest beam intensity but cannot resolve the $K_{\alpha 1}$ and $K_{\alpha 2}$ lines. So it is aligned to K_α line of wavelength $\lambda = 1.54$ Å. X-rays of other wavelengths are filtered out by the monochromator. The monochromatized X-ray beam then passes through a parabolic multilayer mirror which is called Göbel mirror. The Göbel mirror is the bent gradient multilayer optics. The standard lengths of the multilayer optics are 40 mm and 60 mm. This mirror converts the divergent beam emitted from the X-ray source into a intense parallel beam. These special diffractive properties are valid for the Kα radiation of the source, so that the mirror is mainly diffracting the Kα part of the spectrum.

In VXRD setup, a high-precision, two-circle goniometer with independent stepper motors and optical encoders for θ and 2θ circles is used. The sample stage is usually mounted on the inner θ circle of the goniometer. The goniometer can be used in hori-

zontal θ-2θ, vertical θ-2θ and vertical θ-θ geometries. In θ-2θ mode, the sample rotation is defined as ω rotation and the sample stage directly mounted on the goniometer inner circle is called ω-stage. The used sample stage is a 1/4-circle Eulerian cradle. This cradle has two rotational (χ and ϕ) and three translational (X, Y and Z) motions. The corresponding θ, ϕ and χ motors movement have been shown in Fig. 2.9

In this setup, the sample stage contains a 5 inch vacuum chuck connected to a rotary pump to hold the sample placed on it during its movements. The instruments is associated with ERL2000 cooling water unit chiller to maintain the source at a constant temperature. The movements of all parts of the instrument are operated with software controlled stepper motors. The scattered beam from the sample is detected using NaI scintillation (point) detector. The detector interface board generates high voltage required for the operation of scintillation and proportional counters. It contains a high speed pulse amplifier with a pulse shaping stage, line shift correction and baseline restoration unit and also two discriminator windows including complete pulse counting unit. In addition there is a digital count input for various kinds of detectors having digital pulse output. The VXRD unit is kept in a radiation protection housing shown in Fig. . A lead glass window at the front of the radiation protection housing enables the samples to be changed and or the diffractometer mounts to be modified. The window shutter of the X-ray tube stand closes automatically when this window is opened. Two red LEDs light up when the window shutter is open and a green LED lights up when the window shutter is closed.

In our study data were taken in the specular condition, i.e. the incident angle is equal to the reflected angle and both are in a same scattering plane. In this condition $\varphi = 0$ and $\alpha = \beta = \theta$. Under such condition there exists a nonvanishing wave vector component, q_z, which is equal to $(4\pi/\lambda)\sin\theta$ with resolution 0.003 Å^{-1}. The qualitative idea about the samples has been obtained from the Kiessig fringes of the XR profiles. To get a quantitative information i.e., in-plane $(x - y)$ average electron density (ρ) as a function of depth (z) in high resolution,[55] all XR profiles have been analyzed using Parratt's formalism [121] from which one can estimate the total film thickness, the average porosity and the film-substrate interface. For the analysis, each film has been divided

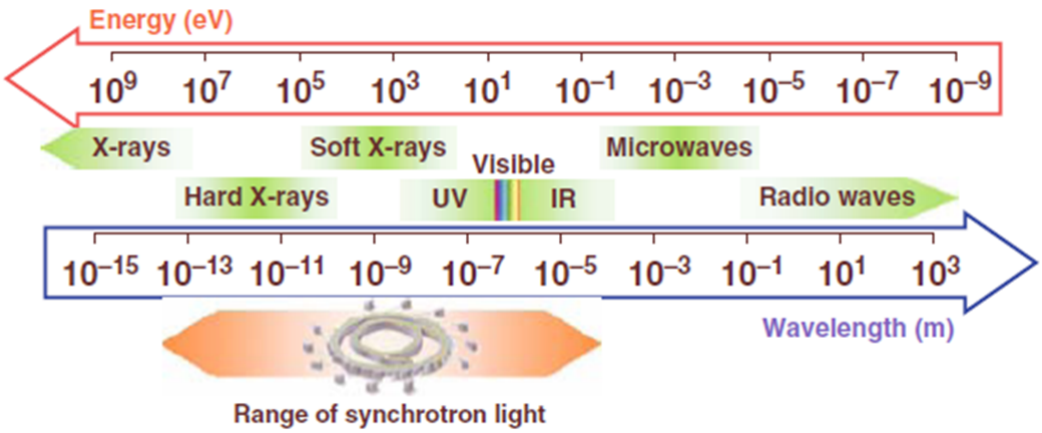

Figure 2.10: Energy and wavelength scales for a very large range of the electromagnetic wave field. On the lower part the large spectral region covered by the synchrotron radiation is highlighted.

a into number of layers and roughness has been incorporated at each interface. The thickness, electron density, and roughness associated with each layer were then set as fitting parameters.

2.2.1.5 Facility: Synchrotron source

Nowadays, the availability of intense X-rays from the modern synchrotron sources have accelerated the usage of X-rays in the determination of interfacial structures of solids. Specially, GISAXS measurements performed at laboratory sources are very limited due to poor beam intensity. The full potential of GISAXS is realized with using a synchrotron radiation source in combination with two-dimensional detectors (CCD detector or image plate). So, we have performed GISAXS measurements at synchrotron radiation which is absolutely necessary to know the complete structure of the film.

Synchrotron radiation takes its name from a specific type of particle accelerator. It is known that a charged particle constrained to move in curved path experiences a centripetal acceleration. Due to it, the particle radiates energy according to Maxwell equations. A non-relativistic particle emits radiation primarily at its frequency of revolution. However, as the speed of the particle approaches the speed of light, the radiation pattern is distorted by relativistic effects and shrinks to a narrow cone. The latter type of radiation is called synchrotron radiation or SR in short. Generally, in synchrotron source,

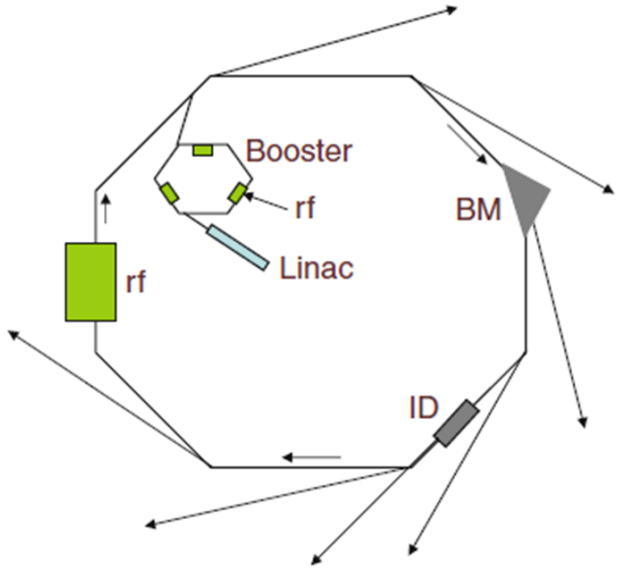

Figure 2.11: Schematic view of a synchrotron radiation source. The injection-accelerating system (LINAC+Booster synchrotron) is inside the storage ring with the bending magnets at their vertices. Insertion devices, ID, can be allocated in the straight sectors to produce specific synchrotron light. The radio frequency (rf) cavity of the storage ring and those of the booster synchrotron are also indicated.

photons or light (electromagnetic wave) is generated by acceleration of ultra-relativistic electrons in a curved path through magnetic fields. The spectrum of synchrotron light reaches from the far infrared up to near gamma rays, the radiation is highly polarized and the intensity greatly exceed other sources. With these properties, SR has proven to be useful in a large number of physical, chemical, geological, and biological processes. Generally, a X-ray beam is characterized by its Brilliance, which is used to compare the quality of the beam produced from different sources. The Brilliance, which is a function of photon energy is defined as,[119]

$$\text{Brilliance} = \frac{\text{Photons/second}}{(\text{mrad}^2)(\text{mm}^2\text{source area})(0.1\%\ \text{bandwidth})} \tag{2.44}$$

The main components of a synchrotron radiation source are - the injection and accelerator system, the storage ring, insertion devices and beam controls.[124,125]

The injection system consists of an electron source, a low energy linear accelerator (LINAC), and a booster synchrotron (circular accelerator) where the electrons reach

the operating energy, in one turn, before being transferred to the storage ring in a synchronized way. To reach high beam intensities in the storage ring, many booster pulses are injected. The process begins in the electron gun where high voltage electric field through a heated metallic cathode produces pulses of electrons which are directed toward the LINAC. In the LINAC, the electrons enter into the first radio frequency cavity which accelerates them and at the same time groups them into bunches. The electrons pre-accelerated in the LINAC are addressed by a bending magnet toward a circular accelerator (booster synchrotron) where they are strongly accelerated to reach the final energy in the range of several giga-electron-volts (GeV) before being transferred to the storage ring. The booster synchrotron is a sequence of both bending magnets and focus-defocus magnets and radiofrequency cavities along the circle.

A storage ring is a circular ring, whose structure is essentially the same as a synchrotron, and in which the electrons are kept circulating at constant energy for more than several hours. A storage ring comprises vacuum chambers for keeping an ultra-high vacuum along the particle trajectory, magnets for bending and focusing the circulating beam and radio frequency accelerating cavities for making up for energy lost as synchrotron radiation, and .

A low pressure ($< 10^{-9}$ torr) in the whole vacuum chamber is required for survival of the electron beam. Due to gas desorption caused by the radiation hitting the vacuum chamber surface a continuous pumping is required and it is carried out by placing many vacuum pumps along the circular path.

The magnetic system consists of bending magnets and focusing quadrupole and sextupole magnets. Dipole magnets are arranged along the electron orbit to modify the trajectory of the electron beam. The magnetic field of the magnets is kept constant in the storage ring because the electron beam energy has to be kept constant. There are photon beam ports at the location of the dipole magnets so that the synchrotron radiation may be utilized. Between the dipole magnets on the straight beam line section there are quadrupole magnets, which provide magnetic fields with gradients to act as lenses for the electron optics system. Sextupole magnets are used to correct the chromatic aberrations caused by focusing errors because of energy spread of electrons within a

bunch. The electron beam is maintained in a stable oscillation (betatron oscillation) around an equilibrium orbit by the lens action with the magnets.

In the arc sections of the storage ring, the electron beam loses energy by emitting synchrotron radiation. This energy loss is supplied by radio frequency cavities, which are set up on a straight section of the ring, and an associated power supply.

Synchrotron radiation emitted from bending magnets does not always meet all requirements of the users. In order to provide the desired radiation characteristics (photon energy, broad band, narrow band, etc.) **insertion devices** are placed on the magnet-free sections (straight sectors) along the orbit. An insertion device comprises periodic magnets, whose polarity alternates periodically in the direction of motion of the electron beam. Therefore, the trajectory of electrons inside the insertion device wiggles like a section of sinusoidal curve. Furthermore, the insertion devices can be turned on or off without affecting the functioning of the storage ring. The insertion devices are wavelength shifters, wigglers, and undulators. In a wiggler the amplitude of the oscillations is rather large and the radiation from different wiggles add incoherently, whereas in undulators, the small-amplitude oscillations from the passage of a single electron produce a coherent addition of the radiation from each oscillation.

Beam controls are used to measure the circulating beam current, beam lifetime, and transverse beam position.

The synchrotron radiations generated in the bending magnets or insertion devices are taken from the ports of the ring and delivered to the experimental station through a beam line. The main beam line is a light-path connecting the storage ring and the experimental station, and performs the function to extract or cut off the photon beam. Various kinds of optical instruments, such as reflection mirrors and monochromators, are set up in the beam line according to the characteristics of the synchrotron radiation to be used and the purpose of the experiment. A standard synchrotron beamline consists of the following components:

Monochromator: For X-rays, silicon and germanium crystals are used as monochromators. The purpose of these crystals is to extract a particular wavelength or energy from the white X-ray beam. This is done by impinging the white beam on the crystals

Table 2.1: Specifications of the synchrotron beamlines use for GISAXS measurements

Beamline	SAXS beam line Elettra, Italy	MiNaXS beam line PETRA III, DESY, Germany
Source	Wiggler	Undulator
Energy (keV)	8	11.4
Monochromator	Double crystal Si (111)	Double crystal Si (111)
Detector	30cm diameter image plate mar300, Marresearch GmbH	CCD detector, PILATUS 1M, Dectris
Image area (pixels)	2000×2000	981×1043
Pixel size (μm)	150	172
Sample to detector distance (cm)	90	171
Incident angle	0.5-0.6°C	0.25°C

whose lattice planes diffract the X-rays of different energies in different directions in accordance with Bragg's law. In order to re-direct the diffracted beam along the incident one, another similar crystal parallel to the first is used. Monochromators with such kind of crystal arrangements are known as *double crystal monochromators*.

Windows: Thin sheets of metal, often Beryllium, which transmit almost all of the beam, but protect the vacuum within the storage ring from contamination, are generally used as windows.

Slits: In order to define both the horizontal and vertical beam size, several slits are used before impinging the beam on a sample of interest.

Focussing mirror: One or more mirrors, which may be flat, bent-flat, or toroidal are used to collimate or focus the X-ray beam. Specialized lenses are also used.

Spacing tubes: Vacuum tubes which provide the proper space between optical elements, and shield any scattered radiation, are generally used in beamlines.

We have performed GISAXS measurements at SAXS beam line, Elettra, Italy and MiNaXS beam line (P03) at the third generation synchrotron source PETRA III of Deutsches Elektronen-Synchrotron (DESY), Germany. The specifications and experimental details of these beamlines maintained during measurements are summarized in Table 2.1.

2.2.2 Dynamic light scattering

2.2.2.1 Basic Formalism

Dynamic light scattering (DLS) also known as photon correlation spectroscopy (PCS) or quasi-elastic light scattering (QELS) is a technique that can be used to determine the size distribution profile of small particles or polymer typically in the sub-micron region suspended within a liquid. It measures the intensity fluctuations of the scattered light as a function of time and relates this to the size of the particles.[126–128] Shining a monochromatic light beam, such as a laser, onto a solution with spherical particles the light scatters in all directions (Rayleigh scattering) as long as the particles are small compared to the wavelength (below 250 nm) of the light beam. Due to the Brownian motion of the particles in the scattering volume the distance between the scatterers in the

solution is constantly changing with time and that results to the intensity fluctuation of the scattered light with time. This intensity fluctuations ($I(q,t)$) with time is expressed in terms of the time correlation functions which include the time scale of movement of the scatterers present in the solution. From this fluctuation, the intensity autocorrelation function is measured using a hardware correlator, where the time dependent scattered intensity is multiplied with itself after it has been shifted by a distance in time τ, and this quantity is then averaged over the total measurement time. The intensity autocorrelation function $\langle I(q,t)I(q,t+\tau)\rangle$ is calculated for various τ values. In a typical dynamic light scattering experiments this τ value ranges from 100 ns to several seconds.

The normalised autocorrelation function $g_2(q,\tau)$ is given by

$$g_2(q,\tau) = \frac{I(q,t)I(q,t+\tau)}{I(q,t)^2} \tag{2.45}$$

The amplitude correlation function or the dynamic structure factor is denoted as $g_1(q,\tau)$ and correspondingly the Siegert relation can be written as,[128]

$$g_2(q,\tau) = 1 + \beta g_1(q,\tau)^2 \tag{2.46}$$

where, β is a constant related to the coherence of the detection optics. For mono-disperse samples, $g_1(q,\tau)$ is a single exponential decay function with decay rate Γ given by

$$\Gamma = D_s q^2 \tag{2.47}$$

where q is the scattering wave vector and D_s is the translational diffusion coefficient. D_s can be calculated using Stokes-Einstein equation given by

$$D_s = \frac{kT}{f} = \frac{kT}{6\pi\eta R_H} \tag{2.48}$$

Using this equation we can determine the hydrodynamic radius R_H of the scattering particle if the temperature of the sample T and viscosity of the solvent η at that temperature are known.

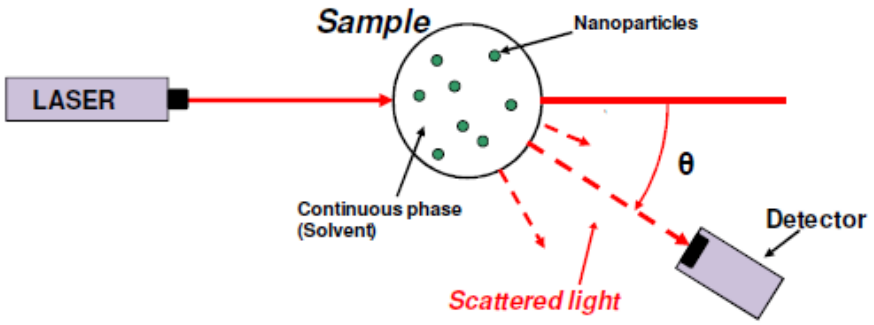

Figure 2.12: Illustration of DLS principle.

2.2.2.2 Instrument

To perform DLS experiment we have used the instrument, Zetasizer Nano-s, Malvern Instruments Ltd., Malvern, UK. The instrument has four main components:
- a light source (4 mW HeNe laser of wavelength 633 nm) to illuminate the scatterer
- an avalanche photodiode detector
- a peltier temperature controller which can change the temperature form 2 to 92°C
- a sample containing 5 ml glass cell.

The operation principle of the instrument is shown in Fig. 2.12. The light source illuminates the sample solution contained in the glass cell and it is scattered at all angles. The detector is used to measure the scattered light at a fixed scattering angle (173° backscatter).

2.2.3 Contact angle measurement

2.2.3.1 Basic Formalism

Contact angle (CA) is a quantitative measure of the wetting of a solid by a liquid which provide the information about the adhesion, surface energy, or hydrophilicity/hydrophobicity of that solid surface. It is defined geometrically as the angle between a tangential to the liquid surface at the three phase boundary where a liquid, gas and solid intersect and the plane of the solid surface (either real or apparent) on which liquid resides or

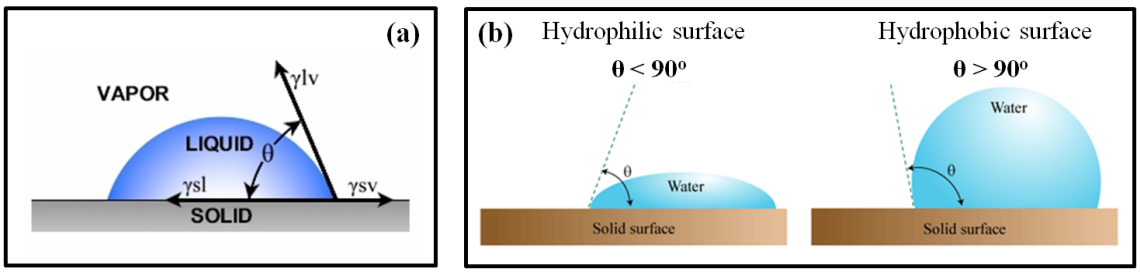

Figure 2.13: (a) Schematic of a liquid drop showing the quantities in Young's equation used for CA measurement. (b) Illustration of contact angles formed by hydrophilic and hydrophobic surfaces.

move (shown in Fig. 2.13(a)). The contact angle (θ) can be theoretically defined by the famous Young's equation describing the interactions between the forces of cohesion and adhesion[129]

$$\gamma_{sv} = \gamma_{lv} \cos\theta + \gamma_{sl} \tag{2.49}$$

where γ_{sv}, γ_{lv} and γ_{sl} represent the solid-vapor, liquid-vapor and solid-liquid interfacial free energy, respectively. Generally, in the case of water if the contact angle on a solid surface is smaller than 90°, then the solid surface is considered as hydrophilic. This condition reflects better wetting, better adhesiveness and higher surface energy. On the other hand, if the water contact angle on a solid surface is higher than 90° the surface is termed as hydrophobic. This condition is described by poor wetting, poor adhesiveness and lower free energy of the solid surface.

This relation is formally applicable only on surfaces that are physically smooth and chemically homogeneous and the state of the system is an equilibrium state. In a real experimental situation, it is practically impossible to have such a surface. Conversely, real surfaces always present roughness and heterogeneity. This leads to irregular drop shapes and the meniscus profile is not fully equivalent to the *equilibrium* meniscus and the system is not in its lowest energy state. Consequently, the result of CA measurement may be any one of a great number of possible contact angles that all fall into a more or less wide interval, characteristic for the system. These have been interpreted as metastable states, corresponding to local minima of the overall free energy of the system. Among them, the only identifiable ones are the extremes of the interval: the major and

minor observable contact angle values which are called dynamic contact angles (all others are static contact angles). In particular, the measured contact angle value higher or lower than the equilibrium contact angle value is commonly called advancing contact angle (θ_a) or receding contact angle (θ_r), respectively. The difference between these two contact angle is called the contact angle hysteresis (H):[130,131]

$$H = \theta_a - \theta_r \tag{2.50}$$

Though measurements of advancing and receding contact angle is the most popular and appropriate technique in wetting characterization of solids, but there are some other useful forms of contact angle like equilibrium contact angle and as-placed contact angle which are used in a variety of fields.[132,133] Equilibrium contact angle refers to the angle measured for a liquid at a solid surface (smooth or rough, flat or curved and homogeneous or heterogeneous) after the entire solid-liquid-fluid system reaches the absolute minimum in its total free energy. On the other hand, as-placed contact angle is defined as the contact angle that a liquid drop adapts as a result of its placement on a solid surface. The changes in equilibrium contact angle and as-placed contact angle is qualitatively similar.

2.2.3.2 Instrument

CA measurements were carried out using CA goniometer (250-F1, rame-hart instrument co., USA) shown in Fig. 2.14 to investigate the hydrophilic or hydrophobic nature of the samples. It can measures a wide range of contact angle (0° to 180°) with resolution 0.01°. The instrument has mainly three units - dispensing unit, viewing unit and measurement unit. The dispensing system generally consists of a 3-axis specimen stage and a micro syringe assembly together with a 22 g straight needle. The micro syringe assembly can be operated by a motorized system to hold and dispense the liquid. The specimen stage is that part of the instrument which holds the solid surface. It must be flat and level - usually built with the ability to adjust the tilt to a level position - so that the contact angle can be accurately measured. The stage is generally able to move up and down a few inches to allow the liquid to be transferred from the syringe needle to the solid

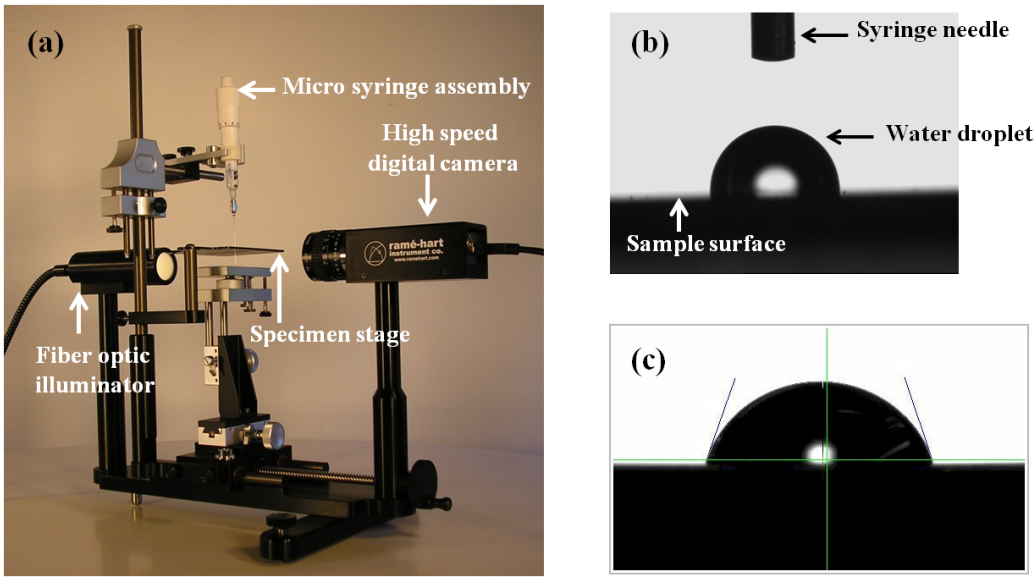

Figure 2.14: (a) The CA goniometer (250-F1, rame-hart instrument co., USA) used to measure the contact angle in our experiment. (b) Image of a contact angle of water taken from the CA goniometer. (c) Method for measuring contact angle using DROPimage Advanced software.

surface, and sometimes able to move laterally as well. The viewing system generally consists of a U1 series high-speed digital camera attached with a goniometer to magnify and capture the image of the drop sitting on the solid surface, and a light source (variable fiber optic illuminator) to illuminate the samples and enhance visibility of the outline of the drop. The camera can be operated at 100 fps. The measurement system (not shown in the figure) is the part that actually measures the contact angle from the image created with the viewing system, and is not a physical part of the instrument. This is usually done using a software program named DROPimage Advanced to trace the drop profile and calculate the angle at the contact point. With the correct calibrations these programs can provide additional information like drop volume and contact area.

For the measurement, a drop (5 μl) of water (Milli-Q) was placed on the sample surface. The CA values were noted after a minute and then 5 successive times at intervals of 20 s. Such measurements were done in more than five different regions over the sample surface. It is to be mentioned that we have not measured the advancing and receding contact angles, which are more appropriate. What we measured is the so-called as-placed CA,[132] whose changes are qualitatively similar to those of the equilibrium

CA.[134]

2.2.4 Ultraviolet-visible spectroscopy

2.2.4.1 Basic Formalism

Ultraviolet-visible (UV-vis) spectroscopy or spectrophotometry uses light in the ultraviolet (190-400 nm) and visible (400-800 nm) spectral region. This spectroscopy is used to probe the electronic transitions (transition of electrons from ground energy state to a higher energy state) of the materials and therefore is often referred to as *electron spectroscopy*. When the energy of the incident light corresponds to the energy of transition between two electronic states, this results in excitation and hence, transition of the electron from the highest occupied molecular orbital (HOMO) to the lowest unoccupied molecular orbital (LUMO). The energy that requires for the transition is absorbed from the incident light. So UV-vis spectroscopy can be classified as absorption spectroscopy.[135]

A molecule of any substance has an internal energy which can be considered as the sum of the energy of its electrons, the energy of vibration between its constituent atoms and the energy associated with rotation of the molecule.[136] The electronic energy levels of a molecule are closely spaced and photons of near ultraviolet and visible light can effect the transition of the molecule from one level to another. These substances, therefore, will absorb light in some areas of the near ultraviolet and visible regions. Since photon and electron energy levels are quantized, it is expected that the absorption spectrum of a molecule (i.e., a plot of its degree of absorption against the wavelength of the incident radiation) should show a few very sharp lines corresponding to specific allowed transitions. In practice, the lineshape of absorption spectra is normally distributed indicating that the molecule is absorbing radiation over a band of wavelengths. The reason for this band, is that an electronic level transition is usually accompanied by a simultaneous change between the more numerous vibrational levels. Thus, a photon with a little too much or too little energy to be accepted by the molecule for a *pure* electronic transition and can be utilized for a transition between one of the vibrational levels associated with the lower electronic state to one of the vibrational levels of a higher

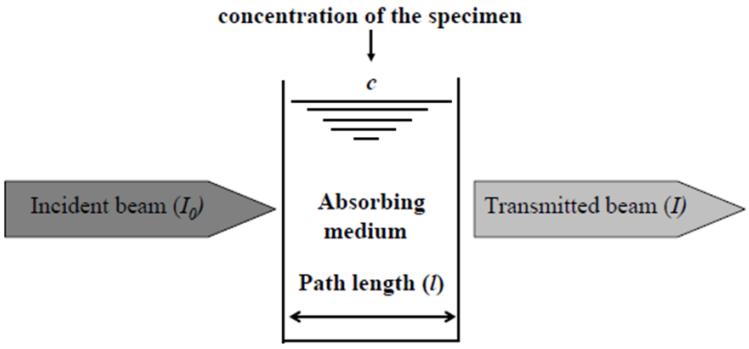

Figure 2.15: Illustration of the absorption of UV-vis radiation in a material medium of optical path length l.

electronic state. Furthermore, each of the many vibrational levels associated with the electronic states also has a large number of rotational levels associated with it. Thus a transition can consist of a large electronic component, a smaller vibrational element and an even smaller rotational change.

Metals have unique optical properties compared to other materials which is the manifestations of the conduction electrons.[137] By reducing the physical size and shape of the metal clusters this property can be modified. The optical spectra of noble-metal clusters exhibit pronounced resonance lines caused by collective oscillation/excitation of conduction electrons stimulated by incident beam. These excitations are known as surface plasmon resonance (SPR) which are known to be controlled by a variety of effects.[135,137,138] In particular, the spectral position of the particle plasmon depends on the dielectric properties of the cluster metal; for instance, silver clusters generally have higher particle-plasmon energies than gold clusters. The spectral position also depends on the size and shape of the clusters.[137–140] In addition, resonances of higher multipolar order appear beside the usual dipolar resonance when the cluster size is increased.[138] In the case of clusters of non-spherical shape, the single dipolar resonance of the spherical one splits into two or more non-degenerate plasmon modes that differ by their oscillation directions. The surrounding also affects the surface plasmon absorbance. The resonance energy gradually shifts to the red with increased refractive index of the surrounding medium,[141] and may also be increased by chemical interactions with the environment.[142] Taking the dielectric constant of the metal to be of the Drude-Sommerfield form it can

be found that the absorption spectrum has a Lorentzian shape and the full width half maxima (FWHM) of the spectrum is the inverse of the Drude scattering time. It can also be found that the width of the SPR mode is inversely proportional to the particle diameter.[137]

In the practical experiment, the intensity of the absorbed light is measured indirectly by measuring the beam intensity which is not absorbed by the sample, i.e., intensity of transmitted radiation. The Beer-Lambert law relates the transmitted intensity (I) to the incident intensity (I_0), the concentration (c) and thickness (l) of the absorption material, as shown in Fig. 2.15, by

$$A = \alpha cl = log\frac{I}{I_0} \tag{2.51}$$

where A and α are the absorbance and absorption coefficient of the absorbing species, respectively. The absorbing medium may be a solid, a liquid or a suspension of colloidal particles in a liquid medium. The absorption spectrum of a material is obtained by scanning the entire wavelength range of the incident beam and measuring the corresponding transmitted signal. In the case of a thick film where transmission is not possible, the data can be collected in reflection mode by adjoining a separate accessory. Absorption spectra can be obtained using the relation, $A + R + T = 1$, where A, R and T are the absorbance, reflectance and transmittance of the specimen. Therefore, in case of thick films we have, $T = 0$ and $A = 1 - R$.

2.2.4.2 Instrument

Spectrometer for measuring the absorption of ultraviolet or visible radiation are generally made up of the four major components:

- a continuum light source, covering a proper range of wavelength i.e. 190-1000 nm,
- a wavelength selector (monochromator) which selects the wavelength of interest,
- a sample container to hold the sample to be studied,
- a chopper which separates the light for reference beam and sample beam,
- a detector/amplifier system, which measures the amount of transmitted light.

In our experiment we have used Lambda 750 UV/Vis/NIR spectrometer, Perkin

Elmer, USA in which tungsten-halogen filament lamp and the deuterium discharge lamp are used as source of visible radiation and ultraviolet radiation, respectively. This instrument is suitable for measurements in the scanning wavelength range between 190 to 3300 nm with a resolution of 0.17 - 5.00 nm. The envelope of the lamp is normally constructed of quartz which exhibits excellent ultraviolet transmission. The radiation is then monochromatized using a double holographic grating monochromator. The double monochromator is a system of two single monochromators, in which the exit slit of the first monochromator is the entrance slit of the second one. In order to optimize the system performance holographic grating grooves with either parallel or of unequal distribution are used. Holographic gratings are generated on plano, spherical, toroidal and many other surfaces. Using this grating monochromators radiation of a narrow band of wavelengths (ultraviolet, visible, and infrared) is selected from the source light. Then the light beam passes through a beam chopper which is a rotating mirror that rotates around its own axis several times per second and during each rotation it chops the incident beam. It alternatively splits the incident beam into two halves, one passes through the sample called sample beam and the other passes through the reference called reference beam. The detector also alternates between measuring the sample beam and the reference beam in synchronism with the chopper. When light passes through the sample, the detector measures the sample beam intensity I and when the chopper diverts the beam through the blank solution, the detector measures the reference beam intensity I_0 and finally the electronic circuit automatically compares I and I_0 to calculate absorbance and transmittance.

The sample compartment in this spectrometer has a lid to protect the detector from strong external light. It accommodates samples in the form of films and liquids filled in cuvette. The cuvette for the sample and reference solution must be transparent to the radiation which will pass through them. Generally, quartz cuvette is required for spectroscopy in both UV and visible region as quartz is transparent in a wide wavelength range (190-1000nm). The most common shape of a cuvette is rectangular having a square base of edge 10 mm. The optical path length of it is 10 mm and the path width is 10 mm. This cuvette typically holds 2-3 ml of sample solution. The detector has to convert the

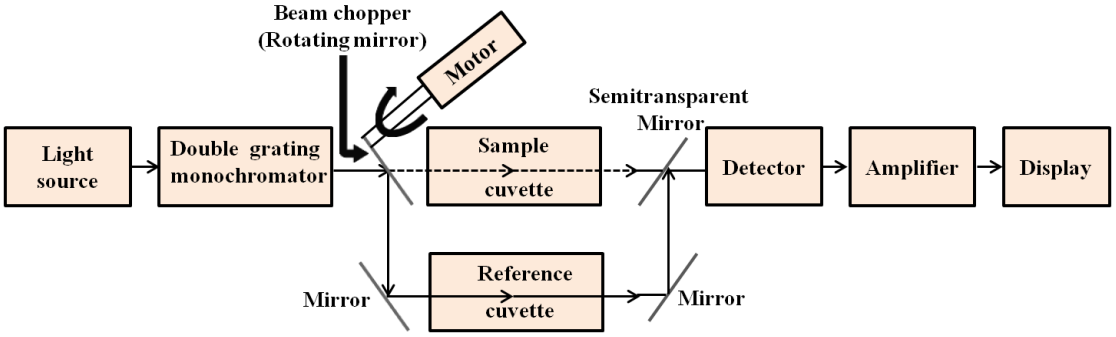

Figure 2.16: Schematic diagram of the UV-vis spectrometer (Lambda 750 UV/Vis/NIR spectrometer, Perkin Elmer, USA) used in our experiments.

radiation energy falling upon them to an electrical signal which can then be processed. Two types of detectors are used in this spectrometer - high sensitive photomultiplier tube and peltier cooled PbS detector for detection in the UV/Vis and IR range, respectively. A photomultiplier tube consists of a photoemissive cathode (a cathode which emits electrons when struck by photons of radiation), several dynodes (which emit several electrons for each electron striking them) and an anode. In this detector the resulting current is amplified using a high gain amplifier and then measured. The schematic diagram of the UVvis spectrometer used in our experiment is shown in Fig. 2.16.

2.2.5 X-ray photoelectron spectroscopy

2.2.5.1 Basic Formalism

X-ray photoelectron spectroscopy (XPS), also known as electron spectroscopy for chemical analysis (ESCA) is the most widely used surface analysis technique to study the elemental composition, empirical formula, chemical information and electronic state that exist within the surface region (first 1-30 monolayers). XPS spectra are obtained by irradiating the sample with soft X-rays (with a photon energy of 200-2000 eV) while simultaneously measuring the kinetic energy and number of electrons that escape from the top 0 to 10 nm of the material. The energy spectrum of the emitted electrons is determined by means of a high-resolution electron spectrometer.[143,144]

XPS is based on the phenomenon of photoelectric effect detected by Hertz in 1887, shown in Fig. 2.17. Each atom in the surface has core electron with the characteristic

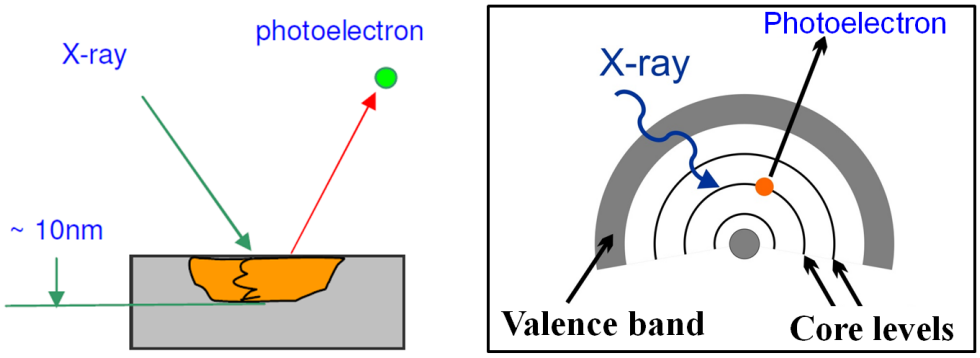

Figure 2.17: Schematic representation of the XPS process.

binding energy that is conceptually, not strictly, equal to the ionization energy of that electron. When an X-ray beam directs to the sample surface, the energy of the X-ray photon is adsorbed completely by the core electron of an atom. If the photon energy $h\nu$, is large enough, the core electron will then escape from the atom and emit out of the surface. The emitted electron is referred to as the photoelectron. The binding energy E_b of the core electron is given by the Einstein relationship,

$$h\nu = E_b + E_k + \phi \tag{2.52}$$

$$E_b = h\nu - (E_k + \phi) \tag{2.53}$$

where $h\nu$ is the X-ray photon energy, E_k is the kinetic energy of photoelectron and ϕ is the work function of the sample. In a first approximation, the work function is the difference between the energy of the Fermi level E_F and the energy of the vacuum level E_V (the zero point of the electron energy scale):

$$\phi = E_F - E_V \tag{2.54}$$

By calibration this quantity is to be determined for the spectrometer used.

The system under study (except for the hydrogen atom and hydrogenlike systems such as He^+) always contains more than one electron and therefore the system remaining after the liberation of the photoelectron still contains electrons. The final state of the

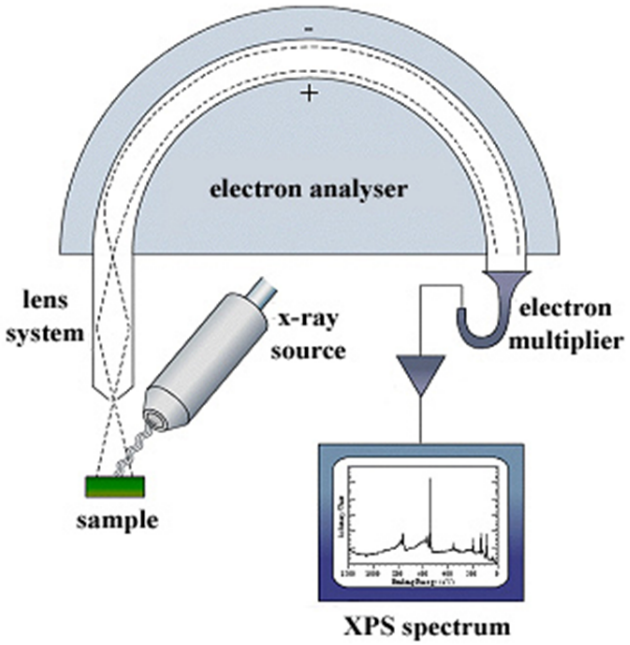

Figure 2.18: Logical layout for an XPS instrument.

photoemission process therefore has a positive hole (one electron has been removed or a positive potential has been added) that can make the final state substantially different to the initial state. In system with many degrees of freedom (many bodys/many electrons) the change can be quite complex. Therefore the theory of photoemission process for the real system is a complicated many body problem.

2.2.5.2 Instrument

The XPS instrument (Omicron Multiprobe MXPS) used for our experiments is illustrated schematically in Fig 2.18. The basic requirements for a photoemission experiment are:

- an x-ray source source of fixed-energy radiation

- an electron energy analyzer (which can disperse the emitted electrons according to their kinetic energy, and thereby measure the flux of emitted electrons of a particular energy) combined with a detection system

- a high vacuum environment (to enable the emitted photoelectrons to be analyzed without interference from gas phase collisions).

The choice of material for a soft X-ray source in XPS depends on two important considerations: (i) the line width must not limit the energy resolution required in the technique and (ii) the characteristics X-ray energy must be high enough so that a significant range of core electrons can be photoemitted for an unambiguous analysis. For our study AlK$_\alpha$ X-ray source fitted with monochromator (Model: XM 500) has been used. The whole system consist of three principle components: an X-ray source with an Al anode, an X-ray crystal mirror to select the monochromatic beam, and a set of adjustment controls. The use of monochromator helps in improving the total instrumental resolution by decreasing the linewidth of the exciting AlK$_\alpha$ (1486.7eV) radiation to about 0.25eV as compared to the value of 00.85eV for unmonochromated AlK$_\alpha$ radiation. The electron energy analyzer measures the energy distribution of the electrons emitted from the sample surface; the photoelectron spectrum is a plot of intensity versus kinetic energy. In our instrument a concentric hemispherical analyzer of 125 mm mean radius with 180° double focusing geometry (CHA; model: EA 125) has been used. The detector used in the experiment is consisting of an array of 5 channel electron multipliers. The sample analysis is conducted in a ultra-high vacuum (UHV; pressure $< 10^{-9}$ millibar) conditions. This facilitates the transmission of the photoelectrons to the analyzer but more importantly minimizes the re-contamination rate of a freshly cleaned sample. This is very important because XPS is very surface-sensitive, with a typical *sampling depth* of only a few nanometers.

For each and every element, there will be a characteristic binding energy associated with each core atomic orbital i.e. each element will give rise to a characteristic set of peaks in the photoelectron spectrum at kinetic energies determined by the photon energy and the respective binding energies. The presence of peaks at particular energies therefore indicates the presence of a specific element in the sample under study - furthermore, the intensity of the peak is related to the concentration of the element within the sampled region.

2.2.6 Transmission electron microscopy

2.2.6.1 Basic formalism

Transmission electron microscopy (TEM) has become the premier tool for the microstructural characterization of materials with very high spatial resolution particularly when particle shape and size are important. In this microscopy technique a beam of electrons is transmitted through an ultra-thin specimen and an image is formed as the result of interaction of the electrons with the specimen. By focussing the electron beam, diffraction patterns can also be measured from microscopic regions, and it is often possible to select a single microcrystal for a diffraction measurement. TEM operates on the same basic principles as the light microscope but uses electrons instead of light and their much lower wavelength (100,000 times shorter than visible light) makes it possible to get a greater resolution (about 0.02 nm) compared to that of a light microscope. TEM uses high energy electrons (up to 300 kV accelerating voltage) which are accelerated to nearly the speed of light and can achieve a magnifications upto 2,000,000×.

Electrons have both wave and particle properties and their wavelike properties mean that a beam of electrons can be made to behave like a beam of radiation. The wavelength is dependent on their energy, and so can be tuned by adjustment of accelerating fields, and can be much smaller than that of light. The wavelength of electrons accelerated by an electrical potential V is given by,[145]

$$\lambda = \frac{h}{\sqrt{2meV}} \tag{2.55}$$

where h is Planck's constant, m and e are the mass and charge of the electron, respectively. For example, electrons of 100 keV energy have wavelengths of 0.37 nm and are capable of effectively transmitting through 0.6 μm of silicon. The higher the operating voltage of TEM instrument, greater is its lateral spatial resolution.

When electrons are accelerated up to high energy levels (few hundreds keV) and focused on a material, they can scatter or backscatter elastically or inelastically, or produce many interactions, source of different signals such as X-rays, Auger electrons or light (Fig. 2.19).[145,146] Most of these signals are detected in different types of TEM and

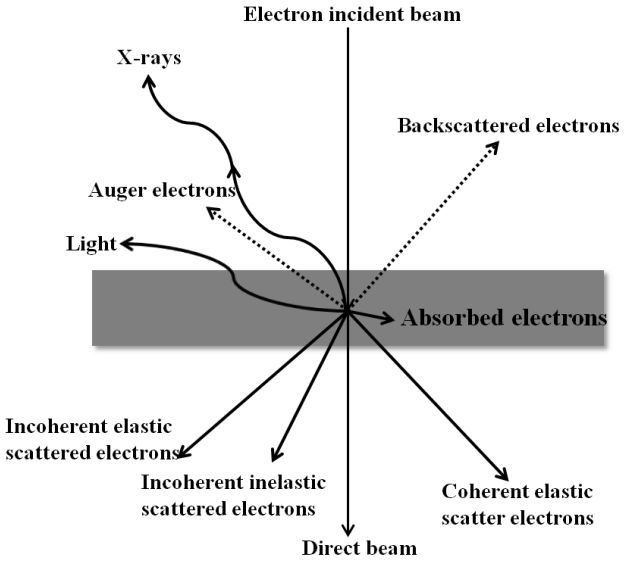

Figure 2.19: Interactions between electrons and material.

a sophisticated system of electromagnetic lenses focuses the scattered electrons into an image or a diffraction pattern depending on the mode of operation. Elastic scattering involves no energy loss and gives rise to diffraction patterns. Inelastic scattering between primary electrons and sample electrons at heterogeneities such as grain boundaries, dislocations, defects, density variations etc. cause complex absorption and scattering effect leads to a spatial variation in the intensity of transmitted electrons.[145] The type of interaction the traveling electrons face determine the mode of operation and each of these modes offers a different insight about the specimen. The most common mode of operation for a TEM is the bright field imaging mode. In this mode the contrast formation is formed directly by scattering and absorption of electrons in the sample.[146] Thicker regions of the sample, or regions with a higher electron density will appear dark, whilst regions with no sample or lower electron density regions of the sample in the beam path will appear bright-hence the term *bright field*. Selected area electron diffraction (SAED) is very useful mode to determine the crystal structure of individual nanocrystals as well as the crystal structure of different parts of a sample. In this case electrons are treated as wave-like rather than particle-like. For thin crystalline samples, this produces an image that consists of a pattern of dots in the case of a single crystal, or a series of rings for a polycrystalline or amorphous solid material. SAED patterns

are often used to determine the Bravais lattices and lattice parameters of crystalline materials by the same procedure used in XRD. By measuring the diameter of a ring or the separation between two symmetric dots on either side of the zero order central spot in the SAED pattern and knowing the camera constants, the interplanar spacing d_{hkl} can be calculated using Bragg's law which is given as,

$$2d_{hkl}\sin\theta = n\lambda \tag{2.56}$$

In modern instruments where the output is directly obtained on the computer as image data, the SAED image has an attached scale bar in units of nm^{-1} and calibrated in terms of the reciprocal space lattice vector $G = 1/d_{hkl}$.

One disadvantage of TEM is its limited depth resolution. In a TEM image the electron scattering information from a three-dimensional sample is projected onto a two-dimensional detector. Therefore, structural information along the electron beam direction is superimposed at the image plane. A further obstacle to study of organic specimen using this microscopy is the radiation damage caused by ionization and subsequent breakage of chemical bonds and finally by a loss of mass.

2.2.6.2 Instrument

A TEM has four important parts:
- electron source,
- electromagnetic lens system,
- sample holder,
- imaging system.

In our experiment, we have used two TEM instruments - JEM-2100, JEOL, USA and Tecnai 20 Super-twin, FEI, USA. The instruments have scanning-TEM (STEM) capability, with both bright-field and dark-field imaging modes, as well as both secondary-electron and back-scattered electron imaging modes. In both the instruments an intense beam of electrons is emitted from the LaB_6 filament electron gun by thermionic emission and accelerated to an energy around 200 keV corresponding to an electron wavelength of 2.5 pm. The accelerated electron beam passes though a electromagnetic lens system

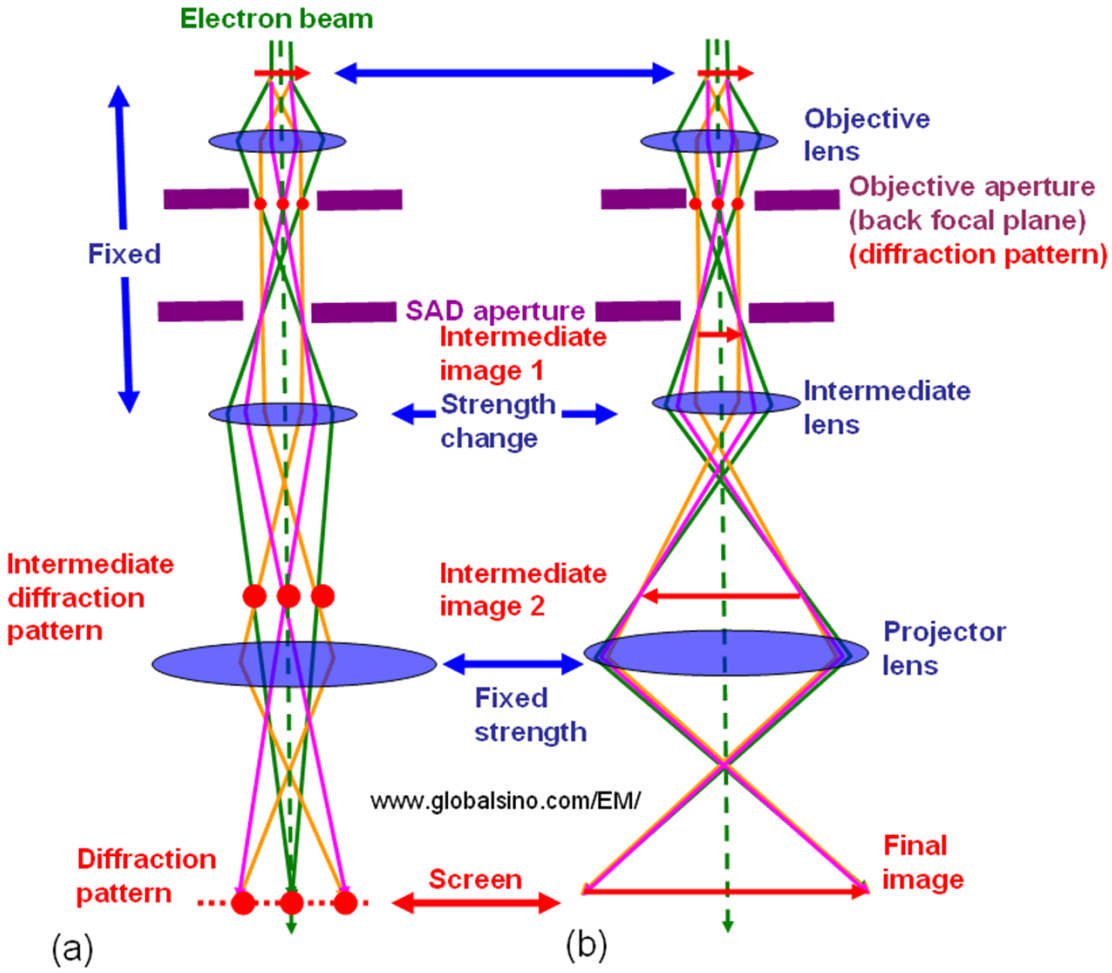

Figure 2.20: Ray diagram for a transmission electron microscope in both image and diffraction mode.

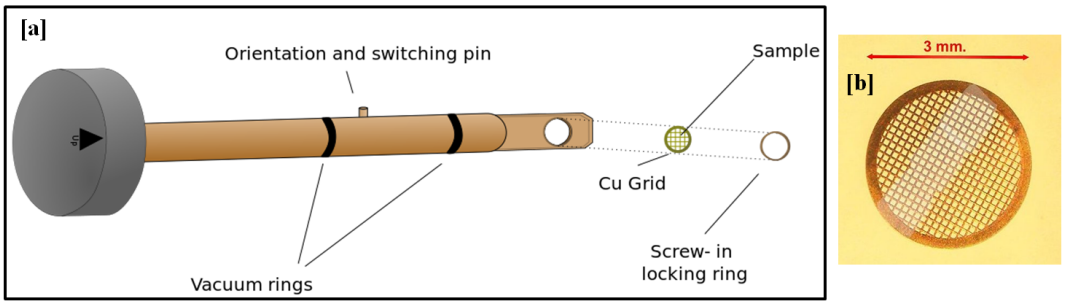

Figure 2.21: (a) A diagram of a single axis tilt sample holder for insertion into a TEM goniometer. Titling of the holder is achieved by rotation of the entire goniometer. (b) TEM sample support mesh grid.

in order to vary the illumination aperture and the area of the specimen illuminated. Finally the beam is projected onto the sample to penetrate the sample thickness either undeflected or deflected. The electromagnetic lens system is constituted of: (i) two or three condenser lenses to focus the electron beam on the sample, (ii) an objective lens to form the diffraction in the back focal plane and the image of the sample in the image plane, (iii) some intermediate lenses to magnify the image or the diffraction pattern on the screen and (iv) projector lenses projected the transmitted electron beam onto the imaging system. Both the TEMs are equipped with the high-resolution (HRP) style objective-lens pole piece to achieve point resolution as small as 0.23 nm - small enough to observe lattice structure in many crystalline materials and with a Gatan Orius bottom-mount, 14-bit, 11-megapixel CCD camera for high quality digital image acquisition and digital streaming video capture.

The whole optical system of the microscope is enclosed in vacuum, typically around 10^{-6} mBar. Air must be evacuated from the column to create a vacuum because of two reasons - first the allowance for the voltage difference between the cathode and the ground without generating arc and secondly to reduce the collision of electrons with air molecules and hence the scattering of electrons. The vacuum system for evacuating the TEM consists of several stages. Initially a low or roughing vacuum is achieved with either a rotary pump or diaphragm pump bringing the TEM to a sufficiently low pressure to allow the operation of a turbomolecular or diffusion pump which brings the TEM to its high vacuum level necessary for the operation.

The TEM sample stage is designed in such a way that it can allow insertion of a sample holder into the vacuum with minimal increase in pressure in other areas of microscope. A diagram of a TEM sample holder is shown in Fig. 2.21. The sample holder can hold a grid of standard size on which the sample is prepared. The most common TEM grid is carbon coated copper ring of diameter 3 mm and thickness 100 μm with an inner meshed area of diameter of approximately 2.5 mm onto which the sample is placed.

3

Sol-gel derived silica thin films

3.1 Introduction

Sol-gel is a very convenient and versatile process for preparing transparent optical materials at low temperature. In this process, a rigid oxide network with pores of submicrometer levels can be prepared in different forms like, bulk, fibers, thin films, powder, etc.[14–16] Sol-gel derived nanoporous thin films have many properties such as, high porosity, adjustable dielectric constant, low thermal conductivity and low dielectric constant.[17,18,32] The low dielectric constant materials are useful for device application and the porous structures are useful for preparing nanorods and nanoparticles. Therefore, it has become increasingly attractive to use these films in optical, microelectronic, and thermal applications such as antiglare and antireflective coatings, thermal insulation, and other applications.[20,147] Among all oxides, sol-gel silica film has demonstrated a more structural and thermal stable film[13] which is very useful material for the improvement of the circuit performance in semiconductor industry. Silica films are extensively used in microelectronic devices as the gate and field oxides in metal-oxide-semiconductor-field-effect transistors (MOSFETs), passivation layers, diffusion and oxidation barriers, and scratch-resistant coatings.[148]

Generally, to prepare silica film in sol-gel process water and low molecular weight alkoxide such as tetramethyl-orthosilicate (TMOS), tetraethyl-orthosilicate (TEOS) or an equivalent organometallic alkoxide are used. As the inorganic precursors hydrolyze and condense to form siloxane bonds, a sol - consists of a liquid with colloidal par-

ticles. With time, due to further polycondensation, those colloidal particles form an interconnected 3D network, called the gel. During film deposition by dip-coating or spin-coating, the polymeric or particulate inorganic precursors are concentrated on the substrate surface by a complex process involving gravitational draining with concurrent drying and continued condensation reactions.[149] The evaporation of the liquid phase during the drying of the layers of the film causes the colloidal particles to aggregate and form a network-like structure having some space, which is free from silica materials but usually filled up with low density water and/or hydrocarbon and thus can be referred as porous-like structure. Subsequent thermal treatment can remove the low density materials from the structure to form the actual porous silica film. The physical and chemical properties and also detailed microstructure of sol-gel derived silica thin film are strongly influenced by a large number of processing parameters like, precursor type, pH of the precursor solution, solvent concentration, water/silica molar ratio (R), nature of the catalyst, aging time, relative rates of condensation and evaporation, aging temperature, drying time, drying temperature, etc.[20,22,29,150,151]

Tuning these parameters not only the microstructure but also the porosity and surface area of the film can be altered. Despite a large number of work to study the influence of different solution condition on the structure and the textural properties i.e. average pore size, pore size distribution, pore shape, surface area, etc. of sol-gel silica bulk materials, only a limited number of work was carried out to inspect the influence of such parameters on the characteristics of sol-gel silica thin films. It is thus became very essential to study the dependence of different structural parameters of silica thin film on the different processing parameters.

Using X-ray reflectivity (XR) technique we have tried to understand the effect of two most important parameters, solvent concentration and aging time of solution on the microstructure of the sol-gel derived spin-coated silica thin films deposited on Si substrates. XR technique essentially provides an electron density profile (EDP) from which it is possible to estimate the thickness and average density or porosity of the film. Also we can have good idea about the structure of the film and the film-substrate interface. The latter provides the information about the attachment of the sol-gel material

with the substrate, understanding of which is very important to form continuous thick and thin films. It is quite evident from our study that minimum aging time of the solution is required to attach the gel material to form continuous film. The possible reason - anchoring through network-like structure, that form during aging (or polymerization) of the solution, is discussed.

3.2 Experimental details

Four silica precursor solutions were prepared in acidic media by varying the solvent/silica molar ratio, while keeping the water/silica molar ratio constant (R = 4). Tetraethyl orthosilicate [TEOS, $Si(OC_2H_5)_4$] was used as silica source while ethanol and hydrochloric acid (HCl) were used as the solvent and catalyst, respectively for solution preparation. After dissolving TEOS in ethanol, appropriate volume of water and HCl was added to the solution to get the final solution with molar ratio of TEOS : H_2O : C_2H_5OH = 1 : 4 : x, where x = 40, 60, 80 and 100 and the pH of all the solutions was kept at ∼1. The solutions were then magnetically stirred for 2 h and allow for aging. Films were tried to prepare by spin-coating each of the solution after different time of aging on the Si(100) substrates. However, the films deposited from the as-prepared and small time aged solutions were found to be discontinuous. The minimum aging-time required for the preparation of uniform thin film is found to be ∼18 h. Accordingly, the films prepared from the 18, 26, 45, 69 and 96 h aged solutions were used for further characterization. Such films were deposited at a spinning speed 5000 rpm for 30 s. All the solutions and the films were preserved at X-ray laboratory, where temperature and relative humidity were maintained at ∼25°C and ∼40%. The XR measurements of all the films were performed within a day after preparation in lab source.

3.3 Results and discussion

3.3.1 XR: Interface and out-of-plane microstructure

XR data of sol-gel derived silica films prepared with different ethanol/silica molar ratio is shown in Fig. 3.1. Kiessig fringes which are the signature of the total film thickness,

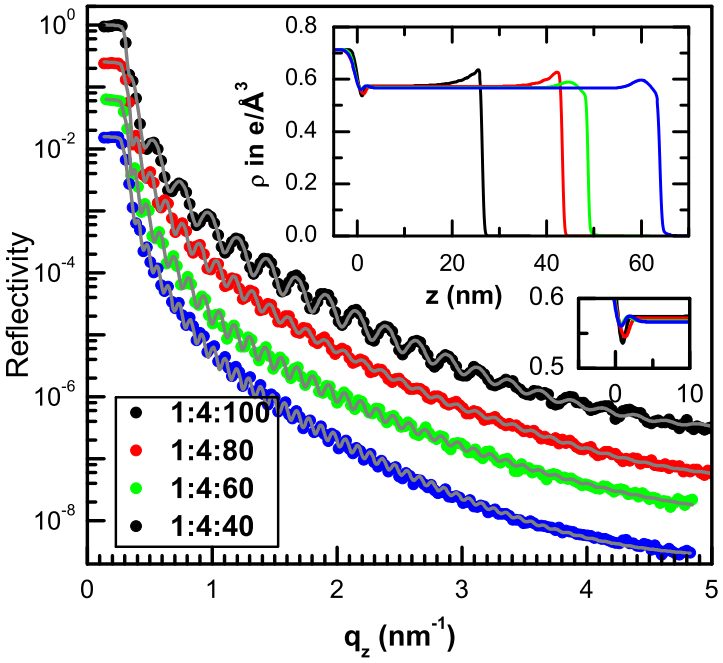

Figure 3.1: XR data (different symbols) and analyzed curves (solid line) of sol-gel derived silica films on Si(100) substrates (curves are shifted vertically for clarity) prepared with four solutions of different ethanol/silica molar ratio. Insets: corresponding EDPs, showing possible structures of the films.

evident in all the films. The appreciable change in the thickness of the films has been observed with the change in the ethanol/silica molar ratio, from which the relationship between the viscosity and the ethanol/silica molar ratio of sol-gel solution can be predicted. It is reported earlier that, the final film thickness is directly proportional to the viscosity of the sol-gel solution.[17] Here, with the increase of ethanol/silica molar ratio, the film thickness decreases, which implies that viscosity of the solution decreases with the increase of ethanol/silica molar ratio. To get details information about the thickness, EDP and structure of the films, all XR profiles have been analyzed using Parratt's formalism.[121] For the analysis, each film has been divided into a number of layers with varying electron density and roughness has been incorporated at each interface. The thickness, electron density, and roughness associated with each layer were then set as fitting parameters. Best fit XR profile along with the corresponding EDP are shown in Fig. 3.1. A close look at the nature of the EDPs suggests that relatively large electron density near top of the film with gradual exponential decrease towards substrate which

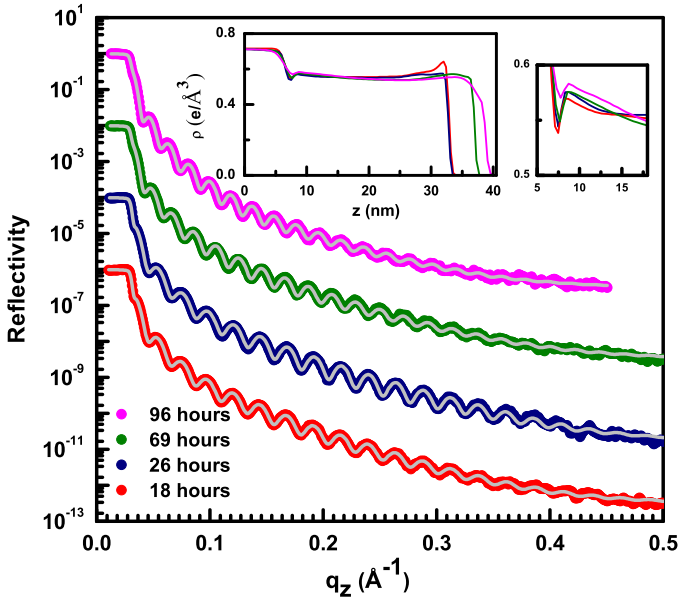

Figure 3.2: XR data (different symbols) and analyzed curves (solid line) of sol-gel derived silica films on Si(100) substrates (curves are shifted vertically for clarity) prepared from solution (TEOS : water : ethanol = 1 : 4 : 100, in molar ratio) aged for different time duration. Insets: corresponding EDPs, showing possible structures of the films.

is related to the differential evaporation of the solvent from the film during spin-coating while the layering (low density followed by high density) in EDPs above the substrate suggests that sol-gel derived silica films are probably made of woolen ball like porous nanostructure through cumulative disordered from substrate. From the EDPs it is clear that there is a dip after the substrate for all the films suggesting poor attachment of the films with the substrate, though its nature is changing with the ethanol/silica molar ratio. With the decrease of ethanol/silica molar ratio, both the width and sharpness of the dip decreases which is related to the better attachment of the film with the substrate. Moreover, as the solvent concentration increases the porosity of the film increases through evaporation from larger volume. Consequently, the average electron density which is related to the mass density of the film decreases.

XR data of sol-gel derived silica films prepared with a solution (ethanol/silica molar ratio of 100) aged for different time duration is shown in Fig. 3.2. Presence of Kiessig fringes in the XR profile of all the films indicates low thickness of the films. To get

details information, all the XR profiles have been fitted as before. The best fit XR profiles of the films prepared with a solution aged for different time duration along with the corresponding EDPs are shown in Fig. 3.2. Fitting parameters reveal that there is no appreciable amount of change in thickness and average electron density of the films prepared with the solution, aged for ∼30h. As the aging time of the solution increases (longer than ∼30h) the film thickness increases and average electron density decreases. So, it can be concluded in first approximation that after ∼30h of aging time the porosity increases with the aging time lowering the electron density and the viscosity of the solutions also increases with the increase of aging time of the solution which increases the thickness of the films due to increase of connectivity of the clusters formed by the sol particles during polycondensation reactions and evaporation of the solvent. In addition, from the nature of EDPs it is clear that with the increase of aging time of the solution, the rate of differential evaporation of solvent from the films during spin-coating decreases and evaporation of the solvent takes place uniformly from the entire film. As the aging time of the solution increases, the average electron density of the film tends to maintain a constant value throughout the entire film just above the film-substrate interface. At the film-substrate interface there is a small dip in EDP of all the films. The width and the sharpness of the dip, which is related to the poor attachment of the film with the substrate decreases as the aging time of the solution increases. This suggests that the attachment of the film with the substrate becomes stronger as the solution is aged for longer time. On the other hand, the layering (low density followed by high density) in EDPs above the substrate is present in same way for all the films suggesting that aging of the solution does not alter the woolen ball like porous nanostructure of the films.

3.3.2 Formation of woolen ball like structure

The sol-gel process involves the evolution of inorganic networks through the formation of a colloidal suspension of solid species in a liquid called sol, which is converted into a gel through polycondensation of the sol (see Fig. 3.3). A gel is a interconnected, rigid network with polymeric chains, whose average length is greater than a micrometer, and

pore width of nanometer dimensions. Generally sol-gel process can be described by the hydrolysis and condensation (water and alcohol) reactions of the metal alcoxides precursors:[15,23,152]

- Hydrolysis: Si-OR + H_2O ↔ Si-OH + ROH
- Water condensation: Si-OH + HO-Si ↔ Si-O-Si + H_2O
- Alcohol condensation: Si-OR + HO-Si ↔ Si-O-Si + ROH

The alkoxide groups (OR) are replaced with hydroxyl groups (OH) in the hydrolysis reaction. The silanol groups are subsequently involved in the condensation reactions producing siloxane bonds (Si-O-Si). When sufficient interconnected Si-O-Si bonds are formed in a region, they behave as colloidal particles or sol. With time the particles and condensed silica species link together to become a three dimensional network with pores of submicrometer dimensions, which is called gel. In practice, it is impossible that all the Si-OH bonds are transformed to Si-O-Si bonds. Depending on the detailed reaction conditions, condensation may begin before hydrolysis is complete. Theoretically, a water/silica ratio, R, of 2 is sufficient for complete hydrolysis and condensation reactions as water is formed in the condensation process, but generally the reactions do not go to completion under these conditions because of the formation of intermediate species. Due to the immiscibility of water and metal alcoxides, alcohol is used as a co-solvent in the reaction. The alcohol can also participate in the reverse reaction.

One of the most important parameters in the sol-gel process is the pH of the starting solution. The isoelectric point of silica, at which the electron mobility and the surface charge is zero, occurs at approximately pH = 2. This pH value forms the boundary between so-called acid catalysis of the polymerisation process (pH $<$ 2) and base catalysis (pH $>$ 2). Under acidic condition, the oxygen atom in Si-OH or Si-OR is protonated in a rapid first step. The electron density are shifted from the Si atom, making it more electrophilic and accessible for reaction with water (hydrolysis) or silanol (condensation). On the other hand, under basic condition it is likely that water dissociates to produce nucleophilic hydroxyl anions in a rapid first step. The hydroxyl anion then attacks the silicon atom. Acid catalysis is associated with fast hydrolysis rates, slow condensation

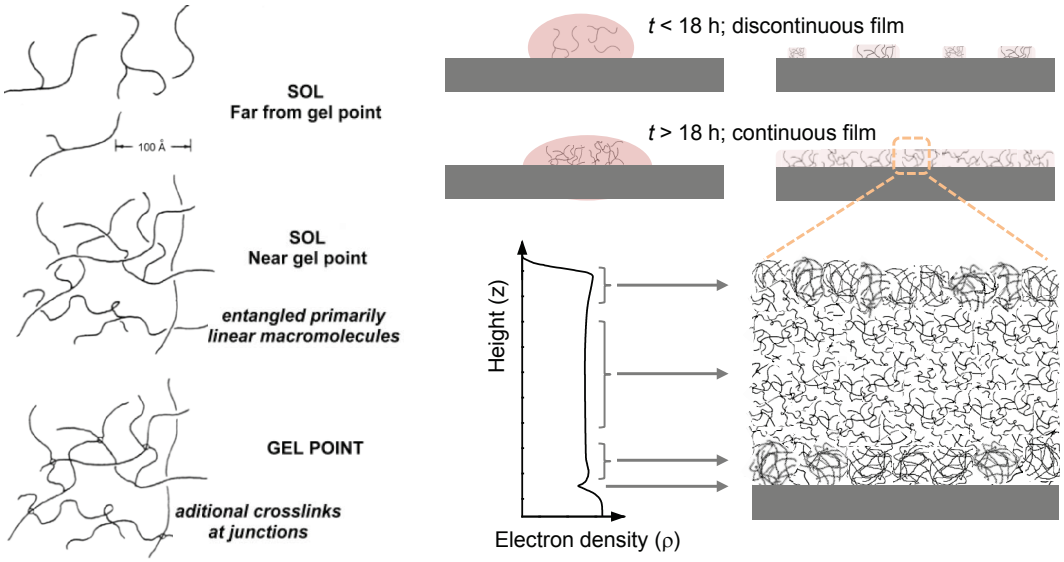

Figure 3.3: Left: Polymerization or gelation of solution due to aging. Top-right: Formation of discontinuous and continuous films by spin-coating the silica sol aged for less than and greater than ∼18 h, respectively, suggesting sufficient number of polymer-like networks in the solution is required for the attachment and getting continuous film. Bottom-right: EDP and model structure of a continuous film.

rate and relatively long gel times whereas, under basic conditions, hydrolysis is slow and condensation rates are faster, giving rise to shorter gel times. In the limit of low pH (< 2) linear chain like flexible network is formed and under conditions of pH > 2 highly branched cluster like less flexible network is formed. Moreover, the chain like flexible silica network is positively charged and highly branched cluster like network is negatively charged as it is prepared under acidic ($<$ isoelectric point) and basic ($>$ isoelectric point) condition, respectively. These are the network structures in bulk solution which can be different at an interface due to columbic interaction within the network as they are confined on an interface and also interaction of the network with the substrate.

The positively charged chain like flexible network prepared under acidic condition behaves like polyelectrolytes which are charged macromolecules, ionize in the presence of polar solvents like water. Long-range Coulomb interactions between the chain like networks and also between the network and the substrate come into play when the sol-gel silica solution is deposited on anionic Si substrates. The oppositely charged Si substrate attracts the networks which helps the silica film formation, whereas the electrostatic repulsion between the networks hinder to do so. Finally, the two opposite electrostatic

interactions counterbalance each other and the flexible chain like networks furl to form spheroidal coils i.e. woolen ball like structure to attach with the substrate during film preparation. Consequently, the attachment of the film with the substrate is found to be through a few number of network segments which is related to the layering i.e., low density (dip) followed by high density above the substrate (shown schematically in Fig. 3.3). From our experiment, it is found that sol-gel solution needs a minimum aging time (∼18 h) to form a minimum number of network through which the film can attach with the substrate.

3.3.2.1 Role of solvent/silica molar ratio

The density of the chain like silica networks in the solution increases with the decrease of solvent concentration in the solution while the silica content is fixed. As a result, during film preparation they furl to form spheroidal coils of shorter diameter to reduce the electrostatic repulsion between the neighboring networks and the number of spheroidal coils directly attached with the substrate surface increases which in turn increases the number of attachment point of the film. Thus decrease of solvent concentration in sol-gel solution induces better attachment of the film with the substrate.

3.3.2.2 Role of solution aging

During aging, solvent evaporates from the sol-gel solution making the networks less flexible and branched cluster like networks are formed by cross linking between the chain like networks. This increases the number of attachment points of the film with the substrate suggesting better attachment of the film with the substrate with the increase of aging time.

3.4 Conclusions

The structural variation of sol-gel derived silica thin films prepared with solutions of different solvent concentration and aged for different time duration was monitored using XR technique. From the analysis of the XR data it is found that with decrease of solvent/silica molar ratio and increase of aging time of the solution the viscosity of

the solutions increases which increases the thickness of the films due to increase of connectivity of the clusters formed by the sol particles during polycondensation reactions and evaporation of the solvent. Further analysis of the XR data suggests that all the films probably made of woolen ball like porous nanostructures of the silica network through cumulative disordered from substrate which evolves sequentially as the product of successive hydrolysis and condensation reactions (and reverse reactions). The poor attachment of the films with the substrate is a characteristic feature of all the films. With the decrease of solvent concentration and increase of aging time, better attachment of the film with the substrate is observed. On the other hand, the electron density of the films decreases with the increase of solvent/silica ratio and aging time of the solutions. So, it can be concluded in first approximation that the porosity increases with the solvent concentration and aging time of the solution, lowering the electron density. The variation in structure of sol-gel derived silica film depending upon different solution conditions makes it very useful from application point of view.

4

Surfactant-mediated mesostructured silica films

Part of the work of this Chapter is published in *Soft Matter*, 2012, **8**, 2956.

4.1 Introduction

Surfactant-templated mesostructured silica materials, discovered by Mobil researchers in 1992,[153] are the subject of intense research due to their potential applications as membranes, low dielectric-constant insulators (so-called low κ-materials), sensors, optoelectronic devices, etc.[4,40,46,47] In many applications, such materials often require in the form of thin films can be grown by a procedure called evaporation-induced self-assembly (EISA),[4] which involves sol-gel chemistry of inorganic precursor, self-assembly of surfactant molecules and finally evaporation of the solvent. The process begins with a homogeneous solution of surfactant, soluble silica, alcohol and water in an acid condition to minimize the siloxane condensation. The concentration of surfactant in the solution, which is kept below critical micellar concentration (cmc), changes with time due to evaporation to form aggregates (called micelles) of different shapes such as, spheres, cylinders, layers, etc. During film deposition by dip-coating or spin-coating, self-assembly i.e. micelle formation and further organization of micelles take place by evaporation of the solvent, which produces lamellar, 2D-hexagonal (p6m), 3D-hexagonal (P63/mmc), or cubic (Pm3n) mesostructures.[45,50,154,155] The structures of the micelles depend on different solution conditions like the surfactant:silica ratio, the initial silica sol after the hydrolysis, relative humidity of the environment, nature of the silicon alkoxide, temperature of the solution, etc. and in many cases can be rationalized by

considering intermolecular forces.[8,156] Even the substrate surface condition on which the films are deposited can play important role on the growth of mesostructured thin film.[56] These parameters are also very important to control the quality of the organization in films.[48,157,158] Besides, the mechanical stability of these mesostructured films is an important consideration for use in almost any application especially, for incorporation of metal nanoparticles. The mechanical stability has usually been addressed in terms of maintaining the porosity of the films. Several treatments have been developed to remove the organic templates from the mesostructures to prepare well-ordered mesoporous films which certainly influence the characteristics of the porous structure.

In this chapter, the morphological evolution of surfactant silica mesostructured films with respect to the synthesis conditions like, surfactant/silica ratio and solvent concentration along with the influence of substrate surface condition on the growth and structure of these surfactant templated mesostructured silica films of different thickness, mainly using XR and GISAXS techniques, were presented. The effect of surfactant removal process on the stability of such films involved in preparing well-ordered mesoporous films for further applications was also examined. The XR results provide information on the out-of-plane separation between the micelles in the films and the attachments of the films to the substrates. Such information allows us to predict possible structures of the films but to ascertain the prediction, structural information along both (out-of-plane and in-plane) directions, which can be obtained from GISAXS results, is very important.

4.2 Different mesostructured silica films

Surfactants exist in a wide range of ordered structures in the condensed states. Depending upon solution conditions like, surfactant concentration, pH, temperature, or electrolyte concentrations in the solution these structures can also transform from one to another. For instance, at a low concentration of surfactant in water, individual surfactant molecules form small spherical aggregates.[8,63] These spherical micelles can coalesce at higher concentration to form elongated cylindrical micelles. Different mesostructures are then formed at slightly higher concentrations. Initially, rod-like micelles aggregate

to form hexagonal close-packed mesostructure. As the concentration further increases, cubic bicontinuous mesostructure is obtained, followed by lamellar structure.[8,46,63,158]

These mesostructures have been largely used as templates to prepare a variety of well-ordered surfactant-templated silica films. During the drying process of film preparation, the growth of micellar ordered domains progressively takes place from the air-sol interface to the interior of the films. By simply changing the surfactant to silica ratio in the initial solution, three phases are observed where different micellar structures have been stabilized by the silica network formed at the time of gelation- (i) 3D-hexagonal structure with the $P6_3/mmc$ space group, constituted from a dense packing of spherical micelles, (ii) a cubic structure with the $Pm3n$ space group, constituted from ellipsoidal micelles and (iii) 2D-hexagonal structure with the $p6m$ space group, constituted from cylindrical micelles.[158]

In this study, we mainly focus our attention in preparation of different hexagonal mesostructured silica films, by changing only the surfactant/Si molar ratio of the initial solution, while keeping other parameters fixed. Cationic surfactant cetyltrimethylammonium bromide [CTAB, $C_{16}H_{33}N(CH_3)_3Br$] as structure directing agent and tetraethyl orthosilicate [TEOS, $Si(OC_2H_5)_4$] as silica source were used for preparation of precursor solution. To identify the structure of the films, samples were characterized using two complementary X-ray scattering techniques - XR and GISAXS. For further confirmation about the structure formation, TEM measurements were performed on some samples, which gives direct image of the structure.

4.2.1 Experimental details

To prepare 2D-hexagonal and 3D-hexagonal mesostructured films two precursor solutions were prepared in a two step process by changing the silica/surfactant molar ratio. In the first step, silica sol was prepared by hydrolysis and condensation of TEOS in acidic condition (pH value 1). In parallel, a second solution was prepared by dissolving different amount of CTAB in ethanol and water. In the second step, second solution was added to the first one to get the final solution of molar ratio TEOS : CTAB : C_2H_5OH : H_2O = 1 : x : 20 : 5.5, where x = 0.19 and 0.10. The CTAB/Si molar ratio 0.19

and 0.10 corresponds to formation of 2D-hexagonal and 3D-hexagonal mesostructure, respectively. The final solution was then stirred for 1 h and aged for 5 h. The diluted solution was prepared by adding excess ethanol (of amount 35 cc) to the stock solution to prepare thin films. Finally, we prepared both thick and thin films by spin cast the stock and diluted solution respectively on hydrophilic OH-terminated Si surfaces with speed 4000 rpm for 60 s. The as-prepared mesostructured CTAB-silica films were then heated at 120°C for 16 h to dry and complete siloxane condensation. All the samples were preserved at x-ray laboratory, where temperature and relative humidity were maintained at ∼25°C and ∼40%, respectively. XR measurements were performed on the as-prepared (after 15 h from preparation) samples using a lab source and GISAXS measurements of the heat treated samples (after 60 days from preparation) were done using a synchrotron source.

4.2.2 Results and discussion

4.2.2.1 XR and GISAXS: Identification of strctures

XR data of different mesostructured (for different CTAB/silica ratio) thick and thin films measured initially (after 15 h) are shown in Fig. 4.1. The absence of any Kiessig fringes in the XR curves shown in Fig. 4.1(a) indicates high thickness of the films, whereas presence of Kiessig fringes in the films as shown in Fig. 4.1(b) confirms lower thickness of the film. The presence of two pseudo Bragg peaks with varying position is evident in each curve indicating the existence of repeating layered structure of micelle and silica in the film. From the positions of the Bragg peak in each curve it is concluded that the two peaks correspond to first and second order diffraction from the same pseudo plane of the mesostructure suggesting presence of long range well-ordered structure in the film. Intensity of the Bragg peaks suggests that the better ordered structure is present in the thin film compared to that in thick film. Moreover, the Bragg peak positions are different depending upon CTAB/silica molar ratio and also on film thickness. For higher CTAB/silica molar ratio, the Bragg peaks exist in higher q_z region for both thick and thin film compared to that of lower CTAB/silica molar ratio. According to Bragg's diffraction law, the d-spacing is inversely proportion to Bragg peak position. So, it is

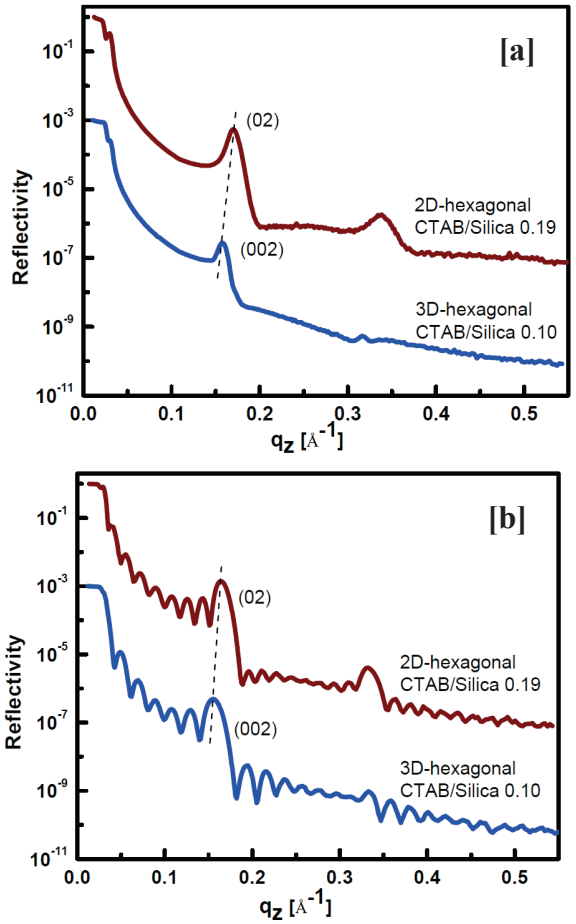

Figure 4.1: XR data of CTAB-silica 2D- and 3D-hexagonal mesostructured thick (a) and thin (b) films, for two different CTAB/silica ratio, deposited on OH-terminated Si(100) substrates, measured initially (after 15 h) (curves are shifted vertically for clarity).

clear that the d-spacing between the planes along the perpendicular direction of the substrate is larger for the films prepared with lower CTAB/silica molar ratio compared to that of higher CTAB/silica molar ratio. Values of d, obtained from the Bragg peak positions are tabulated in Table 4.1.

Fig. 4.2 represents the XR data of dried mesostructured thin films. Well resolved first and second order Bragg peaks are observed in all the curves indicating no appreciable deterioration of the ordering in the structure of such thin films with time. The values of d, obtained from the first order Bragg peak positions, are tabulated in Table 4.1. It is clear from the table that for the thin films the value of d decreases with time which is related to drying of the films in out-of-plane direction. Such decrease is less for the

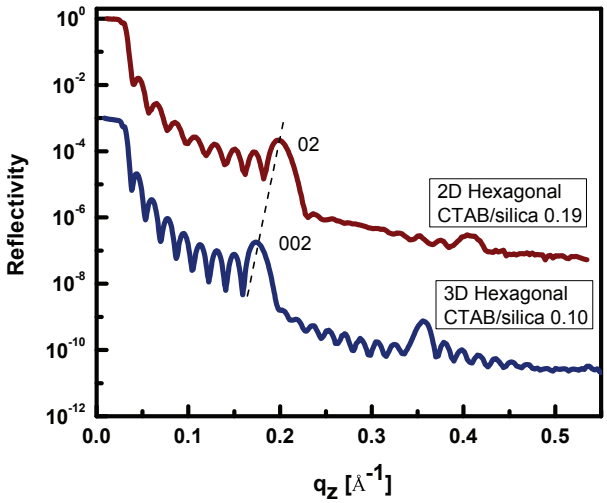

Figure 4.2: XR data of CTAB-silica mesostructured thin films deposited on OH-terminated Si(100) substrates, measured finally (after 60 days) (curves are shifted vertically for clarity).

Table 4.1: The separation (d) corresponding to the first order Bragg peaks for the films prepared with different CTAB/silica molar ratio as obtained from XR data. Subscripts i and f represent parameters corresponding to the initial and final time of measurements, respectively.

CTAB/Si molar ratio	$d_{thick,i}$ (nm)	$d_{thin,i}$ (nm)	$d_{thin,f}$ (nm)
0.19	3.68	3.81	3.16
0.10	3.98	4.04	3.63

film prepared with higher CTAB/silica molar ratio. Consequently, like the as-prepared films the out-of-plane separation between the planes of the mesostructure present in the dried films is not same. The separation is larger in the film prepared with lower CTAB/silica molar ratio compared to that of higher CTAB/silica molar ratio (shown in Table 4.1) which may be related to the shape of the micelles. Micelles with more curved geometry are expected to form in the solution of lower CTAB/silica molar ratio whereas, micelles with less curved geometry are expected to form in the solution of higher CTAB/silica molar ratio and such shape variation of the micelles induces formation of different mesostructures present in the films.[48] During drying the shape of the micelles with more curved geometry is more stable compared to that with less curved geometry and able to form stable mesostructure.

Now to identify the structures present in the films with different CTAB/silica molar

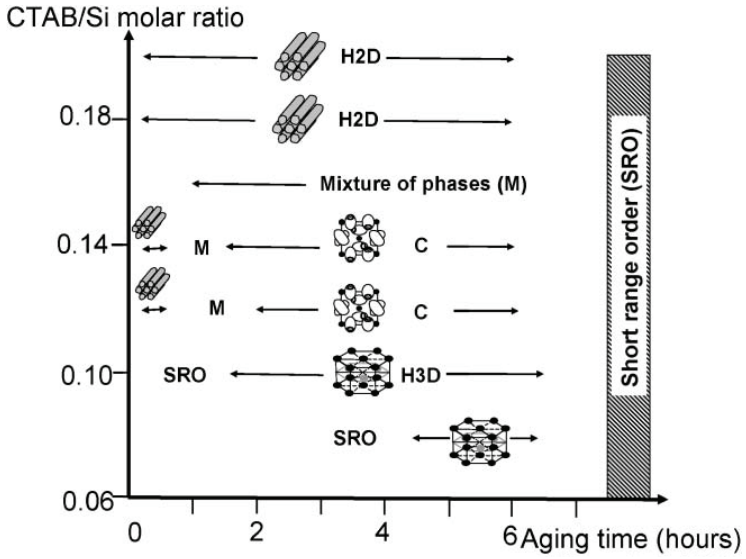

Figure 4.3: The domain of existence of the different micellar phases observed in the CTAB-silica system for different CTAB/silica ratio, adapted from literature.[158]

ratio, we have to compare the experimental results with the reported ones. Fig. 4.3 shows the different phases observed in the CTAB/silica system as a function of the aging time of the silica sol for different values of the CTAB/silica ratio. According to this phase diagram, the films prepared with CTAB/silica molar ratio 0.10 and 0.19 can be indexed to 3D-hexagonal ($P6_3/mmc$) mesostructure composed of spherical micelles and 2D-hexagonal ($p6m$) mesostructure composed of cylindrical micelles, respectively.[47,158] For 2D-hexagonal mesostructured film the Bragg peaks corresponds to first and second order diffraction from (02) plane and for 3D-hexagonal mesostructured film the Bragg peaks corresponds to first and second order diffraction from (002) plane. Both the planes are parallel to the substrate surface and no preferential orientation present along in-plane direction. Moreover, from the experiments it is clear that the 3D-hexagonal mesostructure formed with spherical micelles is more stable compared to the 2D-hexagonal structure of cylindrical micelles.

To verify the structure further we have performed TEM measurement on the thin film prepared with the diluted solution of CTAB/silica molar ratio 0.19. The film was prepared by spin-coating the solution on carbon coated copper grid. The HRTEM image of a well-ordered 2D-hexagonal structure is shown in Fig. 4.4. From this image the in-plane spacing between the micelles is found to be 2.45 nm, which is half of the

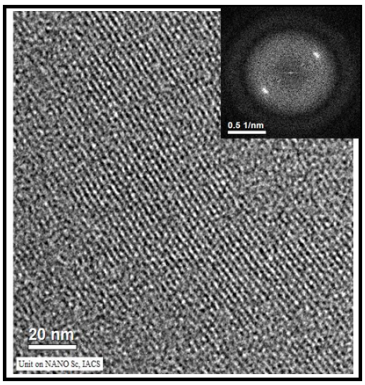

Figure 4.4: HRTEM image (in-plane view) and corresponding power pattern of well-ordered 2D-hexagonal mesostructured film prepared on grid.

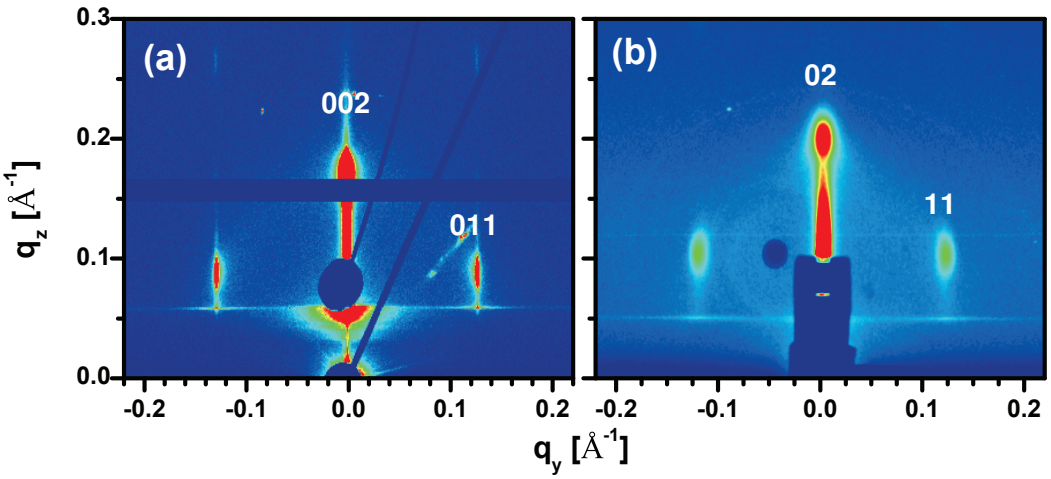

Figure 4.5: GISAXS pattern of dried CTAB-silica mesostructured thin films deposited OH-terminated Si(100) substrates, measured after 60 days of preparation (a) CTAB/ailica ratio 0.10, (b) CTAB/silica ratio 0.19.

in-plane lattice parameter b. The value is slightly less than that obtained from GISAXS measurement. This may be due to the size effect of the sample surface on which the film is prepared.

The GISAXS patterns of the dried 2D- and 3D-hexagonal thin films are shown in Fig. 4.5. One Bragg spot along q_z direction and two Bragg spot along q_y direction are present in the GISAXS pattern of both the films indicating the films have well-ordered structure. The position of the Bragg spots are different depending upon CTAB/silica ratio, similar to that of XR data. From the coordinates of the (11) and (02) peaks in the case of 2D-hexagonal mesostructure and (011) and (002) peaks in the case of

Table 4.2: In-plane (b) and out-of-plane (c) unit cell parameters of the mesostructured films on OH-terminated Si substrates. Subscripts i and f represent parameters corresponding to the initial and final time of measurements, respectively

CTAB/silica molar ratio	b (nm)	c_i (nm)	c_f (nm)
0.10	4.96	8.08	7.36
0.19	5.18	7.62	6.30

3D-hexagonal mesostructure on the GISAXS patterns it is possible to calculate the in-plane (b) and out-of-plane (c_f) structural parameters of the films, respectively (listed in Table 4.5). It is to be noted that the value of (c_f) obtained from GISAXS measurements is consistent with that of c_f ($= 2d_f$) obtained from the XR measurements.

4.2.2.2 Formation of different mesostructures

Generally, surfactant molecules are soluble in aqueous solution. Part of the initially added molecules is adsorbed onto the air-liquid interface and forms an adsorbed monolayer. Since the space for the monolayer formation is limited at the surface, the rest of the molecules remain in the solution as a free form of molecules (monomers). For most of the cases, the major driving forces for the surfactant to form well-defined aggregates are the hydrophobic attractions at the hydrocarbon-water interfaces and the hydrophilic ionic or steric repulsion between the head groups. No strong covalent bonding is involved in micelle formation. As the concentration of surfactant is increased, the monomers come close together by these interactions. Consequently, the head groups comes close together, which can be either ionic (for ionic surfactants) or hydrated (for nonionic surfactants and amphiphilic polymers) the repulsive force between the them begins to arise on the surface of the self-assembled aggregate (micelle). The transition of monomers into this self-assembled aggregate form takes place when these two opposite forces are balanced. The micelle is at equilibrium with monomers. The equilibrium structures can be determined by the thermodynamics of the self-assembly process and the inter- and intra-aggregate forces.

A simple way to describe this kind of interaction is to use a geometric packing parameter (shape factor), $g = V/a_0 l$, where V is the volume of the surfactant hydrophobic

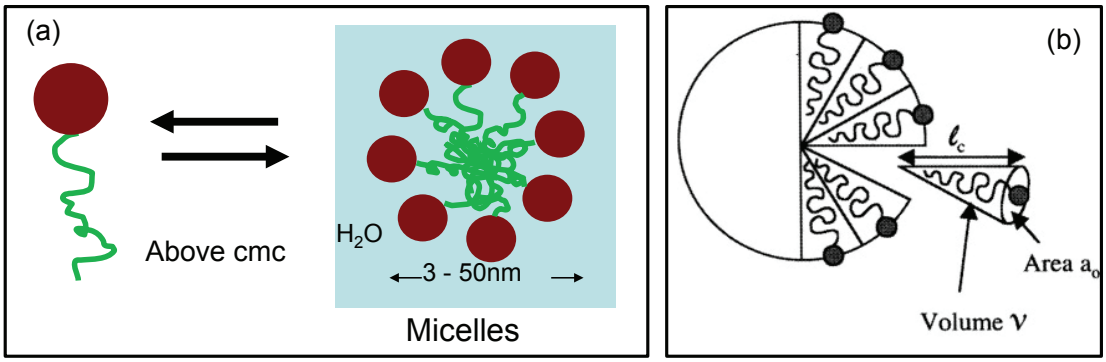

Figure 4.6: (a) Micelle formation : micellization. (b) Packing parameter g design for the structural control of mesostructured materials.

chains plus any cosolvent (organic molecules) between the chains, a_0 is the effective head-group area at the aqueous-micelle surface and l is the surfactant chain length (shown in Fig. 4.6). As a general rule, if $g < 1/3$, the micelles are spherical, if $1/3 < g < 2/3$, the micelles are cylindrical, and if $g \approx 1$, lamellae are favored. Depending upon different solution conditions, micelle of different size and shape can be formed, which act as template to prepare well-ordered mesostructured silica film. Among these condition, the initial surfactant/silica molar ratio is taken as the main critical packing parameter for tailoring the final mesostructure. As the surfactant concentration increases, the amount of water available for association with the surfactant head group decreases. Consequently, the degree of hydration of the surfactant head group decreases. The reduced hydration of the head groups leads to a decrease in the effective head group area. Based on the critical packing parameters, for fixed surfactant tail length, a reduction of the head group area increases the critical packing parameters. A larger critical packing parameter favors a less curved geometry. As a result transition from the more curved spherical micelles to less curved cylindrical micelle and finally flat lamellar phase is observed with the increase of surfactant concentration. The cylindrical micelle has almost the same diameter as the spherical micelle and has length 2-5 times its diameter.

In this study, we have used cationic surfactant CTAB which is carrying a positive charge on the surface-active portion i.e., head group of the molecule (S^+) and negative charge (X^-) on the non-surface-active portion of the surfactant for maintaining electrical neutrality. On the other hand, in the acidic route (with pH < 2) of sol-gel process

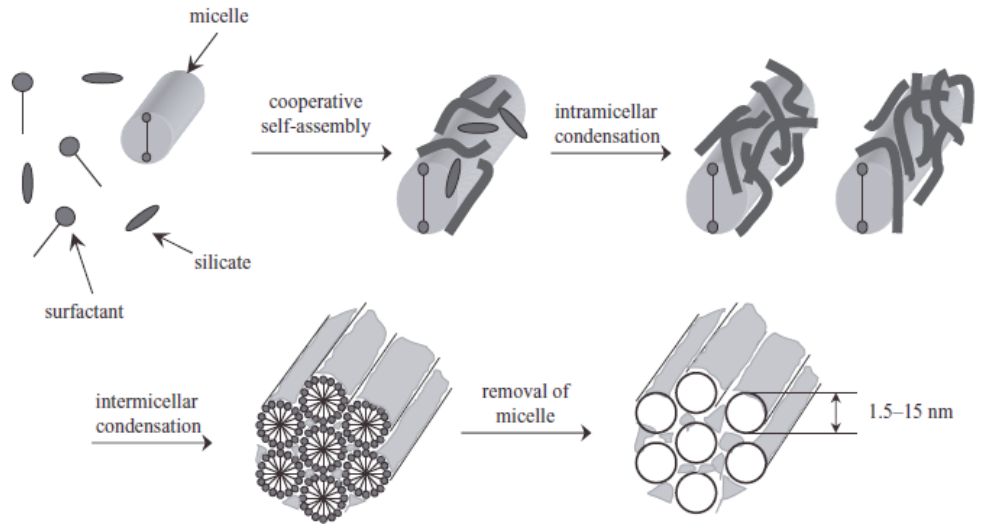

Figure 4.7: Mechanistic scheme of the formation of hexagonal mesoporous silica. Taken from literature.[8]

associated with fast hydrolysis rates and slow condensation rate, positively charged silica oligomers $\equiv SiOH_2^+$ (denoted as I^+) are formed. The addition of the silicate species in the micellar solution (spherical or cylindrical micelles) promotes the counterion binding of them on the surface of micelles through counterion mediated electrostatic forces which changes the micellar structures and can sometimes participate in the self-assembly of the surfactants. Therefore, this step is actually a cooperative self-assembly process. These silicate species will then undergo initially dominating condensation reaction on the counterion-adsorbed micellar surfaces (intramicellar condensation). For the hexagonal structure, these factors are believed to induce the transition of spherical or cylindrical micelles into long, wormlike micelles. This means that micellar growth is induced in this step of primary self-assembly. In this sense, both the surfactant and silicate can be considered to be the primary self-assembly building units. Micelles with the silicate species on their surfaces then align into the hexagonal sites through the intermicellar attraction that is mainly the condensation between the micelles. This is the secondary self-assembly process, and the surfactant-silica composites are formed in this step. The micelles are the secondary self-assembly building unit and this silica mesostructure is the secondary self-aggregate. Because of the weaker surfactant-silica interaction in the acid synthesis route, the as-prepared silica mesostructure is usually less condensed and

the structure order is thus softer which leads to rich morphology like film.

4.3 Substrate and drying effect in shape and ordering of micelles inside mesostructured films

The normal self-assembly process of the surfactant molecules at an interface can be different from that in the bulk solution, because it is perturbed by competing surfactant-surface and solvent-surface interactions, which can lead to different structure. The adsorption of surfactant molecules on solid surfaces in aqueous solutions has attracted much attention in the field of colloid and surface chemistry because of its interesting physical and chemical properties. Recently, adsorbed surfactants at different solid-liquid interfaces have been widely studied mainly using atomic force microscopy to obtain direct images of surface aggregates at the interface between solid substrates and aqueous solutions.[159–165] These studies suggest strong role of substrate surface condition, apart from concentration of the surfactant, in structure formation through different attachments. The substrate surface condition can be modified through termination of surface with OH or H group, which essentially modifies the surface free energy or polar-nonpolar (hydrophilic-hydrophobic) or electrostatic nature of the surface.[55,59,62,63,85,87,166] However, not much systematic work has been carried out to understand the role of such substrate surface condition on the initial attachment of silica coated surfactant molecules, which can not only control the initial mesostructure of the film,[54] but also the final mesostructure through subsequent drying. Moreover, understanding the role of alcohol on those structures and their control is very important, as it is known that alcohol can act as cosolvent or cosurfactant and can modify the mesostructure, accordingly.[50,51]

In order to understand those issues, mesostructured films (by selecting fixed ratio of surfactant and silica) were prepared after adding different amount of excess alcohol before spin coating on OH- and H-terminated Si substrates and were then characterized using complementary XR and GISAXS techniques. Formation of compressed 2D-hexagonal or centered rectangular ($c2mm$) mesostructure (as shown schematically in Fig. 4.8) with disorder by deviating from perfect 2D-hexagonal structure (for which

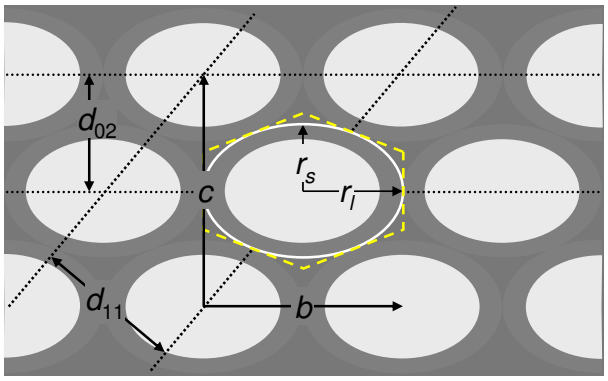

Figure 4.8: Schematic of compressed 2D-hexagonal i.e. centered rectangular ($c2mm$) mesostructure with unit cell parameters (b and c), lattice spacings (d_{02} and d_{11}), Wigner-Seitz cell (yellow dashed lines) and corresponding ellipse (white curve) with semi-major (r_l) and semi-minor (r_s) axis.

$d_{11} = d_{02}$, $r_l = r_s$ and $c/b = \sqrt{3}$), are observed. Possible role of substrate surface, excess alcohol and drying on such structural deformation, are discussed.

4.3.1 Experimental details

Silica-surfactant stock solution were prepared using CTAB as surfactant to prepare 2D-hexagonal mesostructured films on differently terminated Si surfaces. Before film preparation, different diluted solutions were prepared by adding excess ethanol (of amount ϕ = 15, 20, 30 and 35 cc) to that stock solution to study the effect of alcohol in the mesostructure formation. Films were then prepared by spin-coating the diluted solutions on the hydrophilic OH-Si substrates labeled as OH(0), OH(15), OH(20), OH(30) and OH(35) and on hydrophobic H-Si substrates labeled as H(0), H(15), H(20), H(30) and H(35). All the samples were then preserved at x-ray laboratory, where temperature and relative humidity were maintained at ∼25°C and ∼40%, respectively. XR measurements were performed on the samples as a function of time (first measurement of each sample was carried out after 15 hours from preparation) to see the effect of drying in the structure of the film and GISAXS measurements of the dried samples were done using a synchrotron source.

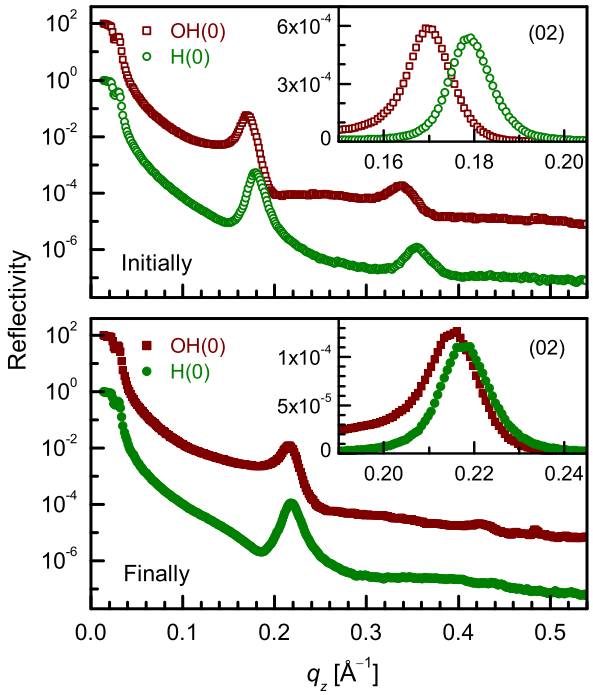

Figure 4.9: XR data of CTAB-silica mesostructured thick films on differently-terminated Si(001) substrates, measured initially (after 15 h) and finally (after 2 months) (curves are shifted vertically for clarity). Insets: magnified view of corresponding first order (02) Bragg peak to have better idea about their position and intensity.

4.3.2 Results and discussion

4.3.2.1 XR: Interface and out-of-plane structures

XR data of OH(0) and H(0) CTAB-silica films measured initially (after 15 h) and finally (after 2 months) are shown in Fig. 4.9. The presence of pseudo Bragg peak (around $q_z = 0.2$ Å^{-1}) with slightly varying position (see insets of Fig. 4.9) is evident in each curve. Also the nature of reflectivity profile (or fall of intensity), after Bragg peak, is not same. For OH(0) film, the fall is sharp followed by small dip, while for H(0) film, the fall is more gradual. The absence of any Kiessig fringes in the curves indicates that the films are quite thick, while the presence of pseudo Bragg peak indicates the existence of repeating layered structure in the film. Such repeating layers are arising from the periodic arrangement of the cylindrical micelles in polymeric silica matrix to form 2D-hexagonal structure, which corresponds to the (02) Bragg peak of equivalent rectangular unit cell (see Fig. 4.8). The second order Bragg peaks, which are present

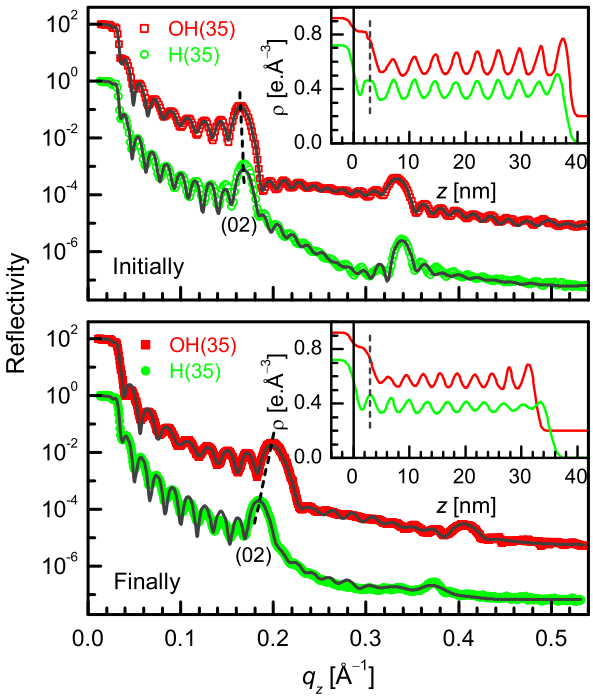

Figure 4.10: XR data (different symbols) and analyzed curves (solid line) of CTAB-silica mesostructured thin films on differently-terminated Si(001) substrates, measured initially (after 15 h) and finally (after 2 months) (curves are shifted vertically for clarity). Position and movement of first order (02) Bragg peak are indicated by dashed line. Insets: corresponding EDPs, showing possible structures of the films on different surfaces with different film-substrate layer (between solid and dashed straight lines).

in the initially-measured films, are almost absent in the finally-measured or dried films. Also, the intensity of the first Bragg peaks decreases considerably for the dried films, which indicates that the ordering in the structure of the films deteriorates with time. Values of d (i.e. d_{02}), obtained from the (02) Bragg peaks, are tabulated in Table 4.3. Decrease in the values of d with time is clearly evident, which is related to the drying. However, such decrease is different for films on differently-terminated substrates and is more for OH(0) sample, where initial value of d was large. This suggests that though 2D-hexagonal structure is formed on both terminated surfaces, the size, shape or separation of micelles is probably not same. To predict further from the XR data, extraction of EDP is necessary, which is possible for thin films, as discussed next.

XR data of OH(35) and H(35) CTAB-silica films measured initially (after 15 h) and finally (after 2 months) are shown in Fig. 4.10. Unlike thick films, Kiessig fringes are present in the curves indicating low thickness of the films. Well resolved first and second

Table 4.3: Parameters, such as the separation (d) corresponding to the first order (02) Bragg peaks and its shrinkage (Δd) with time, the total film thickness (D) and the number of repetitive layers (N) for the films on differently-terminated Si substrates as obtained from XR data. Subscripts i and f represent parameters corresponding to the initial and final time of measurements, respectively.

Sample	d_i (nm)	d_f (nm)	Δd (nm)	D_i (nm)	D_f (nm)	N
OH(0)	3.71	2.91	0.80			
H(0)	3.52	2.89	0.63			
OH(15)		3.04			55	17
H(15)		3.20			58	17
OH(20)		3.13			49	15
H(20)		3.19			55	16
OH(30)		3.13			39	11
H(30)		3.19			41	11
OH(35)	3.82	3.16	0.66	38	33	9
H(35)	3.74	3.40	0.34	38	35	9

order (02) Bragg peaks are observed in all the curves. The intensity of both the peaks decreases for the dried films. This indicates that the ordering in the structure of such thin films deteriorates with time, however, the ordering is better compared to the thick films. The values of d, obtained from the (02) Bragg peak positions, are tabulated in Table 4.3. It is clear from the table that for the thin films the value of d decreases with time and such decrease is less for the film on H-Si substrate, similar to that observed for the thick films. However, the values of d obtained for the thin films are more compared to those of the thick films and the change in the values of d, due to drying, for both the thin films is quite less compared to that for the thick films.

To get further information about the thin films, EDPs have been extracted by analyzing the XR profiles using Parratt's formalism.[121] For the analysis, a model of oscillatory electron density profile, arising from periodic repetitions of two stacked layers with roughness at each interface, is considered. One layer is made of cylindrical surfactant aggregates plus silica wall, having an averaged electron density ρ_1, a thickness t_1 and a roughness σ_1. Another layer is made of silica only, with an electron density ρ_2, a thickness t_2 and a roughness σ_2. Depending upon the substrate nature the initial attachment may be different, which is also considered in the model. Best fit XR profiles of the films on two differently-terminated substrates along with the corresponding EDPs

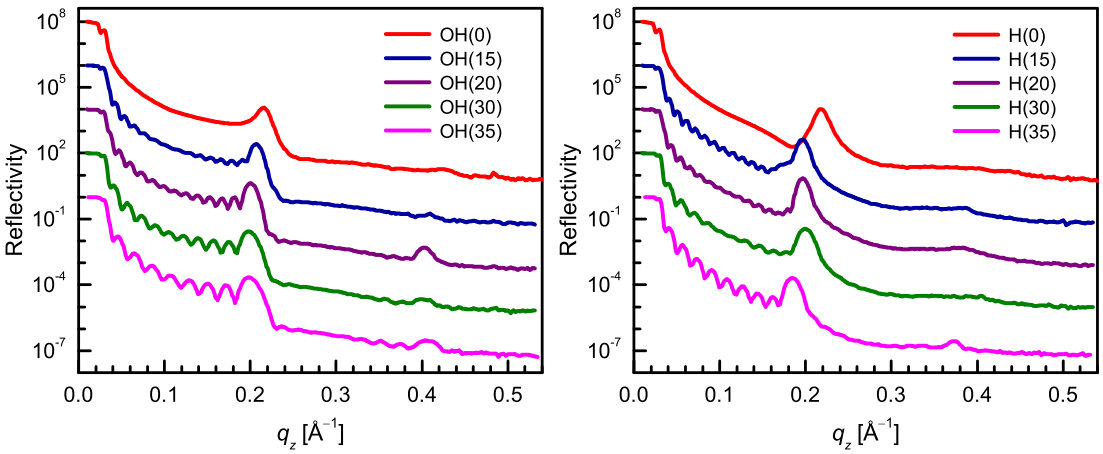

Figure 4.11: XR data of CTAB templated mesostructured dried silica films of different thickness deposited on hydrophilic OH-terminated Si substrates and hydrophobic H-terminated Si substrates. Curves are shifted vertically for clarity.

thus obtained are shown in Fig. 4.10.

The EDPs near film-substrate interface for two films are quite different. For the OH(35) film, after substrate there is an intermediate plateau region followed by a dip, while for the H(35) film a sharp dip after substrate is evident. The width of the dip is again different. The plateau and dip regions correspond to silica and micellar layers, respectively. Such silica layer is arising partially from oxidation of Si substrate after RCA treatment and partially from the coating of micelles. Absence of silica layer on H-Si substrate indicates direct attachment of micelles on it. Such attachment is via a hemicylindrical micellar layer as the small width of the dip suggests. It is necessary to mention that the different nature in the fall of intensity after the Bragg peaks on differently-terminated substrates is related to this different types of attachment.

The EDPs (Fig. 4.10) show that after initial film-substrate layer (of thickness d_{fs}), both the films consist of N number of repetitive cylindrical micellar layers, where the top silica layer has extra thickness (d_t). The repetitive layers are uniformly spaced throughout the film with average separation d. The values of N and the total film thickness ($D = d_{fs} + N \times d + d_t$) are enlisted in Table 4.3 along with the values of d. For the films measured initially, the value of d on OH-Si substrate is larger than that on H-Si substrate, which may be related to the shape of the micelles. It is expected that due to the different attachment of the film with the substrate, the spherical shape

of micelles on hydrophilic substrate may become elliptical (with large in-plane size and small out-of-plane size) on hydrophobic substrate. Furthermore, it is observed from the EDPs that the ordering of micelles on the H-Si substrate is nearly uniform, while on the OH-Si substrate, it is better towards the top. With time the separation decreases and the ordering deteriorates for both the films. The deterioration in the ordering with time is likely to be related to the stress developed due to asymmetric shrinkage of the film, namely shrinkage only allowed along z-axis but not in $x - y$ plane. The decrease in separation, which is mainly related to the drying of the silica materials, not only decreases the silica wall thickness but also the size of the micelles along out-of-plane direction, as evident from the EDPs. The decrease is however more on OH-Si substrate, suggesting definite role of the initial shape of the micelles. The asymmetric shrinkage, which tries to make the shape of the micelles elliptical (by compressing along out-of-plane direction), is likely to affects more if the initial shape is spherical rather than elliptical. The value of N is found to be same (9) for both the films. However, the value of D for both the samples, which was similar at the time of initial measurements, finally becomes different due to the different change in value of d with time.

In order to understand any systematic influence of excess alcohol on the structure of the films on both the substrates, XR curves for the dried films of different alcohol content (thus of different thickness) on hydrophilic (OH-Si) and hydrophobic (H-Si) substrates are shown in Fig. 4.11. The shift of (02) Bragg peak towards the lower q_z value with the increase of excess ethanol in the solution is observed. The value of d_f obtained from the peak position and the value of D_f obtained from the Kiessig fringes (for the films grown on OH-Si substrates, initial silica layer thickness was also included) are listed in Table 4.3, which indicate the increase in the value of d_f and the decrease in the value of D_f with the increase of excess alcohol in the solution. From the value of D_f it is possible to find out the value of N, which is also listed in Table 4.3. The addition of alcohol in the solution just before deposition is to dilute the solution, hence to decrease the viscosity, which is observed in the value of D_f, but not in the value of d_f. The increase in the value of d_f, which is related to the micelle size and the silica coating thickness, apparently suggest that the increase in the micelle size is large compared to

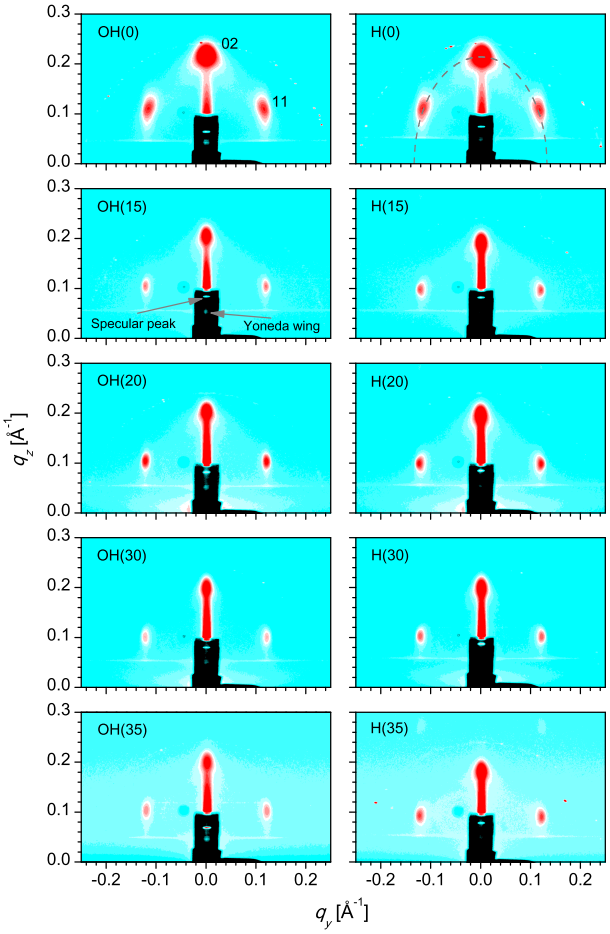

Figure 4.12: GISAXS pattern of the CTAB templated dried silica films of different thickness on hydrophilic and hydrophobic Si substrates, showing (11) and (02) peaks of the compressed 2D-hexagonal structure, semi-elliptical ring (dashed line) used for the estimation of the ratio (r_l/r_s) and also the specular peak and Yoneda wing (indicated by arrows).

the decrease of the silica wall thickness.

4.3.2.2 GISAXS: In-plane and out-of-plane structures

So far, we have discussed XR results, which essentially provide the information about the out-of-plane separation between the micelles in the films and the attachments of the films with the substrates. Such information allow us to predict possible structures of the films and the role of different parameters, such as hydrophobic-hydrophilic nature of substrate, cosolvent-cosurfactant nature of alcohol or stress effect of drying, on those structures formation. However to ascertain the prediction, structural information along

both (out-of-plane and in-plane) directions, which can be obtained from GISAXS results, is very important and will be discussed now. GISAXS patterns of the dried CTAB-silica mesostructured films of different thickness on differently-terminated Si substrates are shown in Fig. 4.12. (02) and (11) Bragg spots, signatures of compressed 2D-hexagonal structure, are evident in all the patterns. In-plane (b) and out-of-plane (c_f) structural parameters for all the dried films, extracted from GISAXS spots are listed in Table 5.2 and plotted as a function of excess alcohol (ϕ) in Fig. 4.13(a). It is necessary to mention that the value of c_f obtained from the GISAXS measurements is consistent with that of c_f ($= 2d_f$) obtained from the XR measurements (Table 4.3). Specular peak and Yoneda wing are also observed in the GISAXS patterns, which correspond to the incident angle (α) and the critical angle (α_c), respectively.

Fig. 4.13(a) shows that the value of b decreases (however small), unlike c_f, with excess-alcohol content. This is in contradiction with the prediction that the increase in the size of micelles is larger than the decrease in the silica coating thickness. To understand the actual situation, we have investigated the ratio of semi-major and semi-minor axis (r_l/r_s) of the ellipse,[167] as defined in Fig. 4.8. The values of $(r_l/r_s)_f$, estimated from $\sqrt{3}/(c_f/b)$, are listed in Table 5.2. These values agree well with the values estimated from the semi-elliptical ring[167] as indicated in Fig. 4.12. The variation of $(r_l/r_s)_f$ with ϕ is shown in 4.13(b). Also to understand the effect of drying, the value of c_i ($= 2d_i$) for the thick and thin films, obtained from the initial XR measurements and the corresponding ratio $(r_l/r_s)_i$, considering b remains unchanged with time, are listed in Table 5.2 and also included in Fig. 4.13. It is clear from the Fig. 4.13 that the shape of the silica layer coated micelles in the films, changes with the addition of excess alcohol in the solution, even in the initial stages of measurements. However, the change ($\sim$0.1) is small compared to the dried films ($>$0.2). With time the change in the value of r_l/r_s for the films on OH-Si is more compared to that on H-Si. Correspondingly, the value of $(r_l/r_s)_i$ for the films on H-Si is slightly larger than that on OH-Si, while the value of $(r_l/r_s)_f$ is reverse.

The variation of different parameters, plotted in Fig. 4.13, can be expressed quantitatively using standard exponential dependence. First consider the size ($2R$) of circular

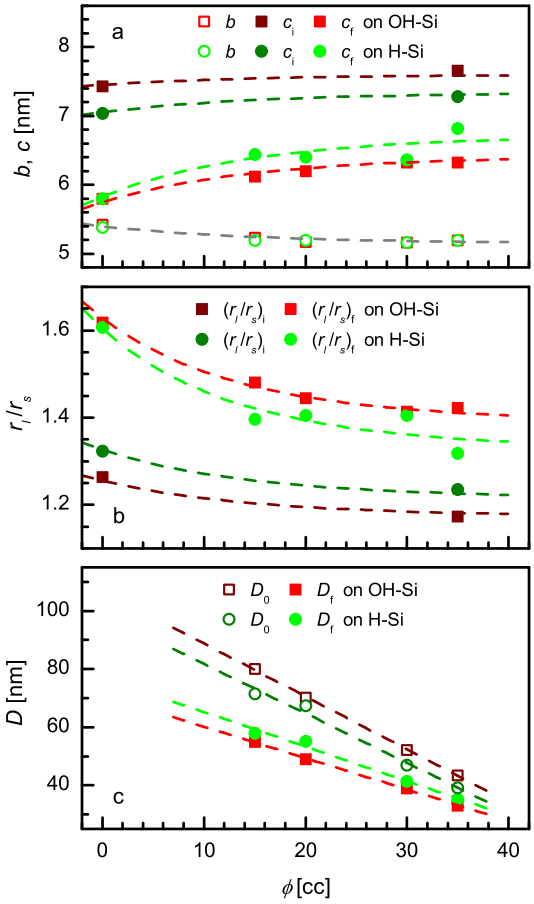

Figure 4.13: Influence of excess alcohol (ϕ) on (a) the in-plane (b) and out-of-plane (c) unit cell parameters of the compressed 2D-hexagonal structure, (b) the ratio of semi-major and semi-minor axis (r_l/r_s) of corresponding ellipse and (c) the film thickness (D) for the different films on hydrophilic and hydrophobic Si substrates. Dashed lines through the data points in (a) and (b) are the analyzed curves and in (c) are the straight lines. Subscripts 0, i and f represent parameters corresponding to the as-prepared time and to the initial and final time of measurements, respectively.

micelles. Presuming no drastic change in the shape of the micelles in our experimental alcohol domain, the variation of $2R$ with excess alcohol (ϕ) can be written as:

$$2R(\phi) = 2R_0 + 2\Delta R(1 - e^{-\phi/\Phi}) \tag{4.1}$$

where $2R_0$ is the size corresponding to the stock solution, $2\Delta R$ is related to the change in size and Φ is related to the critical amount of the excess alcohol. Second consider the in-plane separation (b), the value of which is a sum of the size of a micelle ($2R$) and the thickness of silica wall. Due to the attachment of the film with the substrate,

there should not be any in-plane movement of materials in the film with time (t), hence b should be independent of t. The variation or decrease of b with excess alcohol, as observed experimentally, can be expressed as:

$$b(\phi) = b_0 - \Delta b(1 - e^{-\phi/\Phi}) \tag{4.2}$$

where b_0 is the in-plane separation corresponding to the stock solution, Δb is the change in separation, which is related to the combined change in the size and in the silica wall thickness. Third consider the ratio r_l/r_s (or $2r_l/2r_s$). The in-plane size, $2r_l$ is nothing but b, which is a function of ϕ, but independent of both t and nature of substrate, while the out-of-plane size, $2r_s$ depends on all three parameters (ϕ, t and nature of substrate). The decrease of $2r_s$, initially on hydrophobic substrate, is due to the change in the shape of micelles from circular to elliptical, while with time, is essentially due to contraction of silica materials, which also changes the shape of the micelles. The contraction of silica materials depends on the silica wall thickness and initial shape of micelles. Considering all these aspects, variation of r_l/r_s can be expressed as:

$$\frac{r_s}{r_l}(\phi, t) = \frac{fb(\phi) - \Delta[b(\phi) - 2R(\phi)/f^2](1 - e^{-t/\tau})}{b(\phi)} = f - \Delta[1 - \frac{1}{f^2}\frac{2R(\phi)}{b(\phi)}](1 - e^{-t/\tau}) \tag{4.3}$$

where $f \leq 1$ is a substrate nature dependent term, which takes into account the different initial shape of the micelles in the film. For circular shape, $f = 1$; while for in-plane elongated elliptical shape, $f < 1$. Second term essentially takes into account the change with time, where Δ and τ are the critical decay constant and time, respectively. Such change is also related to the silica wall thickness and the initial shape of the micelles, which have been taken care by the square bracket term. Note that for $t = 0$, $r_l/r_s = 1/f$ and for $f = 1$, $r_l/r_s = 1$.

Eqs. 5.1 to 4.3 have been used to simulate the variation of b, c and r_l/r_s. For the simulation, a set of values for different parameters (other than that for f) is used for all the samples. First the variation of b has been fitted using Eq. 4.2. The fitted profile is shown in Fig. 4.13 and the value of the parameters (Φ, b_0 and Δb) are listed in Table 5.3. Next, the variation of r_l/r_s and c [$= \sqrt{3}b/(r_l/r_s)$] have been simulated using Eqs. 5.1 to

Table 4.4: In-plane (b) and out-of-plane (c) unit cell parameters of the compressed 2D-hexagonal structure, the ratio of semi-major and semi-minor axis (r_l/r_s) corresponding to the equivalent ellipse and estimated as-prepared film thickness (D_0) for the different films on differently-terminated Si substrates. Subscripts i and f represent parameters corresponding to the initial and final time of measurements, respectively.

Sample	b (nm)	c_i (nm)	c_f (nm)	$(r_l/r_s)_i$	$(r_l/r_s)_f$	D_0 (nm)
OH(0)	5.42	7.42	5.80	1.26	1.62	
H(0)	5.38	7.04	5.80	1.32	1.61	
OH(15)	5.23		6.12		1.48	80
H(15)	5.19		6.44		1.40	72
OH(20)	5.17		6.20		1.44	70
H(20)	5.19		6.40		1.40	68
OH(30)	5.16		6.32		1.41	52
H(30)	5.16		6.36		1.41	47
OH(35)	5.19	7.64	6.30	1.18	1.43	43
H(35)	5.19	7.28	6.82	1.24	1.32	39

4.3. For the simulation we have fixed the value of $2R_0 \approx 3$ nm, which we obtained by preparing film containing micelles only (see supplementary information). The analyzed profiles are shown in Fig. 4.13 and the parameters obtained from the analysis are listed in Table 5.3, which are useful to predict the evolution of the structure of the film, as discussed in the next section. Furthermore, the film thickness at the time of preparation (i.e. $t \approx 0$) can also be estimated considering $D_0 = f(d_{fs} + d_t + \sqrt{3}bN/2)$ and using $d_{fs} + d_t \approx 3$ nm (as obtained for the thin film) and the values of N, b and f, as listed in Tables 4.3 to 5.3. The value of D_0 thus obtained are listed in Table 5.2. Such value of D_0 along with the value of D_f are plotted in Fig. 4.13(c), which show almost linear decrease with excess alcohol. However, the value of D and its change with excess alcohol for the films on OH-Si are initially (i.e. $t \approx 0$) large, but finally become small compared to those for the films on H-Si.

4.3.2.3 Formation mechanism

The evolution of the structures on OH-Si and H-Si substrates are shown schematically in Fig. 4.14. Before elaboration of such model structures, let us first discuss the general formation mechanism of the silica-surfactant mesostructure. Above cmc, surfactants aggregate and form micelles. It is formed by a process of force balance in which no

strong covalent bonding is involved.[6,8,164] The initial shape of such micelle is mostly spherical, which can transformed to other shape depending upon the solution conditions. It is known that in acid synthesis route, the mesostrcutured silica is formed by weak electrostatic interaction between cationic surfactants head group (S^+) and positively charged silica oligomer (I^+), mediated by counterion (X^-).[43,168] Hence the initial micelle formation is fast but the silica condensation is slow. The surfactants first adsorb the counterions to form the S^+X^- micelles, while in acidic solution, the hydrolysis and protonation of TEOS first generates the positively charged silica species as $\equiv SiOH_2^+$ (denoted as I^+). In the mixed solution, the condensation reaction of I^+ occurs on the counterion-adsorbed micelle surface ($S^+X^-I^+$) and once enough silica condensation occur to form long polysilicate chains, then those chains act as bridges between micelles (having hydrophobic tail part inside and hydrophilic head group outside) to form the mesostructure. The final shape of micelles and their arrangement in the film, however, depend on the solution conditions. Concentration of CTAB, CTAB:TEOS ratio, pH, temperature, etc. chosen for the present experiment are such that they lead to the formation of cylindrical micelles in 2D-hexagonal structure.[4,40,45,46]

It is known that OH-Si substrate is hydrophilic, while H-Si substrate is hydrophobic in nature, which can be easily verified from the wetting or dewetting properties of the water with the surface through naked eyes, apart from contact angle measurements.[60] Such different nature of the substrates will exert different forces on the silica coated aggregates. Accordingly, the initial attachment of the film on hydrophilic substrate is via silica coated cylindrical structured micelles, while that on the hydrophobic substrate is via hemicylindrical structured micelles. As the OH-Si surface is hydrophilic and anionic in nature, they can attract the positively charged silica coated micelles ($S^+X^-I^+$) by electrostatic interaction to lower the free energy of the system. As a result a silica buffer layer is found on the Si substrates and above it there are cylindrical micelles (as shown schematically in Fig. 4.14). On the other hand, H-Si substrate, due to its hydrophobic nature, can not form hydrogen bonds with water, rather try to cover-up with the surfactant hydrophobic tails to reduce the water exposer on it and also the free energy of the system. Best possible reduction for such silica coated micellar system

Table 4.5: Different parameters used for the simulation of the size, shape and separation of the micelles in the films on the two differently-terminated Si substrates.

Substrate	Φ (cc)	b_0 (nm)	Δb (nm)	$2R_0$ (nm)	$\Delta 2R$ (nm)	τ (hr)	Δ	f
OH-Si	15	5.4	0.25	3.0	0.45	20	0.85	1.0
H-Si	15	5.4	0.25	3.0	0.45	20	0.85	0.9

is however possible by formation of hemicylindrical micelles with reduced curvature on the substrate (as shown schematically in Fig. 4.14).

The cylindrical micelles are then stacked above the first micellar layer, the shape which is strongly influenced by the curvature of the micelles in the first layer. For the as-prepared films, the near circular micelles on OH-Si substrate with $r_l/r_s \approx 1$ become elliptical on H-Si substrate with $r_l/r_s \approx 1.1$ (as shown schematically in Fig. 4.14 for $t \approx 0$ and $\phi = 0$). Next, when excess alcohol is added to the solution just before deposition, it acts as both cosolvent and cosurfactant. As cosolvent it dilutes the solution, which decreases the repetition number and the silica coating layer thickness, while as cosurfactant it resides on the outer boundaries of the micelles, which increases the effective head group area of the surfactant molecule[51] and hence the size of the micelles (from $\sim$ 3.0 to 3.45 nm, obtained from $2R_0$ and $2\Delta R$ values). Combination of the coating layer thickness and the micelles size, decreases the overall separation, which showed up in the value of b (from $\sim$ 5.40 to 5.15 nm, obtained from b_0 and Δb_0 values) only, but not in r_l/r_s (as shown schematically in Fig. 4.14 for $t \approx 0$ and $\phi = 35$ cc). Further with the addition of excess alcohol the silica coating thickness decreases from $\sim$ 2.4 to 1.7 nm, which is showed up on the hydrophilic substrate. On the hydrophobic substrate, the micelles become elongated (with size $2R/f^2$) along in-plane direction. So, on such substrate, the in-plane size of the micelles changes from $\sim$ 3.7 to 4.25 nm with addition of excess alcohol and corresponding in-plane silica wall thickness changes from $\sim$ 1.7 to 0.9 nm.

The structures of the films, that we discussed so far, are formed just after deposition, that is due to the fast evaporation of solvent while spin coating. Such structures further modified with time, as presented in Fig. 4.14 for initial and final stages of measurements and can be visualized as follows. With time, the thickness of the coated silica layer

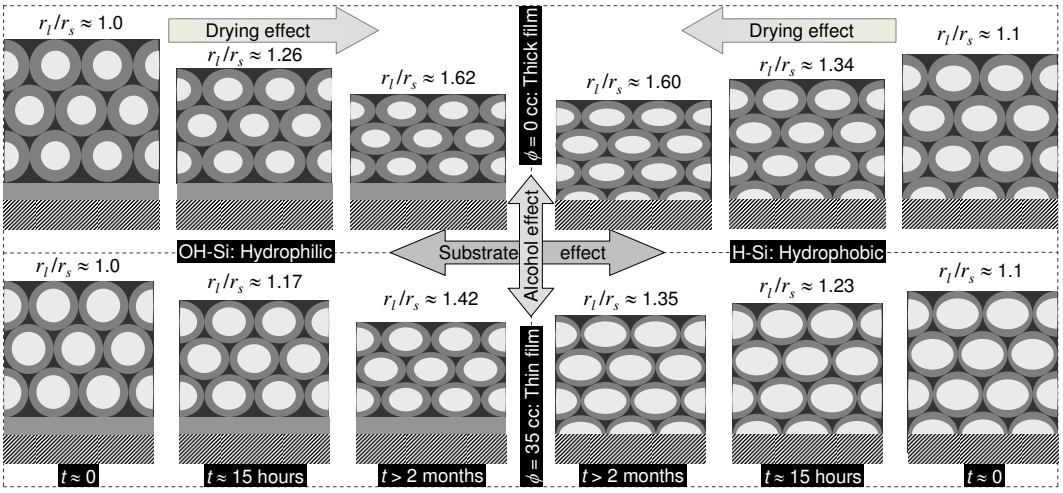

Figure 4.14: Model cross-sectional views of the CTAB-silica mesostructures just after deposition ($t \approx 0$) and in the initial ($t \approx 15$ hours) and final ($t > 2$ months) stages of measurements for the thick ($\phi = 0$) and thin ($\phi = 35$ cc) films on OH-Si and H-Si substrates as predicted from XR and GISAXS results, showing the effects of substrate, alcohol and time (drying) on the r_l/r_s value, on the attachment of the films on the substrates, and on the size, separation and shape of the micelles in the films.

decreases due to drying effect. Such decrease is only allowed in the out-of-plane direction but not in the in-plane direction (due to the attachment of the film with the substrate). This also decreases the size of the micelles and the separation between them along out-of-plane direction, which in turn changes the shape of the micelles by squeezing them along the out-of-plane direction and the value of r_l/r_s, respectively. It is necessary to mention that the value of silica coated layer thickness $(b - 2R)$ which seems to be quite large ($\sim$ 2.4 to 1.7 nm) initially becomes quite reasonable ($\sim$ 1.5 to 1.2 nm) with time due to drying, as obtained from out-of-plane information. The change in the r_l/r_s value seems to depends on the initial in-plane silica wall thickness. If such thickness is large (which is for the films prepared with $\phi = 0$) then the change is large, while if thickness is small (which is for the films prepared with ϕ = 35 cc) then the change is also small. Considering the different initial shape of the micelles on the OH-Si and H-Si substrates, largest initial silica wall thickness ($\sim$ 2.4 nm) is estimated for the thick film on OH-Si substrate and corresponding change in the value of r_l/r_s is maximum ($\sim$ 0.62; change from 1 to 1.62), while smallest in-plane silica wall thickness ($\sim$ 0.9 nm) is estimated for the thin film on H-Si substrate and corresponding change in the value of r_l/r_s is

minimum ($\sim$ 0.25; change from 1.1 to 1.35). However, in terms of the shape of the micelles, the maximum and minimum deviations from the circular shape are observed for the thick film on H-Si substrate and the thin film on OH-Si substrate, respectively. Also with time, due to the asymmetric shrinkage of the silica wall and hence also of the micelles, the stress is developed in the film, which deteriorates the ordering in the film. For the thick film, both the number of repetitive micelles layers (N) and the silica wall thickness are big, hence the stress is large.

4.4 Surfactant templated mesoporous silica films

Technical advances in various fields, such as adsorption, separation, catalysis, drug delivery, sensors, photonics, and nanodevices, require the development of ordered porous materials with controllable structures and systematic tailoring pore architecture. The well-ordered mesoporous silica films can only be obtained after the elimination of the surfactants from as-synthesized mesostructure silica films by different removal methods which certainly influence the characteristics of mesoporous materials.[169–172] The porous structure as well as catalytic, adsorbed, conductive and magnetic properties of the mesostructured films can readily be tailored by tuning different solution condition like, surfactant/silica molar ratio which changes the shape of the micelle and overall mesostructure, the pH of the solution, addition of counterion, the length of the surfactant molecules used as templating agent etc.

The most common method to remove templates is calcination owing to the easy operation and complete elimination of the surfactants. The drawbacks of calcination are the unrecovery of surfactants and the sacrifice of surface hydroxyl groups. Moreover, it is unsuitable for thermally unstable and air-sensitive materials, such as sulfides and organic frameworks. Solvent extraction is a mild and efficient method to remove surfactants and get porosities without distinct effects on frameworks. Ethanol or THF can be used as an organic extracting agent. A small amount of hydrochloric acid is added in the extracting agent to improve the cross-linkage of frameworks and to minimize the effects on mesostructures.[40]

In this section, our aim is to prepare stabilized mesoporous silica films through the

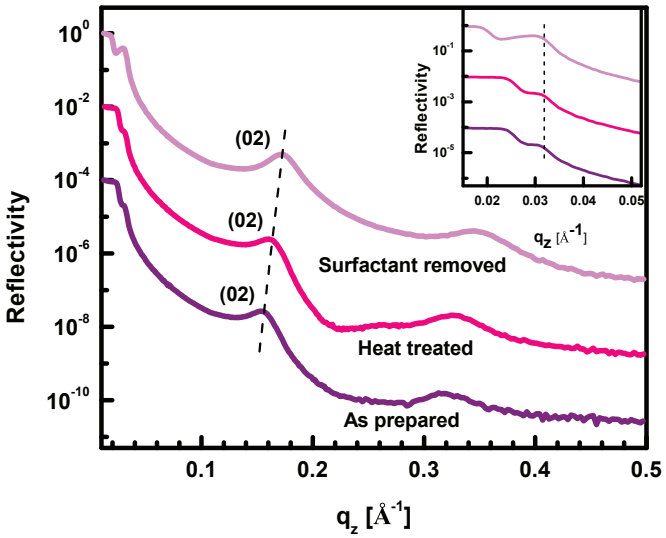

Figure 4.15: GISAXS pattern of CTAB-silica mesoporous thick film deposited on OH-terminated Si substrate, showing(02) Bragg peak of 2D-hexagonal ($p6m$ space group) structure.

template removal by solvent extraction method from mesostructured silica films. The films were then characterized using two X-ray scattering techniques - XR and GISAXS to know the complete information about the porosity and stability of the structure of the samples.

4.4.1 Experimental details

The as-prepared 2D- and 3D-hexagonal mesostructured CTAB-silica films were first heated at 120°C for 16 h to dry and complete siloxane condensation. Then solvent extraction was performed to remove the surfactant from the films where the films were thoroughly rinsed with a solution containing ethanol and hydrochloric acid (with a molar ratio of 1 : 0.007) for 3 h at 60°C to prepare stable mesoporous silica films. The extracted samples were then washed with ethanol and dried in air. XR measurements were performed on the samples 15 h using lab source and GISAXS measurements of the dried samples (after 60 days from preparation) were done using a synchrotron source.

Table 4.6: The separation (d) corresponding to the first order Bragg peaks for the 2D-hexagonal thick and 3D-hexagonal thin film as obtained from XR data. Subscripts a, h and s represent parameters of the film as-prepared and after heat treatment and surfactant removal, respectively.

Film	d_a (nm)	d_h (nm)	d_s (nm)	$q_{c,a}$ (Å^{-1})	$q_{c,h}$ (Å^{-1})	$q_{c,s}$ (Å^{-1})
2D-hexagonal thick	4.03	3.83	3.63	0.023	0.024	0.019
3D-hexagonal thin	4.00	3.88	3.49			

4.4.2 Results and discussion

4.4.2.1 XR and GISAXS: In-plane and out-of-plane structures

Fig. 4.15 represents XR data of 2D-hexagonal CTAB-silica mesostructured thick film measured initially (after 15 h) and after successive treatments. The first and second order pseudo Bragg peaks correspond to the (02) plane of compressed 2D-hexagonal structure with slightly varying position is evident in each curve confirming that the films was not delaminated during the successive treatment processes. With the application of each treatment, the peak position is shifted in higher q_z region i.e., there is decrease of out-of-plane separation between the planes due to shrinkage of silica walls. The d-spacing of the film estimated from the peak position of XR data after successive treatments is tabulated in Table 4.6.

The most important feature to be observed in these XR data is the position of critical angle which is directly related to the average electron density. There are two critical angles q_c present in all the XR profile, the critical angle at lower q_z position corresponds to the average electron density of the film of whereas the critical angle at higher q_z position ($\sim$0.0316 Å^{-1}) is that of the silicon substrate. As these films have an electron density lower than the substrate density, they actually act as quasi-waveguides. A close look at the critical angles (shown in the inset of Fig. 4.15) indicates that successive treatment processes have strong effect on the average electron density of the film. Table states that after the heat treatment the critical angle is shifted towards higher q_z region, whereas after the rinsing process there is a significant shift of that towards lower q_z region, meanwhile the substrate q_c remains the same (as expected) during both the treatments. In other words, the average electron density of the film increases after the

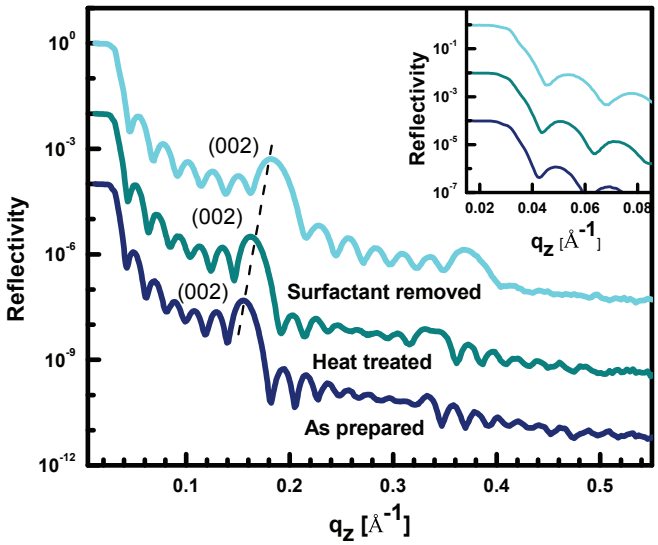

Figure 4.16: GISAXS pattern of CTAB-silica mesoporous thin film deposited on OH-terminated Si substrate, showing (002) Bragg peak of 3D-hexagonal ($P6_3/mmc$ space group) structure.

heat treatment process whereas decreases after the rinsing process.

It is now well known that thin film is necessary for the detailed analysis of the XR data, which can provide further information about the structure. Also it is known that the thin film having 2D-hexagonal mesostructure is less stable compared to 3D-hexagonal mesostructure. So, for further XR measurements, we have used 3D-hexagonal CTAB-silica mesostructured thin films, which were subjected to different treatment processes. The reflectivity patterns of the film after different treatments, shown in Fig. 4.16, exhibit classical well-defined Kiessig fringes typical of uniform films of finite thickness. This suggests that the essential structure is not modified by treatment processes. Like the 2D-hexagonal thick film, the Bragg peak position is shifted towards higher q_z region suggesting decrease in out-of plane separation due to drying and the removal of surfactant. The decrease of d value estimated from peak position is less for the 2D-hexagonal thick film compared to 3D-hexagonal thin film, estimated in Table 4.6. The critical angle corresponds to the average electron density of the thin film is also altered after each treatment process similar to thick film, but change is not so prominent in this case compared to that of thick film.

Fig. 4.17 shows the GISAXS pattern of the 3D hexagonal thin film, heat treated and

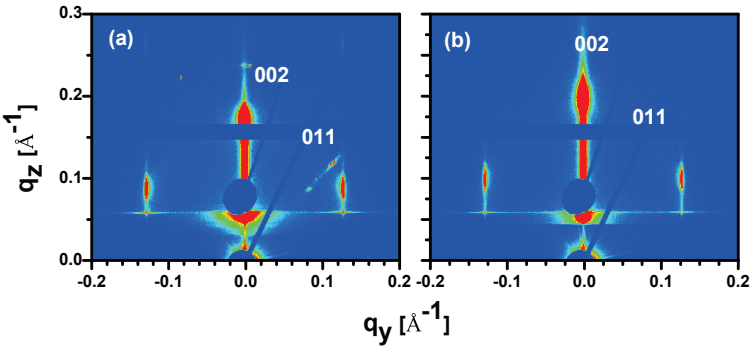

Figure 4.17: GISAXS pattern of CTAB-silica thin films deposited on OH-terminated Si substrate, showing (002) Bragg peak of 3D-hexagonal structure. (a) Heat treated mesostructured film, (b) Surfactant removed mesoporous film.

then surfactant removed. The patterns exhibit the characteristic spots of the compressed 3D hexagonal symmetry and shows this symmetry is well preserved after the heat treatment and solvent extraction process. The in-plane (b) and out-of-plane (c_f) structural parameters for the films, calculated from GISAXS spots are listed in Table 4.7. The value of r_l/r_s states that the shape of the pores becomes less spherical as the structure gone through different treatments though the overall structure remains same.

4.4.2.2 Removal of surfactant

Solvent extraction is a mild and efficient method to remove surfactants from the mesostructured silica films and get porosity without distinct effects on silica framework. Generally, ethanol or THF can be used as an organic extracting agent. It is well known that in acid synthesis route, the mesostrcutured silica is formed by weak electrostatic interaction between cationic surfactants head group (S^+) and positively charged silica oligomer (I^+), mediated by counterion (X^-).[43,168] Theoretically, the surfactants can be completely removed by the ethanol solution without an exchangeable cation needed. However, this was argued to be impossible because there is always a small amount of the cationic surfactants which remain strongly and directly bound to the silica framework of the films. So, the ion exchange i.e., extraction with acidic ethanol solution is necessary for complete removal of the surfactant template from acid synthesized mesostructured silica film. For this purpose, a small amount of hydrochloric acid is added in the ethanol

Table 4.7: In-plane (b) and out-of-plane (c) unit cell parameters of the structures, the ratio of semi-major and semi-minor axis (r_l/r_s) corresponding to the equivalent ellipse for the thin films on OH-terminated Si substrates.

Sample	b (nm)	c (nm)	(r_l/r_s)
Heat treated	4.94	7.36	1.16
Surfactant removed	4.94	6.29	1.36

solution during solvent extraction process which also helps to improve the cross-linkage of the frameworks and to minimize the effects on mesostructures.

Moreover, compared with calcination, solvent extraction process can get silicate materials with larger pore sizes. Much more surface hydroxyl groups can also be kept, enhancing the hydrophilic property and modifying the reactive ability of pore channels. However, the application of extraction is limited by the fact that surfactants cannot be completely (100%).

4.5 Conclusions

Structural evolution of evaporation-induced self-assembled CTAB-silica mesostructured films with respect to CTAB/Si molar ratio were monitored using XR and GISAXS techniques. Depending on the CTAB/Si ratio two different hexagonal structures were obtained from two micellar phases stabilized by the percolation of silica clusters resulting from the rapid evaporation of solvents: (i) at low CTAB/Si molar ratio (0.10), the 3D-hexagonal structure with the $P6_3/mmc$ space group, formed by dense packing of spherical micelles and (ii) at high CTAB/Si (0.19) molar ratio, the 2D-hexagonal structure with the $p6m$ space group, made up of cylindrical micelles. For both the structures, the films are textured with the densest micellar planes parallel to the film-substrate interfaces.

Secondly, structural evolution of evaporation-induced self-assembled 2D-hexagonal CTAB-silica mesostructured films on differently-treated Si substrates were investigated using XR and GISAXS techniques. Centered rectangular ($c2mm$ space group) structure is observed in dried films on both the hydrophilic (OH-Si) and hydrophobic (H-Si) substrates showing clear deviation from perfect 2D-hexagonal ($p6m$) structure. Such

deviation is directly related to the change in shape and ordering of the micelles with or without silica coating layer inside the film. The cylindrical shaped micelles, which are initially circular on hydrophilic OH-terminated Si substrate to form perfect 2D-hexagonal structure, become elliptical (extended along in-plane) on hydrophobic H-terminated Si substrate to form slightly compressed 2D-hexagonal structure due to different attachment of the film with the substrate. With time the silica materials try to squeeze due to drying, which can be expressed exponentially with critical drying time $\sim$ 1 day. However, squeezing is not allowed along in-plane direction due to the attachment of the film on the substrate. Such asymmetric squeezing compressed the structure and also developed stress. The latter deteriorates the ordering of the film. The compression depends on the silica wall thickness; more the thickness, more is the compression. The silica wall thickness again depends on the amount of excess alcohol. More we add the excess alcohol, less is the film thickness and the silica coating layer thickness, hence the compression and stress, which are clearly observed in the structure of the film. Excess alcohol not only act as cosolvent as mentioned before, but also act as cosurfactant. According to the latter, the size of the micelles increases exponentially with critical amount of excess alcohol as $\sim$ 15 cc. Analysis of the XR data measured in different time interval and the GISAXS data measured for the dried film suggest that during deposition, cylindrical shaped micelles are circular on OH-Si to from perfect 2D-hexagonal structure (with $r_l/r_s \approx 1$), while elliptical on H-Si to from compressed 2D-hexagonal structure (with $r_l/r_s \approx 1.1$). Such difference in shape is related to different attachment of the film with the substrate, namely silica on hydrophilic OH-Si substrate and hemicylindrical micelles on hydrophobic H-Si substrate. For the dried films, the maximum and minimum deformed structures (i.e. $r_l/r_s \approx 1.62$ and 1.35) are observed for the thick film on OH-Si and for the thin film on H-Si, respectively. However, considering the shape of the micelles, the maximum and minimum deformed shapes are predicted for the thick film on H-Si and for the thin film on OH-Si, respectively. Combining initial shape and the effect of compression with time, which are related to the nature of substrate and the amount of excess alcohol, respectively, final structures of the dried films along with the shape of the micelles are formed, which are of immense importance for their proper use

as template and other applications.

For using such mesostructured silica films as template for further application solvent extraction method has been adapted to remove the surfactant template from the silica framework. The overall structure of the film remains same though the shape of the pores becomes less spherical as a result of successive treatments. The shape of the micelle is more stable in the case of 2D-hexagonal thick film compared to that of 3D-hexagonal thin film.

5

Nature of a Cl-terminated Si surface and its time evolution estimated from deposited mesostructured silica film

The work of this Chapter is published in *Soft Matter*, 2013,**9**, 9799 and *J. Phys. Chem. C*, 2014, **118**, 11350.

5.1 Introduction

Silicon is perhaps the most widely investigated semiconductor material due to its various uses in device fabrication. Among different investigations, one of the thrust areas is tuning the nature of Si surface to control the growth and stability of different interesting nanostructures on it.[55,56,58–61,164,173–175] Tuning the nature of the surface can be done through the termination or passivation of the Si dangling bonds with selective atoms or groups like, -OH, -H, -Cl etc. and this process is extremely important for their applications in a wide range of fields, including nanotechnology, microelectronics, optoelectronics, biomedical and biological sensors.[176,177] Passivation essentially prevents contamination and surface defect states, thus controlling the electronic properties of the surface or interface.[177] It also modifies the surface free energy, the polar-nonpolar (hydrophilic-hydrophobic) or electrostatic nature, the surface defect states and the reactivity of the surface.[55–64]

Among different passivated surfaces, Cl-terminated Si surface, which has good Si-Cl bond stability is drawing tremendous attention due to its higher reactivity compared to the H-terminated Si surface for the functionalization reactions.[81,82] Such Cl-terminated

Si surface can facilitate the growth of materials with a high dielectric constant, the attachment of self-assembled monolayers, or the production of simple organic layers for application in biotechnology.[82,84] In particular, alkyl Grignards react readily with a chlorinated Si surface to create an alkyl-terminated Si surface. The efficient assembly of organic molecules on Si using the S-N linkage was achieved by reacting amines with a Cl-terminated Si surface.[83] Recently such Cl-Si surface can be prepared from the H-Si surfaces using different methods in ambient conditions, which is much more applicable to industrial purposes. Among them, the wet-chemical process is one of the best and easiest methods to maintain a contamination-free Si substrate.[88,90,178]

Despite a large number of works on the Cl-Si surface, only a limited number of works has been carried out to determine the hydrophobic/hydrophilic nature of the surface,[85–87] which again provides contradictory or incomplete information about the nature of the surface, at least on the microscopic level. For example, the macroscopic contact angle measurement for the Cl-Si surface was found to be small compared to that of the hydrophobic H-Si surface.[85] This along with ultrafast electron crystallography experiments on the adsorbed water molecules suggests that the Cl-Si surface is hydrophilic in nature.[85] On the other hand, a theoretical calculation on the adsorption of water on the Cl-Si surface based on a full first-principles approach suggests that the surface is hydrophobic in nature.[86,87] It is thus became essential to use other experimental techniques/schemes to determine the hydrophobic/hydrophilic nature of the Cl-Si surface. Understanding the initial nature of a surface, although essential, but not sufficient for the proper utilization of that surface to any specific purpose. Understanding stability/instability of that surface is also very important, as it can influence the initial growth of nanostructure on it and its evolution with time. However, not much work has been carried out to understand the stability/instability information of the Cl-Si surface at ambient conditions.

It is known that the structure of the monolayer or multilayer film of metal-organic or organic-inorganic (having both hydrophobic and hydrophilic parts) on the pretreated Si surface strongly depends on the nature of the Si surface.[56,59] The preferential adsorption of materials can provide information on the adhesion and the hydrophilic/hydrophobic

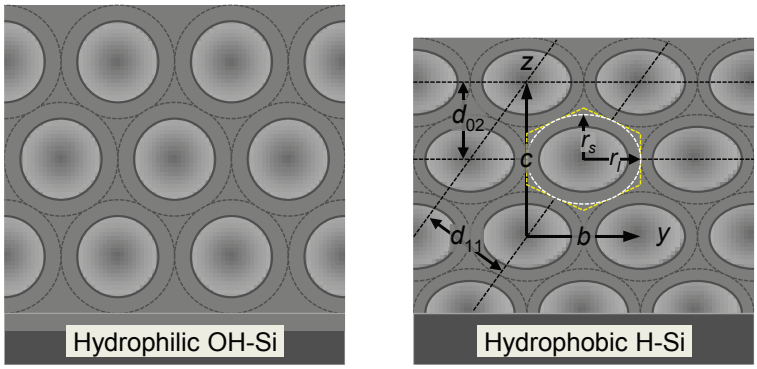

Figure 5.1: Schematics of 2D-hexagonal mesostructured films on hydrodrophilic and hydrophobic Si substrates and an equivalent centered rectangular ($c2mm$) structure with unit cell parameters (b and c), lattice spacings (d_{02} and d_{11}), the Wigner-Seitz cell (yellow dashed lines) and corresponding ellipse (white curve) with semi-major (r_l) and semi-minor (r_s) axis.

nature of a surface apart from conventional contact angle (CA) or water adhesion measurements.[133,179,180] For example, the adsorption of the metal-organic film deposited by LB technique on a hydrophilic OH-terminated Si surface proceeds via hydrophilic metal head groups, while adsorption on a hydrophobic H-terminated Si surface proceeds via hydrophobic organic tail groups.[59] Similarly, for the CTAB-silica (organic-inorganic) mesostructured film, hydrophilic silica molecules are adsorbed on the OH-Si surface to form a silica layer (gray color), while the hydrophobic tail parts of the CTAB molecules are adsorbed on the H-Si surface to form hemicircular micelles (light color),[56] as presented schematically in Fig. 5.1. Accordingly, the near circular micelles on the former became less circular (or more elliptical) on the latter (light color). and suggests that the hydrophobic/hydropholic nature of a solid surface, on the microscopic level, can be evident from the structural information of the deposited CTAB-silica mesostructured film.

In this chapter, we have used this scheme (adsorption and shape effects of silica micelles) to systematically investigate two topics: (1) hydrophilic/hydrophobic nature of a Cl-terminated Si surface and (2) time-evolution of such Cl-terminated Si surface at ambient conditions. Two complementary techniques X-ray reflectivity (XR) and grazing incidence small angle X-ray scattering (GISAXS) were used to study the structure of the CTAB-silica mesostructure film deposited on time-evolved Cl-terminated Si surface.

Special attention had paid to get information about the film-surface interface.

5.2 Nature of a Cl-terminated Si surface: hydrophilic or hydrophobic?

According to definition, a surface is hydrophilic if it tends to adsorb water or be wetted by water, whereas a surface is hydrophobic if it tends not to adsorb water or be wetted by water. A Si surface can be hydrophilic or hydrophobic depending on the surface condition. It has been reported that a hydrophilic surface is characterized by OH groups and a hydrophobic surface is covered with SiH, or SiF groups. Thus, a hydrogen-terminated surface is hydrophobic whereas an oxide- or hydroxide covered surface, which tends to be terminated by OH, is, in general, hydrophilic. [59,62,63] Moreover, Br-terminated Si substrate shows intermediate behavior indicative of coexisting hydrophilic and hydrophobic nature of this terminated surface.[58,59]

There are different ways to understand the hydrophilic/hydrophobic nature of a surface. A recent review article proposed different measures and classifications of the hydrophilic/hydrophobic nature of solid surfaces based on different parameters such as the contact angle, the water adhesion tension, the work of spreading or the energy of hydration.[180] All these parameters are essentially related with the surface free energy, the interfacial energy, surface roughness, surface texture etc. Contact angle measurements provide information on the wetting, while direct adhesion measurements using a centrifugal adhesion balance provide information on the affinity.[133,179,181] The information on the adhesion can also be available from the frictional force microscopy. These measurements gives macroscopic description of the substrate and sometimes a macroscopic description and a microscopic one can lead to a different assignment of the hydrophobic/hydrophilic character of a given substrate; in fact, a measured small contact angle does not necessarily imply strong water-surface interactions and could be compatible with a molecular-level hydrophobic description. [87]

In this study, CTAB-silica 2D-hexagonal mesostructured thin films[40,45,158] were deposited on the Cl-Si surface and also on the OH-Si and H-Si surfaces to investigate

the hydrophilic/hydrophobic nature of Cl-terminated Si surface in the molecular or microscopic level. The chlorination of the Si surface through a wet-chemical process was verified using an X-ray photoelectron spectroscopy (XPS) technique. The hydrophilic nature of the Cl-Si surface, on the macroscopic level, was confirmed by conventional contact angle (CA) measurement, while the complete structures of the films were obtained by complementary XR and GISAXS techniques, which clearly suggest that the Cl-Si surface is hydrophilic in nature, even an the microscopic level. A possible reason behind the weakly hydrophilic nature of the Cl-Si surface is discussed.

5.2.1 Experimental details

XPS measurements of Cl-Si(100) and Cl-Si(111) samples were performed to determine the chemical nature of the Cl-terminated Si surfaces. The samples were transferred to the UHV chamber just after preparation. CA measurements of the Cl-Si(100) and Cl-Si(111) samples were carried out to investigate the hydrophilic or hydrophobic nature of the samples. The CA measurements of the OH-Si and H-Si samples were also carried out for comparison.

To prepare 2D-hexagonal mesostructured films, silica-surfactant solution was prepared in two step synthesis process using CTAB as surfactant. A diluted solution was then prepared by adding excess ethanol (of amount 35 cc) to that stock solution to prepare thin films using a spin-coater. Films were prepared on the Cl-Si substrates and also on the OH-Si and H-Si substrates, which were labelled as CTAB-SiO/ClSi, CTAB-SiO/OHSi and CTAB-SiO/HSi, respectively. Before characterization, samples were preserved at X-ray laboratory, where temperature and relative humidity were maintained at $\sim$25°C and $\sim$40%, respectively. The XR measurements of the CTAB-SiO/Cl-Si, CTAB-SiO/OH-Si and CTAB-SiO/H-Si samples were performed within a day and up to 30 days after preparation (dried films) using a lab source. On the other hand, GISAXS measurements of the dried samples (after 30 days) were performed in MiNaXS beam line (P03) at the third generation synchrotron source PETRA III of Deutsches Elektronen-Synchrotron (DESY), Germany.

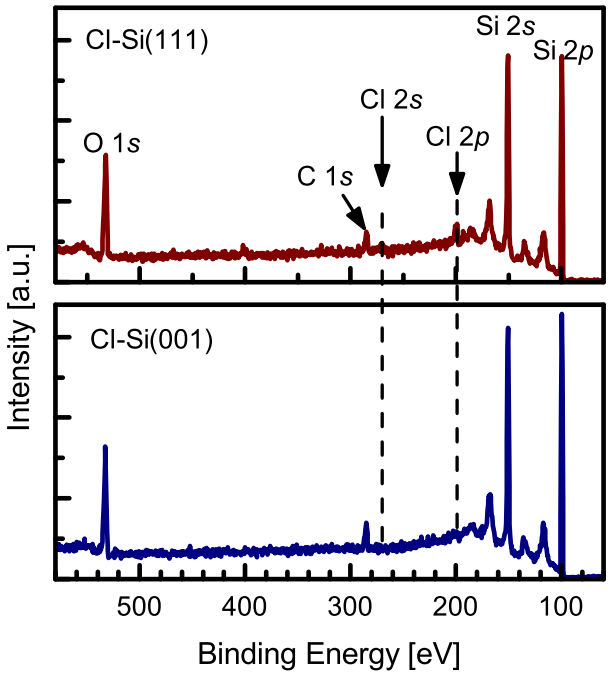

Figure 5.2: Survey x-ray photoelectron spectra for the Cl-Si(111) and Cl-Si(100) samples. Peaks are labeled with the corresponding binding energies.

5.2.2 Results and discussion

5.2.2.1 XPS: Chemical nature of surface

XPS survey scans for the Cl-Si(111) and Cl-Si(100) samples are shown in Fig. 5.2. Two pronounced peaks are observed near 99.5 and 150.5 eV for the Si 2*s* and Si 2*p* binding energies, respectively, while the observed peaks at the successive intervals of 17.5 eV on the higher binding energy side of the two principal peaks are due to the plasmon loss features, characteristic of crystalline silicon samples.[84] Two peaks near 285.5 and 532 eV are also observed in both the scans, which correspond to the C 1*s* and O 1*s* binding energies, respectively. In addition, two small peaks near 199 and 270 eV are observed for the Cl-Si(111) sample, which are almost absent for the Cl-Si(100) sample. These two peaks correspond to the Cl 2*p* and Cl 2*s* binding energies, respectively. The presence of these two peaks for the Cl-Si(111) sample indicates the formation of Cl-terminated Si(111) surface, while for the Cl-Si(100) sample very poor intensity of the two peaks suggests very small coverage of Cl on Si(100) surface.

Three high resolution spectra for the Cl-Si(111) sample near Si 2*p*, Cl 2*p* and Cl 2*s*

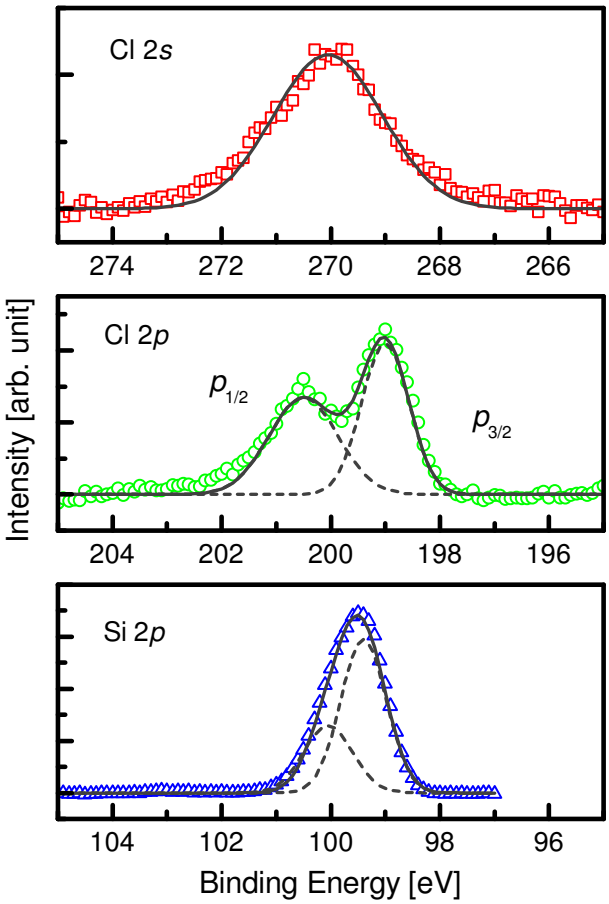

Figure 5.3: XP spectra of the Cl 2s, Cl 2p and Si 2p binding energy regions of the Cl-Si(111) sample.

binding energies are shown in Fig. 5.3. The peaks of the Si 2p spectrum can be reproduced well by considering the $2p_{3/2}$ and $2p_{1/2}$ peaks, with a separation of 0.6 eV and an area ratio of 2, in agreement with the reported values.[178] Similarly, the peaks of the Cl 2p spectrum can be reproduced well, considering the two spin-orbit split peaks ($2p_{3/2}$ and $2p_{1/2}$ with separation of about 1.5 eV). The presence of the 2s, $2p_{3/2}$ and $2p_{1/2}$ peaks of Cl in the Cl-Si(111) sample confirm the chlorination of the Si(111) surface. No significant peak for the silicon oxide layer is observed, indicating negligible oxidation of this surface. This Cl-Si(111) substrate is henceforth referred to as the Cl-Si sample.

5.2.2.2 CA: Hydrophilic/hydrophobic nature of surface

The hydrophilic/hydrophobic nature of the differently-terminated Si surfaces, in the macroscopic level, can be easily estimated from the CA measurements. The as-placed

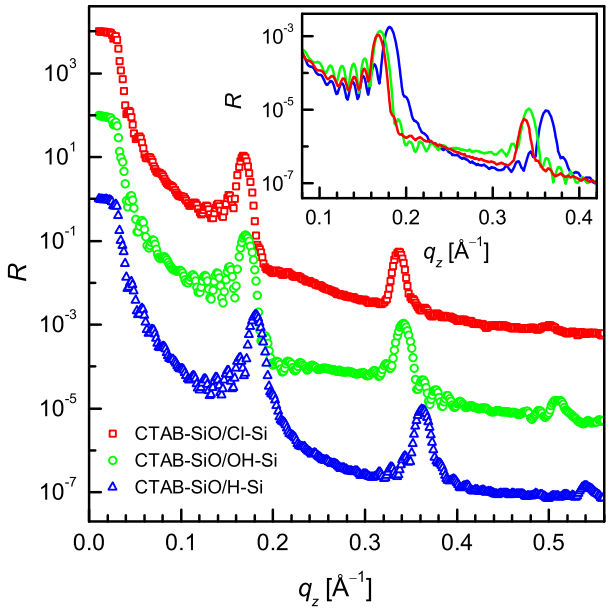

Figure 5.4: XR data of CTAB-silica mesostructured thin films on differently-terminated Si substrates, measured initially (curves are shifted vertically for clarity). Inset: selected portion of the same data (without any shifting) to have better idea about the nature of variation, before and after the first Bragg peak, for the three samples.

CA value for the Cl-Si surface is found to be about $27 \pm 5°$, while those for the OH-Si and H-Si surfaces are found to be about $15 \pm 3°$ and $64 \pm 4°$, respectively. The footprint of water on the Cl-Si surface is found to be about 4-5 mm. The CA can provide the information about the adhesion, surface energy, or hydrophilicity/hyhrophobility (which is of our interest).[180] The values of the CA for the OH-Si and H-Si surfaces correspond to the hydrophilic and hydrophobic nature of the surfaces, as expected.[182] The value of CA for the Cl-Si surface is very small compared to that of the H-Si surface, but large compared to that of the OH-Si surface. This suggests that the Cl-Si surface is weakly hydrophilic in nature.

5.2.2.3 XR: Hydrophilic/hydrophobic nature from interface and out-of-plane structures of deposited film

The XR data of the CTAB-SiO/Cl-Si, CTAB-SiO/OH-Si and CTAB-SiO/H-Si samples collected after preparation are shown in Fig. 5.4. Two strong and one very weak pseudo Bragg peaks are visible in all the curves, which correspond to the first, second and

third orders of the (02) Bragg peak for the 2D-hexagonal mesostructure, suggesting the formation of well ordered 2D-hexagonal structure. The nature of the XR profile before and after the first Bragg peak for the CTAB-SiO/Cl-Si sample is found to be intermediate to those of the CTAB-SiO/OH-Si and CTAB-SiO/H-Si samples. This is clearly visible from the curves shown in the inset of Fig. 5.4. The peak-height of the first Bragg peak compared to the preceding dip is minimal for the CTAB-SiO/OH-Si sample and maximal for the CTAB-SiO/H-Si sample, while for the CTAB-SiO/Cl-Si sample it is in between. The fall after the first Bragg peak and before the second Bragg peak is sharp and then almost flat for the CTAB-SiO/OH-Si sample and very gradual for the CTAB-SiO/H-Si sample, while for the CTAB-SiO/Cl-Si sample it is again in between, but more like the CTAB-SiO/OH-Si sample. Kiessig fringes, which are the measure of the total film thickness, are very clearly observed for all the XR profiles before first Bragg peak. The values of d (i.e. d_{02}) obtained from the (02) Bragg peak positions for the three films are tabulated in Table 5.1 with an accuracy better than $\pm$ 0.02 nm. The value of d for the film on Cl-Si is large compared to that on H-Si and even slightly larger than that on OH-Si.

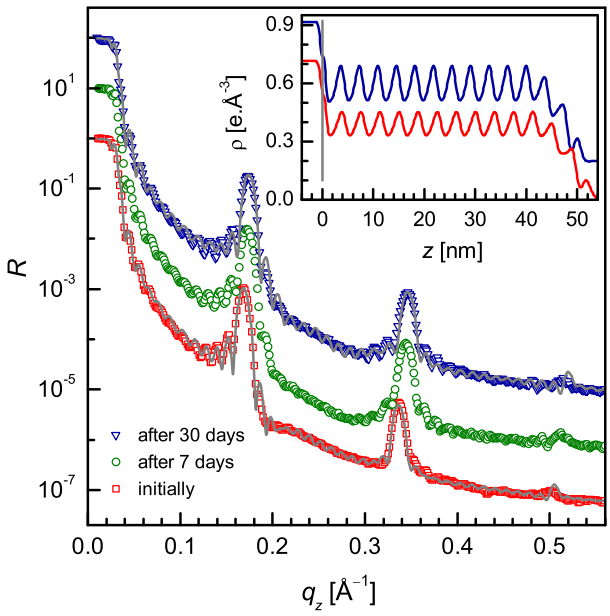

Figure 5.5: XR data (different symbols) and analyzed curves (solid line) of the CTAB-silica mesostructured thin film on the Cl-Si substrate measured at different time intervals (curves are shifted vertically for clarity). Inset: corresponding EDPs measured initially (within a day) and finally (after 30 days).

Table 5.1: Parameters such as the separation (d) corresponding to the (02) Bragg peaks, the total film thickness (D) and the number of repetitive layers (N) for the three samples as obtained from the initially measured XR data.

Sample	d (nm)	D (nm)	N
CTAB-SiO/Cl-Si	3.74	52.5	14
CTAB-SiO/OH-Si	3.70	48.4	13
CTAB-SiO/H-Si	3.47	54.0	15

XR data of the CTAB-SiO/Cl-Si sample collected in different time interval are shown in Fig. 5.5. There is no decrease in the Bragg peak intensity with time indicating no deterioration in the ordering of the film with drying. The Bragg peak positions however change with time but the change is mostly within 7 days. This is same for the change in the nature of the curve before and after the first Bragg peak. The change in the peak positions with time is associated with the decrease in the d value with drying, while the change in the nature of the curve with time may be due to the change in the d value and/or due to the change in the interface. To have a better idea about the structure of the film, especially about the film-substrate interface, the XR data have been analyzed using Parratt's formalism.[121] For the analysis, a model of oscillatory electron density profile (EDP), arising from periodic repetitions of two stacked layers is considered as before.[56] One layer is made of cylindrical surfactant aggregates plus a silica wall and another layer is made of silica only, having different averaged electron density, thickness and roughness. In addition, special attention is paid to the initial layer through which the film is attached to the substrate, as it decides the nature of the substrate surface.

Based on this model, the different natures of the XR profiles (before and after the first Bragg peak) that we observed experimentally in Fig. 5.4 have been simulated (not shown here) considering only the different interfacial natures. Namely adsorption of the film onto the H-Si substrate proceeds through hemicylindical micelles and that onto the OH-Si substrate proceeds through the silica coated cylindrical micelles with the freshly prepared oxide surface, while that onto the Cl-Si substrate is directly through siica coated cylindical micelles. The best fit XR profiles for the CTAB-SiO/Cl-Si sample measured initially and finally are shown in Fig. 5.5 along with the corresponding EDPs in the inset. For the CTAB-SiO/Cl-Si sample measured initially, there is a dip after

Table 5.2: In-plane (b) and out-of-plane (c) unit cell parameters of the compressed 2D-hexagonal structure, the ratio of the semi-major and semi-minor axis (r_l/r_s) corresponding to the equivalent ellipse for the different films on differently-terminated Si substrates. The subscripts i and f represent parameters corresponding to the initial and final time of measurements, respectively.

Sample	b(nm)	c_i(nm)	c_f(nm)	$(r_l/r_s)_i$	$(r_l/r_s)_f$
CTAB-SiO/Cl-Si	5.27	7.48	7.28	1.22	1.25
CTAB-SiO/OH-Si	5.25	7.38	7.24	1.23	1.26
CTAB-SiO/H-Si	5.26	6.94	6.92	1.31	1.32

the substrate, which is gradual and wide. This is unlike the CTAB-SiO/OH-Si sample, where an intermediate plateau region corresponding to the silica layer is present, and also unlike the CTAB-SiO/H-Si sample, where the dip is quite sharp and narrow. The nature of the dip after the substrate in the CTAB-SiO/Cl-Si sample is more like that of the dip after the plateau region in the CTAB-SiO/OH-Si sample. This suggests that the silica coated cylindrical micelles are directly adsorbed onto the Cl-Si surface, which clearly indicates the weakly hydrophilic nature of the Cl-Si surface. Correspondingly, the value of d for the CTAB-SiO/Cl-Si sample is found to be similar to that for the CTAB-SiO/OH-Si sample. With time the width and sharpness of the dip near the substrate for the CTAB-SiO/Cl-Si sample decreases and increases, respectively, which is related to the change in the shape of the micelles from nearly circular to more elliptical, mainly due to the drying of the film that is strongly attached to the substrate.

5.2.2.4 GISAXS: Hydrophilic/hydrophobic nature from in-plane and out-of-plane structures of deposited film

GISAXS patterns of the dried CTAB-silica mesostructured films on differently-terminated Si substrates are shown in Fig 5.6. (02) and (11) Bragg spots, signatures of a compressed 2D-hexagonal structure, are evident in all the patterns. In-plane (b) and out-of-plane (c_f) structural parameters for all the dried films, extracted from GISAXS spots with an accuracy better than $\pm$ 0.02 nm, are listed in Table 5.2. The value of c_i (=$2d$) for all three films obtained from the initial XR measurements (Table 5.1) are also listed in Table 5.2. The distance between the (11) planes for the films on all the substrates is the same. This means that although the initial attachment of the films and the out-of plane

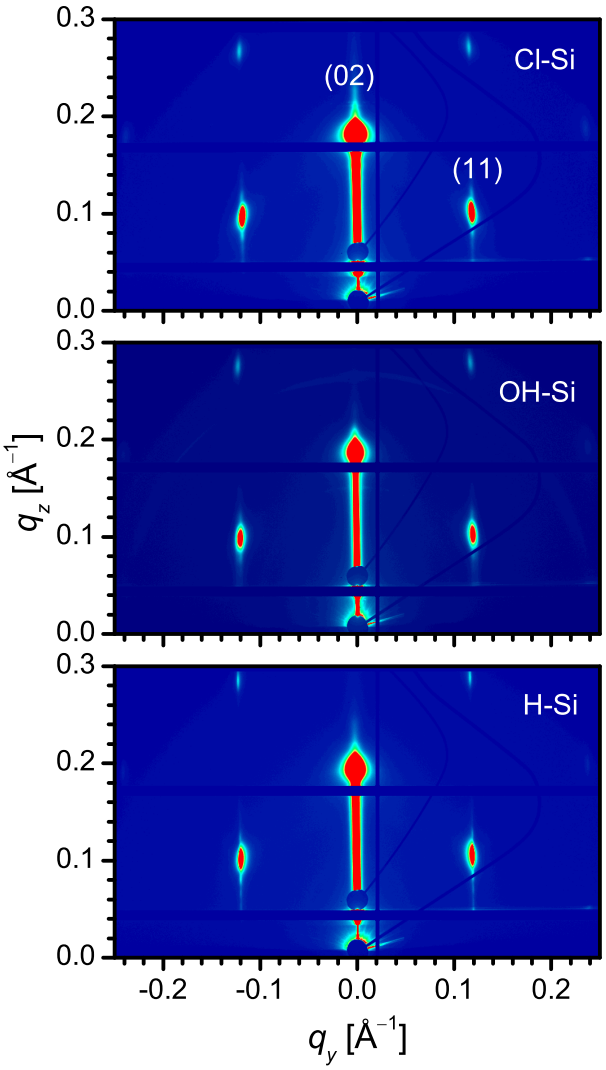

Figure 5.6: GISAXS patterns of the CTAB-silica dried films on differently-terminated Si substrates, showing (11) and (02) Bragg spots of the compressed 2D-hexagonal structure.

distance of the micelles are different on differently-terminated substrates, the in-plane distance between the micelles is the same. The ratios of the semi-major and semi-minor axis (r_l/r_s) which is estimated from $\sqrt{3}/(c/b)$ are listed in Table 5.2. The value of r_l/r_s for the film on H-Si is more compared to that on OH-Si, as reported in previous chapter.[56] The value of r_l/r_s for the dried film on the Cl-Si is similar to that for the film on the OH-Si, while the value for the as prepared film on Cl-Si is even smaller compared to that for the film on OH-Si. This indicates that the micelles are most elliptical on the H-Si substrate and least elliptical (i.e. more circular) on the Cl-Si substrate during the initial stages of the film formation.

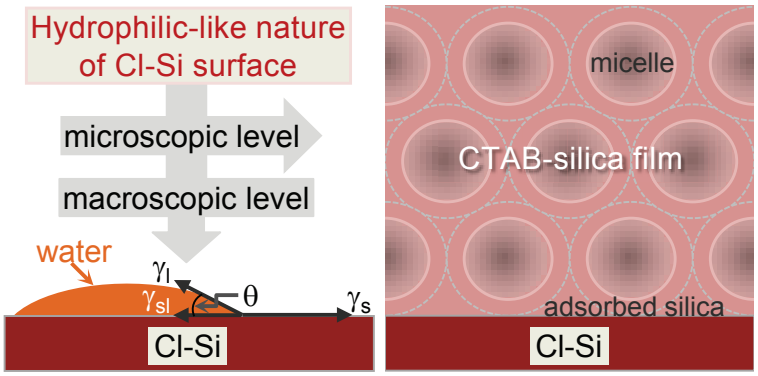

Figure 5.7: Schematic of the wetting with water (on a mm length scale) and the structure of the CTAB-silica film (on a nm length scale) on the weakly hydrophilic Cl-Si surface as predicted from the CA, XR and GISAXS measurements. The surface free energy of solid (γ_s), liquid (γ_l) and interfacial energy (γ_{sl}) dictates the CA (θ) value and the wetting. The adsorbed silica dictates the shape of micelles and the structure of the film.

5.2.2.5 Weakly hydrophilic nature and possible origin

An intermediate wetting behavior of the Cl-Si surface compared to the OH-Si and H-Si surfaces was observed from the CA measurements, which was more similar to that of the OH-Si surface, i.e. the Cl-Si surface is weakly hydrophilic in nature from a macroscopic point of view. The same weakly hydrophilic nature of the Cl-Si surface is also obtained from the XR data analysis (i.e. from the information of the film-substrate interface). It can be noted that the adsorption of the film with the substrate takes place on the molecular level and the formation of a particular interface depends on the nature of the substrate surface on the molecular or microscopic level. The information on the shape (r_l/r_s) of the micelles inside the films in the initial stages, which is induced by the substrate surface nature, however, suggests that the Cl-Si surface is weakly hydrophilic, similar to that of the OH-Si surface or even stronger. So from both the macroscopic and microscopic point of view, as shown schematically in Fig. 5.7, the Cl-Si surface is weakly hydrophilic in nature.

In the wet chemical process, the H atoms of the H-Si surface are exchanged with Cl atoms. The relatively strong electronegativity of Cl atom, listed in Table 5.3, helps to replace the H atom, leaving the surface Cl-terminated. On the other hand, large atomic size of Cl prevents such replacement due to steric-hindrance, especially for the Si(100) surface (where two H-saturated dangling bonds corresponding to a single Si atom need

Table 5.3: The covalent atomic radii (R_a), the electronegativity (δ) on Pauling scale, the bond-energy (D_B) with Si and the bond-length (L_B) with Si for different elements, as obtained from online sites.[75,76]

Element	R_a (Å)	δ	D_B (kJ/mole)	L_B (Å)
Si	1.11	1.90	222	2.33
Cl	0.99	3.16	381	2.02
O	0.73	3.44	452	1.63
H	0.37	2.20	318	1.48

to replace) and also for the rough surface (where the access to H-saturated dangling bonds near the dip is restricted). A high atomic roughness of the H-Si(100) surface compared to the H-Si(111) surface is usually observed.[83] Thus, both steric-hindrance and high roughness make the H-Si(100) surface relatively difficult to terminate with Cl compared to the H-Si(111) surface. This is also consistence with the surface roughness value of the Cl-Si(111) and Cl-Si(100) samples (about 0.54 and 0.96 nm, respectively) as obtained from the analysis of the XR data (not shown here). Even the Si(111) surface is not completely terminated with Cl under most experimental conditions. A few H atoms are never replaced with Cl atoms and a few Cl atoms are further replaced with O atoms. In our case, the presence of the Cl ($2s$, $2p_{1/2}$ and $2p_{3/2}$) and Si ($2p_{1/2}$ and $2p_{3/2}$) peaks and the absence of any significant silicon oxide peak in the XPS scans (Fig. 2.18) clearly suggests that the Cl-Si(111) surface is mostly Cl-terminated.

The weakly hydrophilic nature of the Cl-Si surface compared to the H-Si surface can be well realized considering the polar-nonpolar nature. The electronegativity difference between Cl and Si (1.26) is greater than that between H and Si (0.30), which makes the former polar and hydrophilic, while the latter is nonpolar and hydrophobic. The electronegativity difference between O and Si (1.54) is quite high, but still the O-Si surface is not quite hydrophilic; this is because each O atom is connected to two Si atoms resulting in a decrease in the value of the effective electronegativity difference. The very strong electronegativity of the OH group makes the OH-Si surface highly polar and hydrophilic. The high hydrophilicity of the OH-Si surface is also related to the hydrogen bonding ability of this surface with the water molecules, which is not possible for the Cl-Si surface. Due to the strong electronegativity of Cl, however, it is able to attract water molecules and other hydrophilic particles even better, as observed

for the CTAB-silica film. The lower wettability of the completely converted Cl-Si surface compared to the OH-Si surface is likely to be due to the absence of hydrogen bonding in the former. In reality, the Cl-Si surface is not completely (though mostly) terminated with Cl. A few different atoms that may present are distributed uniformly, making the Cl-Si surface homogeneous but comparatively less hydrophilic as observed from the CA measurement. Silica coated cylindrical micelles are adsorbed through their silica parts onto this homogeneous and weakly hydrophilic Cl-Si surface. However, the presence of different atoms probably restricts the length of the cylinder, which helps the micelles above to relax and to form slightly more circular cylinders compared to those on the OH-Si surface as observed from the r_l/r_s values at the initial stages. The attachment of the silica layers with the Cl-Si surface is, however, quite strong, which creates strong asymmetric stress on the micelles while drying, especially near the substrate.

5.3 Time evolution of a Cl-terminated Si surface at ambient conditions

The stability of the Si surface after passivation with different materials (such as O, H, Cl, etc.) can be different depending upon their bond strength and relative electronegativity. Moreover, the stability of a passivated surface depends on the environments, namely humidity of air, oxygen content in air, dissolved oxygen in water and metal impurity on the surface.[55,58,60,89,90,183] Native oxide is normally grown on the Si surface desorbing the passivated atoms. Thus understanding the growth of oxide layer is one way to understand the stability-instability of a passivated surface. Soft X-ray photoelectron spectroscopy (SXPS)[90] and high-resolution electron energy loss spectroscopy (HREELS)[89] were used to identify the presence of silicon oxide on the surface and its growth with time. Oxidation can change the chemical nature and/or the roughness of the surface, which in turn can change the hydrophilic-hydrophobic nature of the surface. However, not much work is carried out to understand the stability-instability information on the Cl-Si surface, from the point of view of hydrophilic-hydrophobic nature of the surface.

In this study, simple CA measurements which provide macroscopic level information along with the X-ray scattering technique were used to monitor the evolution of the Cl-Si surface with time in ambient condition. The structures of the CTAB-silica 2D-hexagonal mesostructured films deposited at different point of time were estimated by the complementary XR and GISAXS techniques and were used to understand the evolution of the Cl-Si surface in microscopic level from the point of view of hydrophilic-hydrophobic nature of the surface. Transition from weak-hydrophilic toward weak-hydrophobic nature of Cl-Si surface is clearly evident with time. The characteristic transition time is estimated, and the possible reasons for such transition are discussed.

5.3.1 Experimental details

Just after preparation, Cl-terminated Si (111) substrates were kept at ambient conditions [with constant temperature ∼25°C and relative humidity ∼40%] for different durations. Time-evolved substrate is referred as Nd, where N indicates the time (in days) for which it is kept at ambient conditions. For as-prepared substrate $N = 0$. CA measurements of Cl-Si(111) samples were carried out just after preparation and subsequently in different days to investigate the evolution of the hydrophilic-hydrophobic nature of the surface with time. XR measurements of Cl-Si samples were performed just after preparation (within a day) and subsequently in different days to study the stability and reactivity of the samples at ambient conditions.

The CTAB-silica solution prepared in a two-step process was diluted by adding excess ethanol (of amount 35 cm^3) and 2D- hexagonal mesostructured thin films were prepared from that solution (at temperature 25-30°C and relative humidity 70-75%) using a spin-coater on different time-evolved Cl-Si substrates. XR measurements of the as-prepared and dried CTAB-silica mesostructured films on different time-evolved Cl-Si substrates were carried out using a lab source and GISAXS measurements of the dried CTAB-silica mesostructured films on different time-evolved Cl-Si substrates were performed in MiNaXS beam line (P03) at the third generation synchrotron source PETRA III of Deutsches Elektronen-Synchrotron (DESY), Germany.

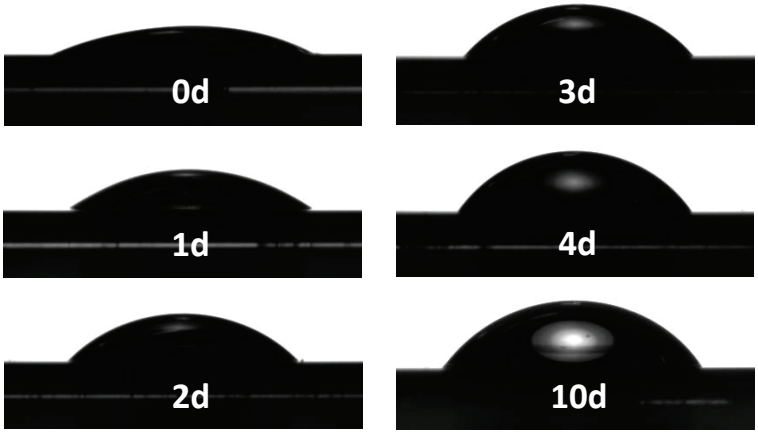

Figure 5.8: Typical images of water drops on a time-evolved Cl-Si substrate. Nd indicates the substrate that is evolved for N days at ambient conditions.

5.3.2 Results and discussion

5.3.2.1 CA: Evolution from wetting-dewetting of water

The hydrophilic-hydrophobic nature of a surface and its evolution with time, in the macroscopic level, can be easily estimated from the wetting-dewetting of water, i.e., from the CA measurements. Typical images of water drops on a time-evolved Cl-Si substrate are shown in Figure 5.8. Dewetting with time is clearly evident from these images. Corresponding average value of CA (θ_c) with error bar are plotted as a function of time (t) in Figure 5.9. The value of θ_c increases with time, which is initially fast then saturates with time. Such variation of θ_c can be expressed quantitatively using standard exponential dependence:

$$\theta_c = \theta_{c0} + \Delta\theta_c(1 - e^{-t/\tau}) \tag{5.1}$$

where θ_{c0} is the CA of the Cl-Si surface at $t = 0$, $\Delta\theta_c$ is the maximum change in the CA with time at ambient condition, i.e. the CA of the Cl-Si surface at $t \to \infty$ is $\theta_{c\infty} = \theta_{c0} + \Delta\theta_c$, and τ is the critical transition time. The variation of θ_c has been fitted using eq (5.1) and the fitted profile is shown in Figure 5.9. The parameters obtained from the fitting are $\theta_{c0} \approx 24°$, $\theta_{c\infty} \approx 60°$, and $\tau \approx 50$ h. Although there are diversity in the definitions of hydrophilic and hydrophobic surfaces, a recent review article[180] proposed different measures and classifications of the hydrophilic-hydrophobic nature of solid surfaces based on different parameters such as the contact angle, the water

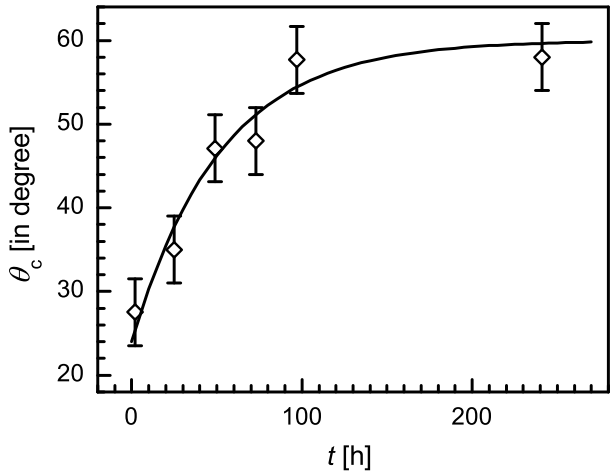

Figure 5.9: Variation of contact angle (θ_c) of Cl-Si surface with time at ambient conditions. Symbols are the experimental data and the solid line through the data is the analyzed curve.

adhesion tension, the work of spreading or the energy of hydration. Accordingly, $0 < \theta_c < 56^\circ - 65^\circ$ is termed as weak-hydrophilic and $56^\circ - 65^\circ < \theta_c < 90^\circ$ is termed as weak-hydrophobic surface. Following this classification, the transition in the nature of the Cl-Si surface at ambient conditions is from weak-hydrophilic toward weak-hydrophobic and the critical time for such transition is about 50 h.

5.3.2.2 XR: Evolution from electron density profile of surface

XR data (R) normalized with Fresnel's reflectivity (R_F) for a time-evolved Cl-Si substrate are shown in Figure 5.10. A dip is present in all the apparently featureless curves. The dip becomes sharper and its position shifted toward the left with time, indicating probable increase in the roughness of the substrate surface. To have a better idea about the nature of the substrate surface, the XR data have been analyzed using Parratt's formalism.[121] For the analysis, a layer on the top of the substrate is assumed. Considering roughness (σ), layer thickness (d_{ox}) and electron density (ρ) as parameters, the XR data have been analyzed. Best fitted curves along with the XR data for the Cl-Si substrate measured initially (0d) and after 10 days (10d) are shown in Figure 5.11. Corresponding EDPs and their derivatives are shown in the insets of Figure 5.11. Decrease in the value of ρ on the top part of the substrate with time is evident from the EDPs. Such low

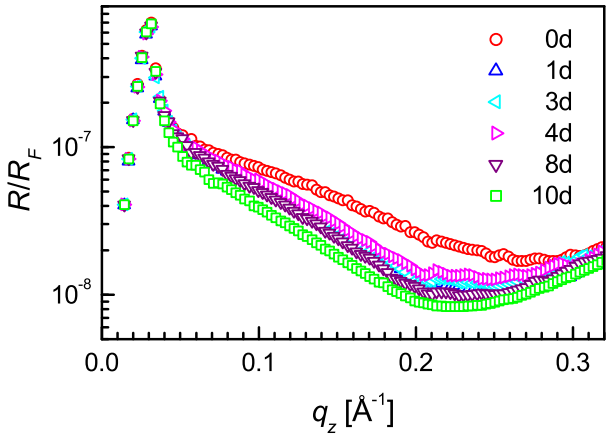

Figure 5.10: Normalized XR data of a time-evolved Cl-Si substrate. Nd indicates the substrate that is evolved for N days at ambient conditions.

density layer corresponds to the oxide layer. The values of σ (about 0.54 and 0.56 nm) and d_{ox} (about 0 and 1.4 nm), estimated from the derivatives of the EDPs (0d and 10d), suggest no appreciable increase in the roughness with time but growth of oxide layer on Cl-Si substrate.

5.3.2.3 XR: Evolution from interface and out-of-plane structures of deposited film

XR data of the as-prepared CTAB-silica mesostructured films on different time-evolved Cl-Si substrates are shown in Figure 5.12. Two strong pseudo-Bragg peaks are visible in all the curves, which correspond to the first and second orders of the (02) Bragg peak for the 2D-hexagonal mesostructure,[158] suggesting the formation of well-ordered compressed 2D-hexagonal structure,[56] as shown schematically in the inset of Figure 5.12. Kiessig fringes, which are the measure of the total film thickness, are very clearly visible for all the XR profiles before first Bragg peak. The nature of the fall of XR profile after the first Bragg peak is found different for the different films. The fall, which is sharp for the film on 0d substrate, became gradual for the film on 8d substrate. This may be due to the change in the film-substrate interface. The values of c_i (i.e. $2d_{02}$) obtained from the (02) Bragg peak positions for the as-prepared films on 0d and 8d substrates are tabulated in Table 5.4 with an accuracy better than $\pm$ 0.02 nm. Small change in the value of c_i is observed, which may be related to the change in the shape of the micelles

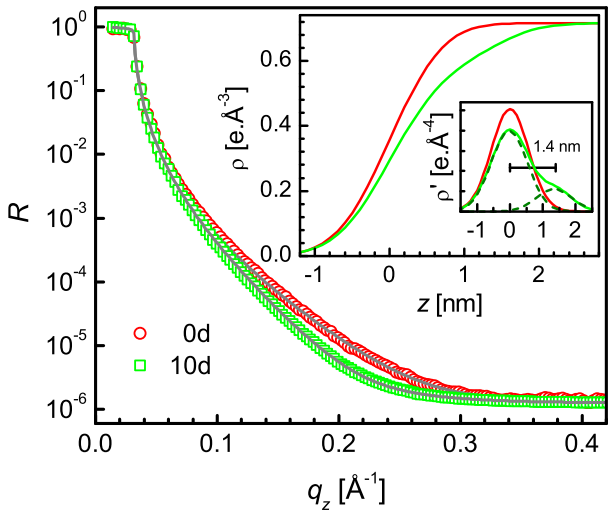

Figure 5.11: XR data (different symbols) and analyzed curves (solid line) of Cl-Si substrate measured initially (as-prepared) and finally (after evolved at ambient condition for 10 days). Inset: corresponding EDPs and their derivatives.

due to the change in the interface. Similarly, the intensity of the first- and second-order Bragg peaks for the film on 8d substrate are about 5 and 12 times less compared to the peaks for the film on 0d substrate, indicating deterioration in the ordering, probably due to the change in the interface.

To get further information about the structure of the films, especially about the film-substrate interface, the XR data have been analyzed considering a model of oscillatory electron density profile (EDP), arising from periodic repetitions of two stacked layers as considered before (as shown schematically in the inset of Figure 5.12).[56] In addition, special attention is paid to the initial layer through which the film is attached with the substrate, as it decides the nature of the substrate surface. Based on this model, the best fit XR profiles for the films on 0d an 8d substrates are shown in Figure 5.12 along with the corresponding EDPs in the inset. Similar to the bare substrate, the growth of oxide layer (i.e. decrease in the value of ρ) on the top part of the substrate with time is evident from the EDPs. Small decrease in the value of d_{02} and in the contrast between two consecutive layers are also observed for the film, which may be related to the change in the shape of the micelles from nearly circular to more elliptical, change in the film-substrate attachment from strong to weak and deterioration in the ordering.

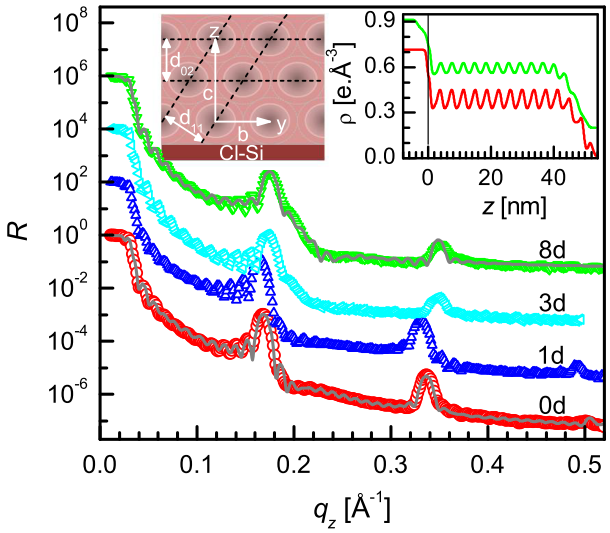

Figure 5.12: XR data (different symbols) and analyzed curves (solid line) of the as-prepared CTAB-silica mesostructured thin films on different time-evolved Cl-Si substrates (curves are shifted vertically for clarity). Nd indicates the substrate that is evolved for N days at ambient conditions. Insets: schematic of a compressed 2D-hexagonal structure showing unit cell parameters (b and c) and lattice spacings (d_{02} and d_{11}) for an equivalent centered rectangular ($c2mm$) unit and analyzed EDPs of the films on initial (as-prepared) and finally evolved (after 8 days) substrates.

5.3.2.4 GISAXS: Evolution from in-plane and out-of-plane structures of deposited film

GISAXS patterns of the dried CTAB-silica mesostructured films on different time-evolved Cl-Si substrates are shown in Figure 5.13. (02) and (11) Bragg spots, signatures of a compressed 2D-hexagonal structure, are evident in all the patterns. Weak (13) Bragg spot is also evident in all the patterns. To have better idea about the positions of the spots, line profiles along q_z and q_y directions and through the (02) and (11) Bragg

Table 5.4: In-plane (b) and out-of-plane (c) unit cell parameters of the compressed 2D-hexagonal structure, the ratio of semi-major and semi-minor axis (r_l/r_s) corresponding to the equivalent ellipse for the films on as-prepared (0d) and time-evolved (8d) Cl-Si substrates obtained from XR and GISAXS measurements. Subscripts i and f represent parameters corresponding to the film at initial and final stages of measurements, i.e., for the as-prepared and dried film, respectively.

Substrate	c_i (nm)	c_f (nm)	b_f (nm)	$(r_l/r_s)_i$	$(r_l/r_s)_f$
0d	7.48	7.28	5.3	1.22	1.25
8d	7.16	7.06	5.1	1.23 (1.28)	1.25

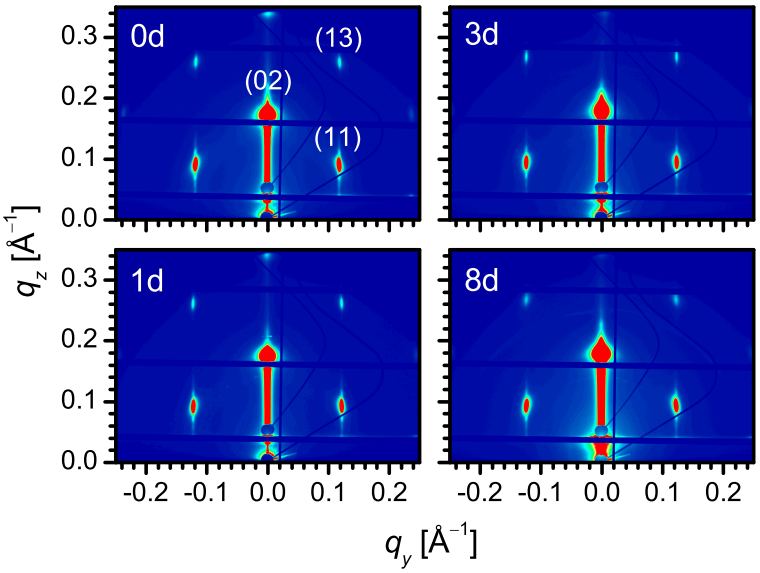

Figure 5.13: GISAXS patterns of the dried CTAB-silica mesostructured thin films on different time-evolved Cl-Si substrates, showing (02), (11) and (13) Bragg spots of the compressed 2D-hexagonal structure. Nd indicates the substrate that is evolved for N days at ambient conditions.

spots for the films on 0d and 8d substrates are plotted in Figures 5.14 and 5.15, respectively. The change in the position of peaks for the two films are clearly evident. The values of c_f and b_f, obtained from the peaks with an accuracy better than $\pm$ 0.02 nm, are tabulated in Table 5.4. The decrease in the value of c_f is observed similar to c_i, but the change is small. The decrease in the value of b_f is also observed, unlike our previous studies,[56,57] which is interesting to note. Considering $b_i = b_f$, the ratio of semimajor and semiminor axis (r_l/r_s) of equivalent ellipse is estimated from $\sqrt{3}/(c/b)$ and is listed in Table 5.4. The values of r_l/r_s for the dried films on both the substrates are found same, while that for the as-prepared films on 8d substrate is found slightly large compared to that on 0d substrate. It can be noted that we have assumed $b_i = b_f$. This is a valid assumption if the film-substrate interaction is strong, as expected for the film on 0d substrate. However, if the film-substrate interaction is weak, which may be a possibility for the film on 8d substrate, then b_i can be greater than b_f. Considering same b_i-value (5.3 nm) for both the as-prepared films, the value of $(r_l/r_s)_i$ for the film on 8d substrate is recalculated and shown in parentheses in Table 5.4. This confirms that the micelles are less elliptical (i.e. more circular) on the 0d substrate and more

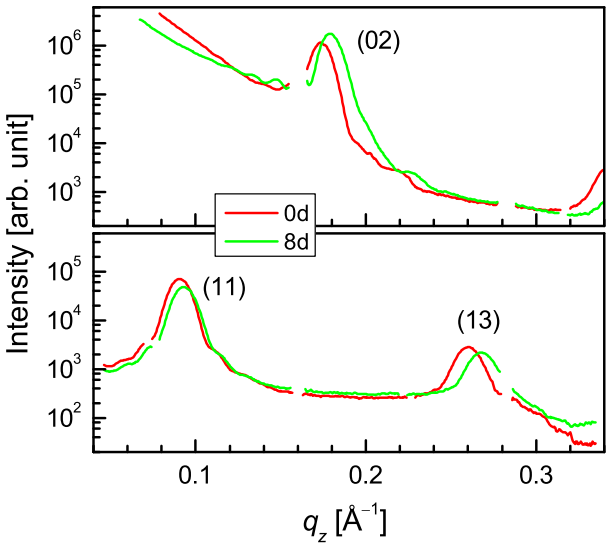

Figure 5.14: GISAXS line profiles along q_z direction and through (02) and (11) Bragg spots for the dried CTAB-silica mesostructured thin films on as-prepared and 8 day-evolved Cl-Si substrates.

elliptical on the 8d substrate during the initial stages of the film formation, as predicted from the XR data analysis. Further with time, the shapes of the micelles on both the substrates become almost the same. This also indicates that the attachment of the film on the 0d substrate is strong, while that on the 8d substrate is weak.

5.3.3 Time evolution of Cl-Si surface and proposed mechanism

The evolution of Cl-Si surface with time at ambient conditions, obtained from different measurements, is shown schematically in Figure 5.16. Evolution in the nature of surface from weak-hydrophilic toward weak-hydrophobic, in macroscopic scale, is evident from the change in the wetting-dewetting properties of water. It is well-known from SXPS[90] and HREELS[89] studies that at ambient conditions oxide grows on the Si surface desorbing the Cl from the Cl-Si surface. EDPs of bare substrate obtained from the XR measurements support the growth of oxide layer, the roughness of which is found slightly large, probably due to the inhomogeneous growth of oxide layer with time. Structures of the CTAB-silica mesostructured films show transition from strongly attached near circular micelles to weakly attached more elliptical micelles, suggesting similar transition of Cl-Si surface from weak-hydrophilic toward weak-hydrophobic with time even in

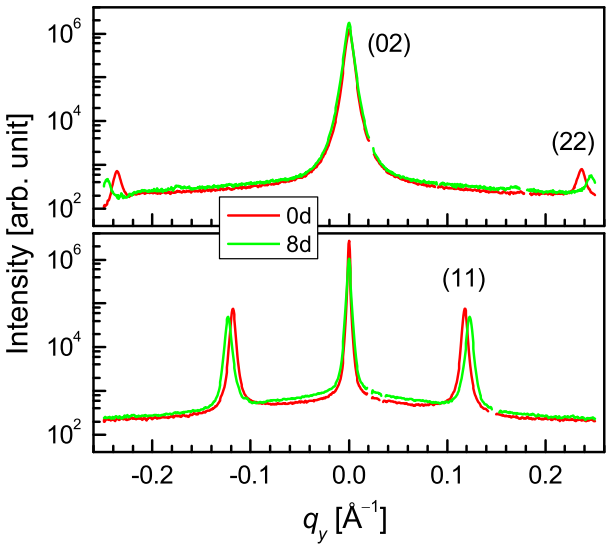

Figure 5.15: GISAXS line profiles along q_y direction and through (02) and (11) Bragg spots for the dried CTAB-silica mesostructured thin films on as-prepared and 8 day-evolved Cl-Si substrates.

microscopic level. The hydrophilic-hydrophobic nature of a surface can arise from its chemical (such as Cl, O, etc.) and/or structural (such as low or high height fluctuation or roughness) natures. Here negligible change in the roughness is observed, suggesting that the variation of θ_c with time is mainly due to the growth of oxides on the Cl-Si surface, similar to that indicated for other passivated-Si surface.[55,59] Also, the exponential decay term corresponds to the desorption of Cl from the Cl-Si surface, similar to that indicated for the Br-Si surface from X-ray standing wave studies.[184] Thus, the critical time of transition, which is found to be about 50 h, essentially represents the critical oxide growth time or the critical stability-instability time of the Cl-Si surface at ambient conditions.

The evolution of hydrophilic-hydrophobic nature of the Cl-Si surface at ambient conditions can be well realized considering its polar-nonpolar nature. The relatively strong electronegativity difference between Cl and Si (1.26),[75] makes the as-prepared Cl-Si surface relatively polar and weak-hydrophilic.[57] Similarly, the electronegativity difference between O and Si (1.54) is quite high,[75] but each O atom is connected to two Si atoms, which makes the effective electronegativity difference quite low. Such relatively low electronegativity difference is probably responsible for the relatively nonpolar and

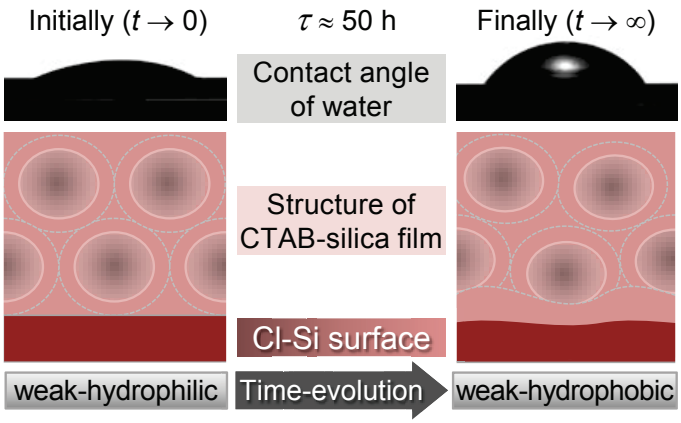

Figure 5.16: Schematic of the wetting-dewetting of water (in mm length scale) and the structures of the CTAB-silica films (in nm length scale) on as-prepared and time-evolved Cl-Si surfaces as predicted from the CA, XR and GISAXS measurements, suggesting weak-hydrophilic (Cl-Si) to more toward weak-hydrophobic (O-Si) transition with time and providing characteristic transition or stability time (τ).

more toward weak-hydrophobic nature of the oxide grown Si surface. Accordingly, relatively wetting and dewetting natures of water are found in as-prepared Cl-Si and oxide grown Si surfaces. Further, silica coated cylindrical micelles of near circular shape are adsorbed through their silica parts onto this homogeneous and weak-hydrophilic Cl-Si surface to form well ordered structure. The attachment of the film to the Cl-Si surface is quite strong, which creates strong asymmetric stress on the micelles while drying, especially near the substrate. On the other hand, hemicylindrical micelles or cylindrical micelles of elliptical shape are attached onto the oxide-grown Si surface, which is more toward weak-hydrophobic and less homogeneous to form less ordered structure. The attachment of the film to the oxide-grown Si surface is quite weak, which tries to release the stress of the micelles while drying.

5.4 Conclusions

The wettability or hydrophilicity of a Cl-terminated Si surface prepared by a wet chemical process and the stability-instability of such surface under ambient condition was examined using different parameters. Chlorination of Si surfaces with different orientations was confirmed by XPS measurements. As Si(111) surface shows better passivation with -Cl atom compared to Si(100) surface, the rest of the measurements were performed

on Cl-Si(111) surfaces. The CA of the Cl-Si(111) surface was found to be intermediate between OH-Si and H-Si, but closer to that of the OH-Si surface, indicating the weakly hydrophilic nature of the Cl-Si surface on the macroscopic level. A structural study of the CTAB-silica film on the Cl-Si substrate suggests the formation of a well-ordered, compressed 2D-hexagonal structure, similar to those observed for the films on the OH-Si and H-Si substrates. Their structural stability suggests quite a strong interaction between the film and the substrate and not much change in the substrate surface nature with time. Silica molecules adsorbed onto the Cl-Si surface to form a silica layer, similar to that observed for the hydrophilic OH-Si surface and unlike that for the hydrophobic H-Si surface, where the hydrophobic parts of the CTAB molecules adsorbed to form hemicircular micelles. Also, the shape of the micelles (which is induced through initial attachment) on the Cl-Si surface is nearly circular, similar to that observed on the OH-Si surface (less elliptical) and unlike that observed on the H-Si surface (more elliptical). Both of these results suggest a weakly hydrophilic nature of the Cl-Si surface even on the molecular or microscopic level.

Investigating the initial nature of Cl-Si(111) surface, stability-instability of that surface was directly monitored by CA measurement. Initially low ($\sim$24°) CA-value of the as-prepared Cl-Si surface finally becomes relatively high ($\sim$60°) when kept at ambient conditions for a sufficient time. This indicates transition in the nature of surface from weak-hydrophilic toward weak-hydrophobic with time. EDPs suggest that such transition is mainly associated with the growth of oxide layer. That means Cl-Si becomes O-Si. However, oxide growth with time is not homogeneous or uniform. Structures of CTAB-silica mesostructured films on as-prepared and time-evolved Cl-Si substrates indicate that silica coated cylindrical micelles of near circular shape are adsorbed through their silica parts onto the homogeneous and weak-hydrophilic Cl-Si surface to form well-ordered structure, while hemicylindrical micelles or cylindrical micelles of elliptical shape are attached onto the oxide-grown Si surface which is less homogeneous and more toward weak-hydrophobic to form less ordered structure. The attachment of the film to the Cl-Si surface is quite strong, while to the oxide-grown Si surface is quite weak. Accordingly, previous one creates strong asymmetric stress on the micelles and latter on

tries to release the stress of the micelles, while drying. Transition from weak-hydrophilic toward weak-hydrophobic of the Cl-Si surface also provides the critical transition time ($\tau \approx 50$ h), which is a measure of its stability and critical oxide growth time at ambient conditions. The quantitative information on the stability of the Cl-Si surface, which was not available before, is of immense importance for the growth of interesting nanostructures on it.

6

Surfactant-mediated growth of nanostructures

6.1 Introduction

Metal nanoparticles, particularly gold particles (AuNPs) have attracted great attention due to their fascinating size and structure-dependent optical, magnetic, electronic and catalytic properties which is vital for fundamental science and also for technical applications like catalysis, photonics, information storage and biology.[5,91–96] AuNPs of different chemical composition, morphology (size and shape) and colloidal properties can be prepared using different synthesis processes and then dispersion as well as stabilization of the nanoparticles can be achieved by covering them with different macromolecules such as surfactants (micelles), polymers and proteins through various interactions like covalent bond, hydrogen bond, electrostatic forces, which might alter the intrinsic chemical properties of the nanoparticles.[92–95] To maintain the intended properties of AuNPs, a simple, versatile and economically viable method is developed to synthesize stabilized AuNPs at ambient temperature in a single step process in aqueous solution of triblock copolymer (TBP) which acts as both reducing and stabilizing agent due to its amphiphilic nature.[5,99–101,104–108,185] Researchers have shown that, in this process the formation and growth mechanism of AuNPs strongly depend on different parameters of TBP micelle,[105–107,109] systematic investigation of which is very important.

In this present study, our prime interest is to synthesize stable, well-dispersed AuNPs with narrow size distribution by varying the pH value of aqueous TBP micellar solution which can influence the reduction of gold ion and also takes part in formation, growth

and stabilization of the AuNPs. In order to understand the effect of TBP micelle with different pH value on simultaneous reduction of gold ion and formation of AuNPs, a systematic study of static and temporal evolution of ternary mixture of TBP+ precursor gold salt+ water has done by monitoring the solution using dynamic light scattering (DLS) and Ultraviolet-visible (UV-vis) spectroscopy. Transmission electron microscopy (TEM) has also done to observe how the micelles act as template and influence the overall morphology of the AuNPs. Researchers have shown that, in the acidic media the reduction of gold ion is very slow and results in unstable large aggregated nanoparticles of various shape, whereas formation of stable and small AuNPs is expected in higher pH value.[109] So, in this study, the pH of micellar solution is varied from normal (6.82) to 11.6. Though the overall shape and size of the TBP micelle does not change depending upon the pH value of the solution, but time evolution of the ternary mixture of TBP + precursor gold salt + water is highly influenced by the pH value of aqueous TBP solution. A possible reason behind this pH dependency on the reduction of gold ion and simultaneously formation of AuNPs is discussed.

6.2 Experimental details

The synthesis of AuNPs from mixed aqueous solution of Pluronic P123 and hydrogen tetrachloroaureate (III) trihydrate ($HAuCl_4.3H_2O$) at room temperature, by the method developed by Sakai et al.[99–101] as described in chapter 2. To investigate the influence of pH value of P123 solution (5.75 mM) on the formation and growth of AuNPs, the normal pH value (∼6.82) of the as-prepared aqueous P123 solution was modified to 8.26, 9.50, 10.60, 11.18 and 11.58, by adding different amount sodium hydroxide [NaOH, Merck, 35%] solution. After changing the pH value, the P123 solutions were mixed with $HAuCl_4$ solution. All the pH value of P123 solution was measured using a pH meter. The mixed solutions prepared with P123 solution of pH value 6.82, 8.26, 9.50, 10.60, 11.18, 11.58 were labeled as Sol-7, Sol-8, Sol-9, Sol-10, Sol-11 and Sol-12, respectively.

Prior to TEM sample preparation, all mixed solutions were centrifuged with water at 12,000 rpm for 20 min to remove the free micelles from the solutions as much as possible. Samples were then prepared by placing a drop of gold colloids on a carbon

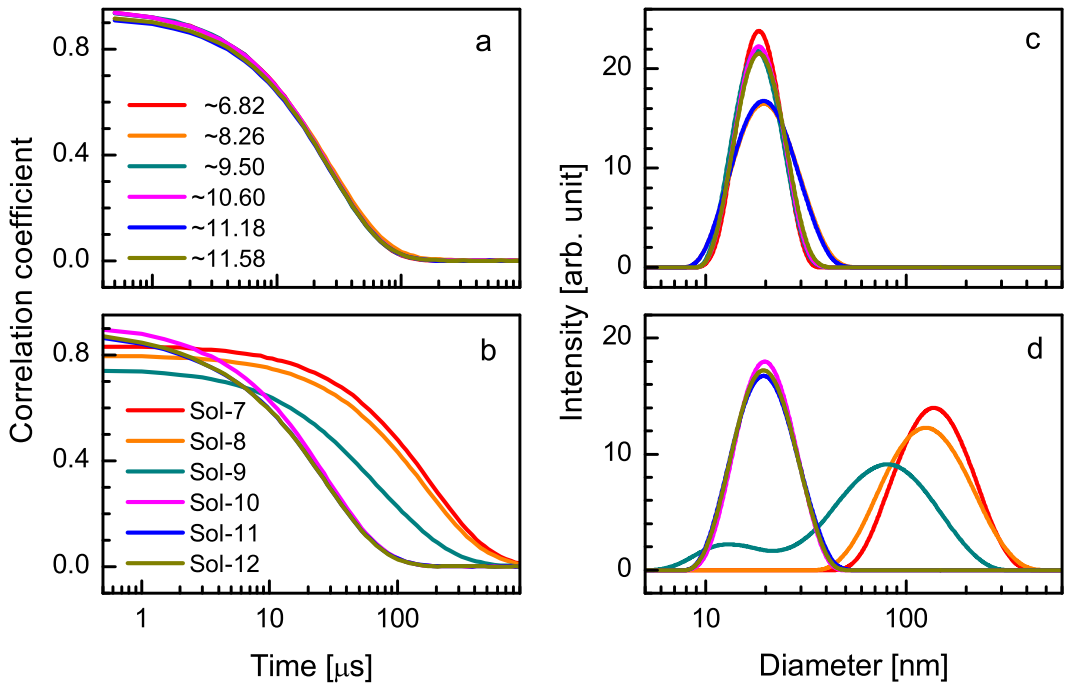

Figure 6.1: Intensity-intensity autocorrelation function, obtained from DLS data, of (a) aqueous P123 solutions and (b) AuNPs loaded P123 micelles solutions at different pH values. Corresponding size distribution graph for (c) P123 micelles and (d) AuNPs loaded P123 micelles at different pH values.

film-covered copper grid and allowed to dry in air. It should be noted that no staining agent which is usually employed to observe clearly the micellar assemblies in order to build an appropriate contrast against the bright background, has been used in the present study. TEM micrographs were analyzed using Image J software.

6.3 Results and discussion

6.3.1 DLS: Size distribution of TBP micelle and nanostructure

All the solutions were characterized using DLS technique to investigate the effect of pH value on the self assembly behavior and structure of P123 micelles in aqueous solution and to determine the size of the nanostructures formed due to homogeneous addition of aqueous $HAuCl_4$ solution in the P123 solution. Fig. 6.1(a) shows the intensity-intensity time correlation (autocorrelation) function obtained from DLS data of the pure P123 solutions (without $HAuCl_4$ solution) of different pH values. The functions are nearly

overlapped and exhibit single exponential relaxation, indicating that the size distribution of the micelles is almost same for all P123 solutions. The size distribution of the micelles at different pH values calculated from autocorrelation function are shown in Fig. 6.1(c). The average diameter of the P123 micelles remains almost same 18.5 ± 1 nm at all pH values with a narrow size distribution like normal pH ($\sim$6.82) at $\sim$25°C.[103] It is also found that the micellar size distributions exhibit a Gaussian peak indicating spherical shape of the micelles at different pH values.

The intensity-intensity time correlation function for the homogeneous incorporation of $HAuCl_4$ solution in P123 solution are shown in Fig. 6.1(b) and corresponding size distribution are shown in Fig. 6.1(d). The size distribution is strongly dependent on the pH value. The size distribution can be categorized in three different pH regions of aqueous P123 solution. At region 1, for pH $\sim$6.82 and 8.26, DLS measurement exhibits single intensity-size distribution, shifted to a larger value (around 141 and 123 nm, respectively) than that of pure P123 micelle. At region 2, for pH $\sim$9.50, dual intensity-size distribution around 13 and 77 nm is observed and finally at region 3, for pH value above 9.50, the intensity-size distribution of the nanostructure is found to be almost similar to that of free micelle ($\sim$19.3 nm). This suggests that though pH value does not influence the size and shape of free micelle in pure aqueous solution but when aqueous $HAuCl_4$ solution is added into the micellar solution the size of the newly grown nanostructures changes depending upon the solution pH value. At region 1, the radius distribution for free micelle does not come and presence of a single size intensity distribution at higher value may originates from the hybrid nanospheres resulting from the self aggregation of P123 micelle due to loading of AuNPs into the surface of it. Moreover formation of large nanoparticles or agglomeration of small nanoparticles may be the reason behind this larger size distribution peak in DLS data. As the pH increases, the size intensity distribution shifts to a lower value along with the decrease in intensity. Around pH $\sim$9.50, along with the size distribution peak at higher value, another size distribution peak at $\sim$19.3 nm originates either from normal micelles (free or nanoparticles loaded) or from free AuNPs of that size. Furthermore, at region 3 there is no signature of the larger nanostructures. The higher intensity of the size distribution peak at $\sim$19.3 nm

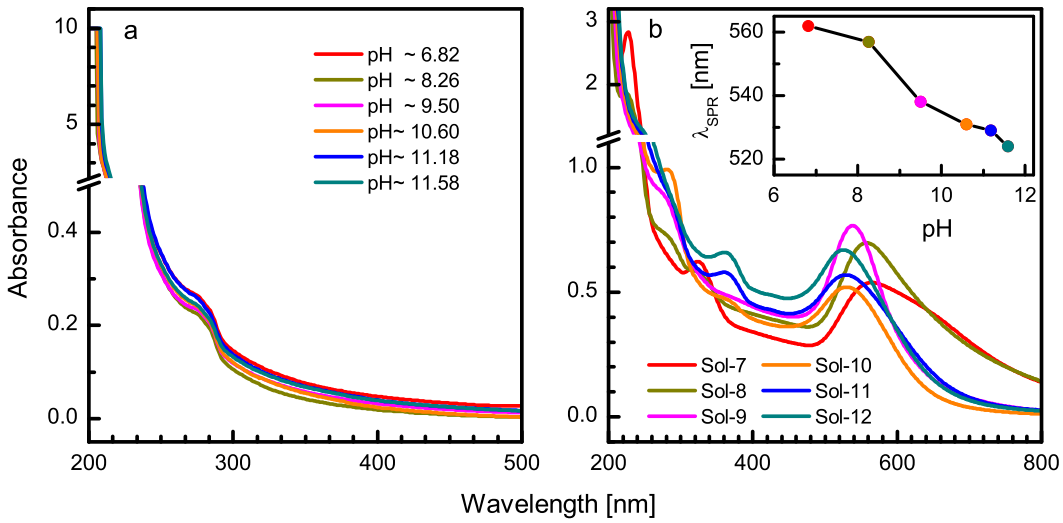

Figure 6.2: UV-vis absorption spectra of (a) aqueous P123 solution at different pH values and (b) $HAuCl_4$ + P123 + water ternary mixture prepared at different pH values (data taken after 3 h of mixing). Inset: Variation of SPR peak position (λ_{SPR}) with pH value.

compared to that of region 2 indicates that at higher pH, the density of the normal micelles (free or nanoparticles loaded) or AuNPs of smaller size in the solution increases and no agglomeration of nanoparticles or formation of larger P123 micelles occurs. The information obtained from DLS measurements allows us to predict possible size of the nanostructures formed in different solutions, but the origin of the size distributions is clear at al. To know the individual shape and size distributions of P123 micelles and AuNPs and the possible origin behind such morphology UV-vis and TEM experiments have been carried out.

6.3.2 UV-vis: Formation and growth of AuNPs

UV-vis measurements of P123 aqueous solutions of different pH values have been carried out to confirm the influence of pH value on the overall shape and size of the P123 micelles, as shown in Fig. 6.2(a). Two absorption bands centered at 205 and 280 nm are evident in the spectra.[109] The peak at lower wavelength has maximum intensity, whereas the intensity of higher wavelength peak has minimum. The position and intensity of the two absorption bands are found to be same for all pH values, indicating that though the environment of the micelles are modified by adding different amount of NaOH solution

but the intrinsic property of micelles do not alter. This result agrees well with the DLS data.

UV-vis spectra of $HAuCl_4$ + P123 + water ternary reaction mixtures, taken after 3 h of mixing are shown in Fig. 6.2(b). There are several peaks around 226, 288, 325, 366 and 530 nm in addition to the peak around 205 nm in the UV-vis spectra of the solutions and their intensity and position are different for different solutions. The peak around 205 nm remains same for all the solutions after 3 h of reaction indicating that there exists appreciable amount of unreacted P123 micelles in all the solutions at the end of the reaction. The peaks around 226 and 288 nm corresponds to the ligand (π)-to-metal (σ^*) charge transfer (LMCT) transitions in $AuCl_4^-$ ions.[109,186–188] For Sol-7, peak around 226 nm shows maximum intensity and then the intensity suddenly decreases for Sol-8 and finally disappears for the solutions with higher pH value. On the other hand, the variation of peak intensity around 288 nm is different. For Sol-7, there is no signature of the peak and gradually with increase of the pH value the peak intensity increases and finally reaches the saturation value. The next peak centered at 325 nm originates from LMCT band of gold (III) and oxygen in ether band of P123 surface cavities. 325 nm peak has maximum intensity for Sol-7 but gradually the intensity falls and finally disappears. Surprisingly, after pH value of 10.60, appearance of another peak around 360 nm starts and its intensity tends to increase for the solutions with higher pH value. Absorbance peak around 530 nm is due to the SPR from the growing AuNPs. It is evident that the shape, intensity and position of SPR peak is different for different solutions. There is a blue shift of SPR peak position as the pH of the micellar solution increases as shown in the inset of Fig. 6.2(b). It is reported earlier that the peak position, peak width, shape of the peak and also peak intensity of SPR band depend upon various parameters of the solution, like particle size, particle concentration, particle geometry, capping agents as well as the dielectric property of the surrounding medium. In the case of Sol-7 and Sol-8, the shape of the SPR absorbance band is unsymmetrical and broader, indicating the formation of anisotropic particles and particle aggregation. For Sol-9 to Sol-12, as the pH of the micelle solution increases, the peak becomes more and more symmetrical, because of the formation of the dispersed spherical nanoparticles with a narrow size

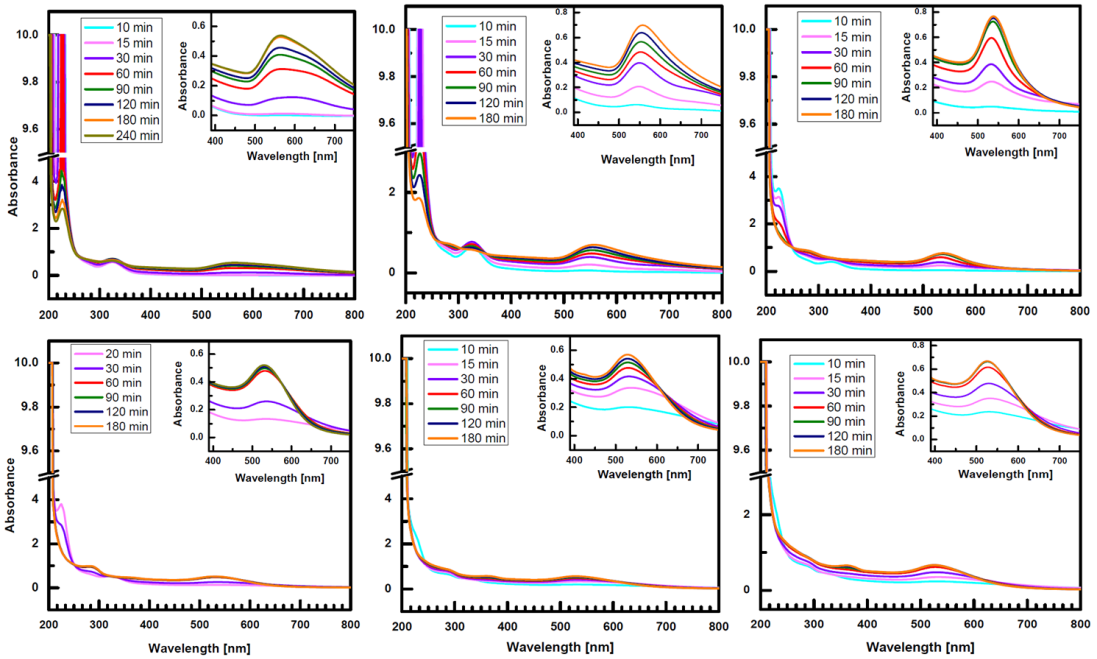

Figure 6.3: Time-evolution UV-vis absorbance spectra of the $HAuCl_4$ + P123 + water ternary mixtures of different pH values.

distribution.

To get better understanding about the influence of pH on the formation, growth and stabilization of AuNPs using P123 TBP micelle in aqueous media, UV-vis measurements have been carried out as a function of reaction-time for all the solutions, as shown in Fig. 6.3. Apart from the 205 nm peak which remains same during the whole reaction time, all other peaks (226, 288, 325, 366 and 530 nm) show appreciable time evolution for all the solutions. First of all, attention will be paid to understand the evolution of SPR peak of AuNPs with time and the appearance of other peaks and their time evolution for all the solutions will be discussed later. For that the absorbance intensity at SPR peak along with peak around 288 and 226 nm for solutions of different pH have been plotted as a function of time in Fig. 6.4. Fig. 6.3 and 6.4 gives the detail description of formation and growth of AuNPs in P123 solution. As the reaction proceeded, the concentration of the gold (III) chloride ions decreases and the intensity of plasmon band around 530 nm characteristic of AuNPs increases with time. After 30 min in the case of Sol-7 and 10 min for other solutions a significant peak around 530 nm starts to appear indicating the formation of AuNPs. It is observed that for Sol-7, with time the intensity of SPR

peak increases with a red shift of 15 nm of the same. For the other solutions, though the intensity increases with time but as the pH of the solution increases the amount of red shift decreases gradually. Even for the Sol-10 to Sol-12 (above pH value of 9.50), the peak position does not shifted at all during the reaction. The increase of SPR peak intensity is associated with the growth of AuNPs in the solutions and this red shift of SPR peak can be attributed to the significant self aggregation of the AuNPs. In the case of Sol-7 and Sol-8, initially the shape of the peak remains unsymmetrical and broader, though the width of Sol-8 is much smaller than Sol-7. This may be due to formation of anisotropic particles and aggregation of the particles. After 120 min of the reaction the width of Sol-7 becomes slightly smaller but asymmetry remains same whereas for Sol-8, after 60 min of reaction time, the peak tends to become less unsymmetrical and narrow. But with the increase of pH of micellar solution, the shape of the SPR peak during the reaction remains symmetric and the width becomes more narrower with time indicating the formation of well dispersed spherical nanoparticles with a narrow size distribution. This results agree well with the data obtained from DLS measurements. At low pH, the size of the nanostructure composed of AuNPs and P123 micelle is large, but with the increase of pH value, the size starts to decrease. It is observed that for low pH region i.e., for Sol-7, the broad SPR band is not a single one but comprise of another shoulder band around higher wavelength (635 nm), and with time as the nanoparticles grow, the intensity of this convoluted peak increases. The absorbance at higher wavelength might originate from the longitudinal plasmon resonance of the AuNPs that deviated from a spherical geometry. This longitudinal band might have resulted from gold nanorods or might be due to interparticle plasmon coupling arising due to self-aggregation of independent large colloidal AuNPs.[91] For Sol-8, initially the sign of convoluted SPR peak is reflected in the spectra, but after 90 min, the signature of several peaks dies out and only one SPR peak at lower wavelength exist. On the other hand, for Sol-9 to Sol-12, only one SPR peak is observed throughout the reaction indicating the formation of well-dispersed spherical AuNPs.

In the case of 226 nm peak, all the solutions have the same time evolution. At the starting of the reaction, the intensity of the peak is maximum followed by a rapid

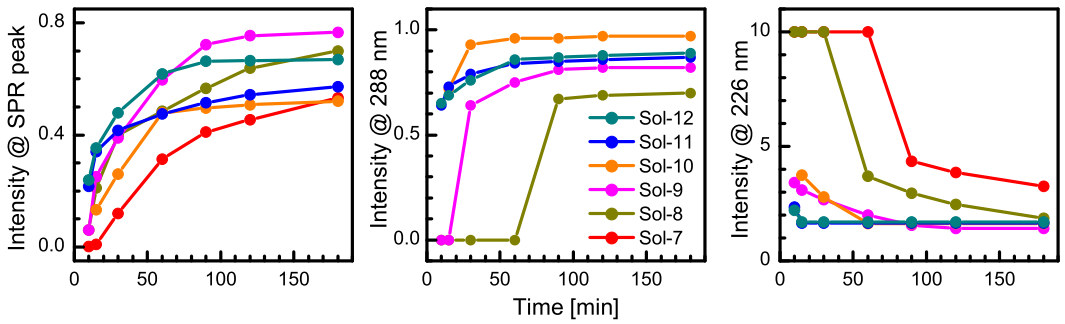

Figure 6.4: Evolution of absorbance intensity at SPR peak, 288 and 226 nm with time for solutions of different pH values.

fall and after that intensity decreases gradually due to the reduction of $AuCl_4^-$ ion into Au(0). For Sol-7 and Sol-8 the intensity starts to decrease after 60 and 30 min of the reaction, respectively, whereas in the case of Sol-9 to Sol-12, the intensity of 226 nm peak decreases very rapidly within 10 min of the reaction and then gradually falls. From this it may be said that high pH of P123 solution helps the $AuCl_4^-$ ions to reduce very fast. However, the peak intensity around 288 nm varies in opposite manner. At the starting of the reaction, there is no signature of the peak for Sol-7 to Sol-9. Even for Sol-7, there is no appreciable change in the intensity throughout the reaction. But for Sol-8 and Sol-9, the intensity rises sharply after 60 and 15 min respectively, and then with time the peak intensity increases slowly and finally saturates. For Sol-10 to Sol-12, the peak starts to rise within 10 min of the reaction and increases gradually with time and finally saturates. Theses results suggest that higher pH value of aqueous P123 solution helps the formation of LMCT band around 288 nm.

The most dramatic differences occur in the intensity variation of the peak at 325 nm originates from the LMCT band between $AuCl_4^-$ ions and PEO surface cavities as shown in Fig. 6.5. In the case of Sol-7 and Sol-8, the intensity varies in similar manner. At the initial stages of reaction, a significant increase in the intensity of the 325 nm peak happens because of the reduction of $AuCl_4^-$ ions in the surface cavities formed by PEO-PPO-PEO units which promote the formation of LMCT band and simultaneously the cavities acts as Au nucleating centers. With time, colloidal AuNPs are formed by these growing nucleating centers and indicates the completion of reaction from the gradual fall of intensity around the peak. For Sol-7, the absorbance starts to decrease after 90 min of

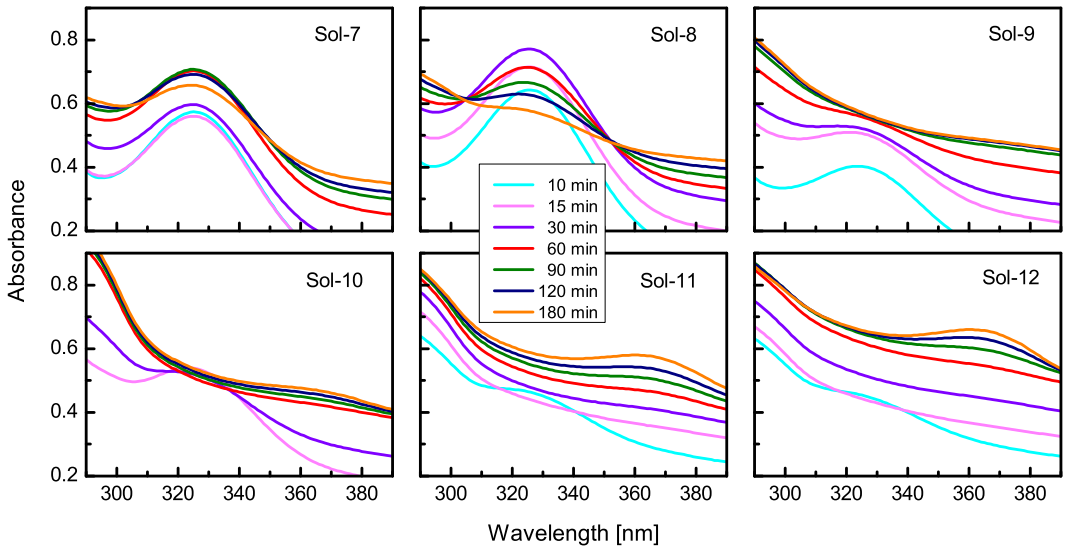

Figure 6.5: Time-dependent UV-vis spectra of $HAuCl_4$ + P123 + water ternary solutions of different pH values, showing evolution of peak near 325 nm.

the reaction, whereas in the case of Sol-8 the intensity falls after 30 min of the reaction. The rate of increase of intensity and also the rate of decrease of intensity is much faster for Sol-8 compared to that Sol-7. But the variation of absorption band around 325 nm is quite different at higher pH value (9.50, 10.60, 11.15 and 11.58). For these solutions, initially the LMCT peak intensity increases with time and after certain time the peak disappears completely. As the pH of the solution increases disappearance of the peak occurs faster (for Sol-9 after 60 min, for Sol-10 after 30 min and for Sol-11 and Sol-12 after 10 min) indicating that the higher pH value help the LMCT complex to convert completely to Au(0). Apart from that another weaker band starts to appear at higher wavelength (around 366 nm) for Sol-10 after 60 min of the reaction (after 30 min for Sol-11 and Sol-12). This band may arise due to the reduction in the energy gap between $2e_u(\pi) \rightarrow 2b_{1g}(\sigma^*)$ orbital caused by the complexation by the π-donor oxygen lone pairs of the PEO parts.[96]

6.3.3 TEM: Morphology of AuNP + TBP nanostructure

To get direct visualization of the collective morphology of the AuNPs and micellar assemblies and to understand further that how the TBP micelles formed at different

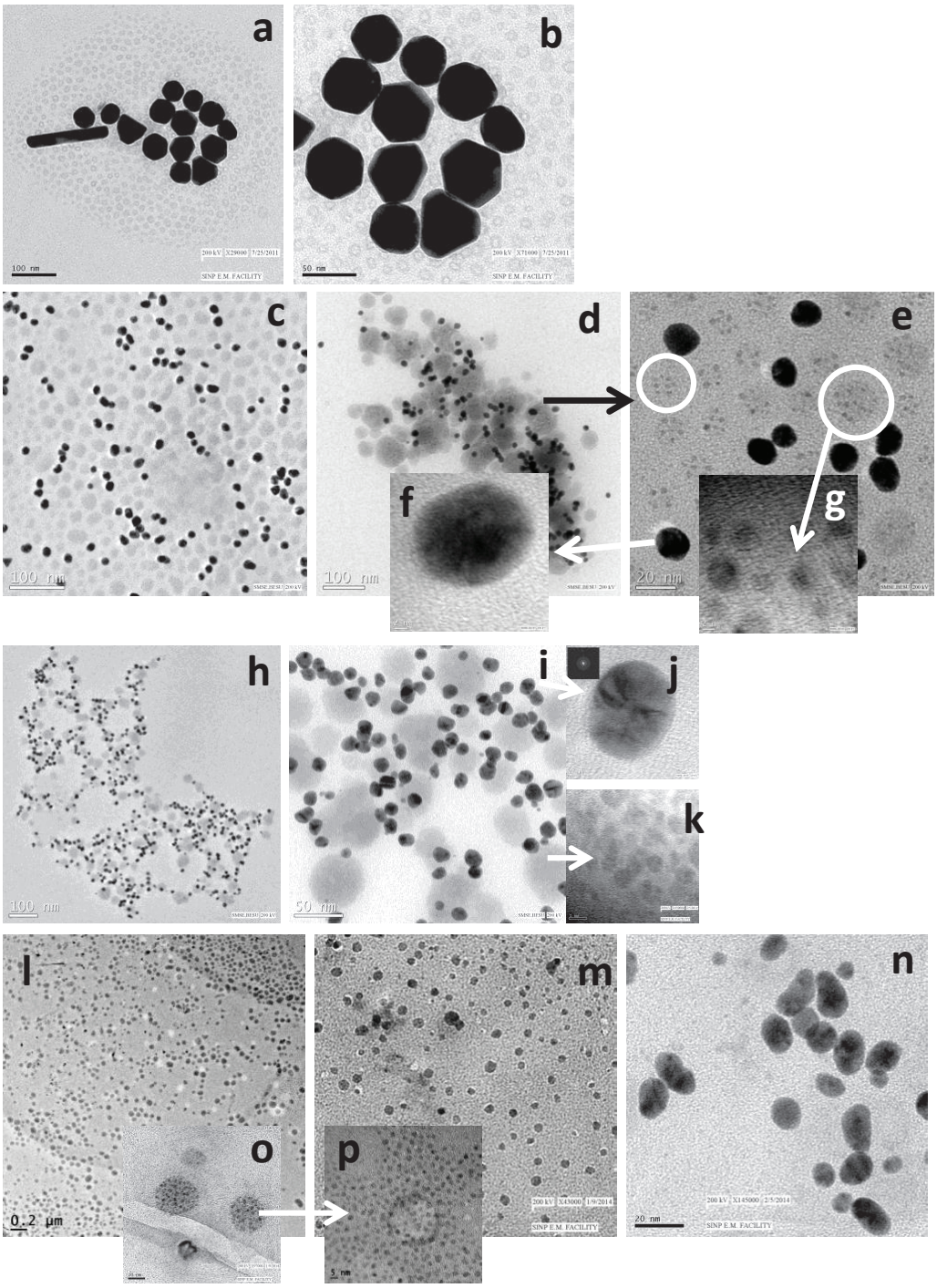

Figure 6.6: TEM images of the P123 micelles and AuNPss synthesized in the $HAuCl_4$+ P123+ water ternary solution of different pH value (a,b) 6.82, (c-g) 9.50, (h-k) 10.6 and (l-p) 11.6. The solutions are used after centrifugation in water. The scale bars represent 200nm (l), 100 nm (a,c,d,h), 50 nm (b,i,m), 20nm (e,n,o), 5nm (k,p) and 2nm (f,g,j) respectively.

pH values influence the shape and structure of the AuNPs, TEM measurements are performed on some of the samples prepared with Sol-7 to Sol-12. In the images AuNPs appear as dark spots whereas the micelle parts show lighter contrast. Fig. 6.6a shows combined image of free micelles of size around 11-12 nm and a group of few large independent AuNPs (45-60 nm) of various shapes present in the sample prepared with Sol-7. A close look at the micelles found no growing nanoparticles present on the surface (Fig. 6.6b) of it. This suggests that though the micelles take part in formation of AuNPs, but after synthesis most of the TBP micelle remains unassociated to AuNPs. Taking into account the data obtained from DLS and UV-vis measurement it may conclude that the uncoated nucleating center present on the surface cavity of the micelles self aggregate between themselves to form large nanoparticles of various shape. TEM images of the samples prepared with Sol-9, Sol-10 and Sol-12 are shown in Fig. 6.6c, h, l respectively which are very much different from that of Sol-7. For these samples, groups of well-defined nearly spherical AuNPs attach on the surface of the TBP micelles. For Sol-9, the average diameter of the micelles and AuNPs are found to be 24 nm and 13 nm respectively (Fig. 6.6c). Another image of the same sample as shown in Fig. 6.6d suggests that along with the micelles of smaller size there exist some large compound micelles (size 63, 78 nm) also. Existence of micelles of two different size region supports the presence of dual intensity size distribution as obtained in DLS measurement. A close inspection of the micelles suggests that they contain several growing nanoparticles of almost same size as evident in Fig. 6.6e. In Fig. 6.6g one such micelle has been selected to show the presence of nanoparticles of size 4 nm inside it. This suggests that in Sol-9, both the micelle and nanoparticles have dual size distribution, but in DLS measurement only the size of the micelle is reflected. For sample prepared with Sol-10, it is found that density of the AuNPs associated with the surface of P123 micelles is high as shown in Fig. 6.6h. In a closer view, it is found that the size of the compound micelle and AuNPs are 50 and 13 nm respectively. The magnified view of a single micelle indicates that the number density of nanoparticles (size 4 nm) inside it is also high compared to that on previous sample (Fig. 6.6k). Further increasing the pH value of micellar solution, free micelles are not seen at all, rather there exists only AuNPs loaded micelles of different

size as shown in Fig. 6.6l and m. The micelles are almost spherical in shape but with two different size 16±2 and 60±10 nm. As a result of close scrutiny of the micelles, it is found that there are a large population of AuNPs of size 3 nm (Fig. 6.6o and p). Apart from these small nanoparticles loaded within the micelles there also exist a large amount of elongated AuNPs of size 11±1 nm. Combining these results indicates that as the pH of the micellar solution increases, the concentration of well-dispersed AuNPs of controlled size increases along with the size of the micelle.

6.3.4 Formation and growth of AuNP in TBP solution

The results clearly shows that pH value of P123 micellar solution has significant influence on the reduction rate of gold ions, growth and stabilization of the AuNPs and also on the final self assembly of the nanoparticle-micelles nanocomposite. Before discussing this in details, let us first discuss the proposed formation mechanism of AuNPs from aqueous TBP micellar solution in a single step synthesis process. Above critical micelle concentration (*cmc*), in the aqueous solution the P123 monomers aggregate in the form of well-defined micelles. The corona of the TBP micelle is composed of hydrophilic PEO units arranged in the form of surface cavities (pseudo-crown ether structure) which can bind the $AuCl_4^-$ ions and acts as sites for the site-specific redox reaction because of the presence of ether oxygens. The redox reaction, involving the reduction of $AuCl_4^-$ ions and oxidation of the oxyethylene and oxypropylene segments of TBP micelles initiates the synthesis of the nucleating centers of AuNPs in the PEO-PPO-PEO surface cavities. The nucleating centers then undergo nucleation process to produce AuNPs. Nucleation may occurs between the nucleating centers occupying the neighboring surface cavities or through autocatalytic thermodynamically controlled reduction depending upon micellar environment and size and shape of micellar assemblies. In this study, the micellar solutions are prepared with pH values above 6.82 (basic medium) such that it can influence the reduction and also nucleation process to produce stable AuNPs with narrow size distribution and well-defined morphologies.

Generally, the strong tetrachloroauric(III) acid ($HAuCl_4$) totally dissolved in aqueous solution generating $AuCl_4^-$ complex ions of square planar geometry and produce two

absorption bands at 226 and 312 nm in UV-vis absorption spectra corresponding to the $p_\pi \rightarrow 5dx^2-y^2$ and $p_\sigma \rightarrow 5dx^2-y^2$ LMCT transitions, respectively. It is reported earlier that, in aqueous solution this $AuCl_4^-$ ion undergoes a pH dependent stepwise hydrolysis in which replacement of chloride by hydroxide ligands takes place and formation of $[AuCl_x\ (OH)_{4-x}]^-$ complex ion occurs. In the low pH region $AuCl_4^-$ ions dominate the solution and as the pH of the aqueous solution increases, $AuCl_4^-$ concentration is lowered and the contribution from $[AuCl_x\ (OH)_{4-x}]^-$ complex increases and both the absorption bands shift toward the lower wavelength due to the insertion of OH^- ions in the inner coordination sphere.[186–190] Moreover, with the increase of pH value, intensity of the band at higher wavelength (312 nm) which indicates presence of large excess of $AuCl_4^-$ ions compared to other hydroxylated species decreases and finally disappears (when pH greater than 6.16) due to the progressive increase and equalization of the energy of the p_π and p_σ orbital. In this study, as the reaction starts with the addition of aqueous $HAuCl_4$ solution in the aqueous P123 solution with high pH value (greater than 6.5), the signature of higher wavelength peak of $AuCl_4^-$ ion is absent from UV-vis absorption spectra and only the peak correspond to $[AuCl_x\ (OH)_{4-x}]^-$ complex (226 nm) exists. During the reduction of $[AuCl_x\ (OH)_{4-x}]^-$ complex ion by the PEO part of micelles to form nucleating centers H^+ ion is generated,[100,109,191] which progresses with the passage of time. This H^+ ions may disturb the binding of the metal ions to the oxyethylene group in the surface cavity of micelles, preventing the PEO part from the reduction of metal ions. As a result, at low pH the reduction rate is slow and yield of nanoparticle is low. But as the reactions take place in higher pH region, the protons are neutralized and the reduction and nucleation process is accelerated. As a result it is found that for Sol-9 to Sol-12, the intensity of 226 nm peak starts to decrease instantaneously as the starting of the reaction, but for Sol-7 and Sol-8 it takes some time. Initially, the peak intensity falls sharply and then the rate slows down. Surprisingly, at the point from which the 226 nm peak intensity starts to fall slowly, the peak around 288 nm starts to appear. This peak indicates the presence of $AuCl_4^-$ ions in the mixed solution. As the reaction proceeds, the generation of H^+ ion increases and the hydrogen bonding interaction of micelle with water becomes more strong. Consequently, this will reduce the extent of

water solvation around $AuCl_4^-$ ion and subsequent rate of Au-Cl substitution by OH. Thus as the reaction proceeds the amount of $AuCl_4^-$ ion reaches an appreciable amount in the solution. It is observed earlier that, $AuOH^-$ has lower tendency to be reduced to form AuNPs compared to that of $AuCl_4^-$.[192] In this case, at higher pH region the peak 288 nm corresponding to $AuCl_4^-$ ion starts to appear within 10 min of the reaction and accelerate synthesis of AuNPs compared to low pH region where the source of AuNPs reduction is $AuOH^-$ and reduction rate of gold ion is lower.

The reduction of Au(III) to Au(0) through the formation of Au(I) involves the LMCT formation and the produced Au(0) acts as nucleating centers for nanoparticles formation. The LMCT formation causes increase in intensity of the 325 nm peak and formation of nucleating centers produce the SPR absorption band around 530 nm. As the rate of reduction of Au(III) increases with the pH value of the P123 solution, the LMCT formation (peak around 325 nm) rate follows the same manner. Then the nucleation between the nucleating centers occurs i.e., as the Au(I) is starts to convert to Au(0) the intensity of 325 nm peak starts to decrease. For Sol-7 and Sol-8, the intensity of 325 nm peak gradually falls and exists with a constant value of intensity till the end of the reaction. This suggests that the conversion is not completed totally, and hence results in a poor yield of AuNPs. Moreover, for Sol-9 to Sol-12, there is a sudden fall of intensity of 325 nm peak to a minimum value indicating that LMCT converts fully to Au(0) resulting in maximum coverage of the micelles with small AuNPs.

At low pH region, the slow rate of reduction of gold ion and also the slow formation and then incomplete conversion of LMCT complex to Au(0) produce smaller number of nucleating centers. This nucleating centers grow larger in size due the autocatalytic thermodynamically controlled reduction of gold ions on the surface of available nucleating centers present in the surface cavity of the micelle and reduce the attractive force between the micelles. As a result a few large AuNPs of different shape are formed due to diffusion controlled nucleation among the nucleating centers which can not be supported by the soft small micelles and present in the solution as bulk phase. Moreover, when the pH value of micellar solution is high, the faster reduction rate of gold ion and simultaneous complete conversion of LMCT complex to Au(0) produce large number

of nucleating centers within the surface cavity of the micelle and promote intermicelle fusion to produce hybrid micelles of larger size. The surface cavity of the micelle acts as soft template to form AuNPs by entrapping all nucleating centers in its micellar phase. As a result, at high pH region micelles are fully loaded with large number of well-dispersed AuNPs of small size.

6.4 Conclusions

The influence of pH value of aqueous P123 micellar solution in reduction of gold salt and then nucleation and growth of AuNPs in aqueous micellar solution at ambient condition is studied using DLS and UV-vis measurements and also the self assembly of the AuNPs in P123 micelles is investigated by TEM measurements. From DLS measurements it is found that though the size of the pure micelle is not altered at different pH values, but when aqueous $HAuCl_4$ solution is added to micellar solution the size of the nanocomposite changes depending upon the solution pH value. A close investigation of UV-vis data analysis also supports the result. At higher pH value, the reduction of gold salt is accelerated along with faster LMCT formation which converts completely to Au(0). Au(0) acts as nucleating centers and nucleation within surface cavity of the micelle helps to form well dispersed AuNPs with ordered structures as the nanoparticles are entrapped by the surface cavity. But at low pH region, the bonding between the metal ion and surface cavity becomes weak and rate of reduction of metal ion decreases which in turns produce very few nucleating centers. This nucleating centers grows larger in size due to further reduction of metal ion on the surface of nucleating centers to form AuNPs. The utility of this study is that the growth, morphology and stabilization of AuNPs synthesized in aqueous P123 micellar solution can be modified through optimizing the pH value of the micellar solution.

7 Conclusion

The detail description of the sample preparation process and all the experimental techniques used to characterize the samples are discussed in Chapter 2. Each technique is presented here with the used experimental set-up along with its basic principles.

In chapter 3 we have represented the XR data of sol-gel derived silica films prepared with solutions of different solvent concentration and aged for different time interval and discussed about the structural differences obtained from electron density profiles of the data. The chapter is arranged with the discussion on the experimental details together with the results and discussion. The electron density profile suggests that all the films are made of woolen ball like structures though the attachment and thickness of the films is different depending on solution conditions. The thickness and attachment of the film increases with the decrease of solvent concentration and increase of duration of aging time of the silica solution. The porosity which is related to average electron density of the film increases with the increase of solvent concentration and duration of aging time of the silica solution.

The structural study of different mesostructures in the form of thin film depending upon different solution condition and different substrate surface condition together with the stability of such mesostructures upon surfactant removal process have been explored in Chapter 4. To understand these topics in details the chapter is sectionalized into three major parts, structural evolution of evaporation-induced self-assembled CTAB-silica mesostructured films with variation of CTAB/silica molar ratio, substrate and drying effect in shape and ordering of micelles inside CTABsilica mesostructured

films and finally the effect of surfactant removal on the CTABsilica mesostructured films. Each section includes discussion on the experimental details together with the results and discussion. In section 4.1 formation of different mesostructures was observed by varying only the CTAB/silica molar ratio in the solution while others processing parameters were kept constant. Analyzing the XR and GISAXS data and comparing the results with the literatures, the mesostructures prepared with CTAB/silica molar ratio 0.10 and 0.19 were indexed to 2D-hexagonal mesostructure composed of cylindrical micelles and 3D-hexagonal mesostructure composed of spherical micelles, respectively. The effect of substrate surface condition and solvent concentration on the shape and arrangement of the micelles inside the CTAB-silica 2D-hexagonal mesostructured films was discussed in second section. Deviation from perfect 2D-hexagonal ($p6m$) structure, for the films prepared on hydrophilic OH- and hydrophobic H-terminated Si substrates by adding different amount of excess alcohol in the mixed solution of CTAB and silica, is observed from the combined XR and GISAXS measurements. Cylindrical shaped micelles, which are initially circular on hydrophilic OH-terminated Si substrate to form perfect 2D-hexagonal structure, become elliptical (extended along in-plane) on hydrophobic H-terminated Si substrate to form slightly compressed 2D-hexagonal structure due to different attachment of the film with the substrate. With time, due to the drying of the silica materials and its restricted movement along in-plane direction, films on both the substrates are compressed along out-of-plane direction only, to form observed centered rectangular ($c2mm$) structures. Also due to the asymmetric shrinkage, stress is developed, which deteriorates the ordering in the film. The final shape of the micelles, including silica coating layer, shows maximum and minimum deviations from circular shape inside the thick film on OH-Si substrate and the thin film on H-Si substrate, respectively, while the deviation in the shape of the micelles, which is of actual importance, seems to be maximum and minimum inside the thick film on H-Si substrate and the thin film on OH-Si substrate, respectively, determined essentially by substrate nature and initial silica wall thickness. In the third section we have discussed about the preparation of mesoporous silica film by removal of surfactant from the CTAB-silica mesostructured film by solvent extraction process. Surfactants were removed from the silica networks by

rinsing the films in acidic ethanol solution and the porosity and stability of the structure was confirmed by using X-ray scattering techniques.

In chapter 5 we have discussed about the initial nature of as-prepared Cl-terminated Si surface prepared by wet chemical process and its time evolution at ambient conditions. The chapter is sectionalized into two major parts and each part includes discussion on the experimental details together with the results and discussion. In the first section, the wettability or hydrophilicity of a Cl-terminated Si surface is examined both in macroscopic and microscopic level. Confirming the total coverage of Si substrate with Cl- atom, the weakly hydrophilic nature of such surface in macroscopic level is determined using CA measurement. To get information in microscopic level, CTAB-silica 2D-hexagonal mesostructured thin film was deposited on Cl-Si surface along with hydrophilic OH-Si and hydrophobic H-Si surface. The structural study using X-ray scattering techniques suggests quite a strong interaction between the film and the substrate and the weakly hydrophilic nature of the ClSi surface even on the molecular or microscopic level, which can be explained by considering the strong electronegativity of Cl- atom. Moreover, it is found that Cl-passivation is strongly dependent on the crystalline orientation of the Si substrate surface. In the second section, the stability and evolution of wetting behavior of Cl-terminated Si surface at ambient conditions with respect to time was investigated. Transition in the nature of Cl-Si surface from weakly hydrophilic toward weakly hydrophobic with time was found from CA measurements which provide information in macroscopic level. Electron density profiles of time evolved Cl-Si surface, obtained from XR measurements, suggest that such a transition is associated with the growth of less uniform oxide layer. Structures of CTAB-silica 2D-hexagonal mesostructured thin films on as-prepared and time-evolved Cl-Si substrates, obtained from XR and GISAXS measurements, confirms the transition in the nature of Cl-Si surface from weak-hydrophilic toward weak-hydrophobic in microscopic level and growth of less homogeneous oxide layer. The critical time of such a transition is about 50 h, which actually represents the stability or the critical time of Cl desorption and oxide growth of the Cl-Si surface at ambient conditions.

The influence of pH value of P123 aqueous solution on the formation and growth of

AuNPs in a single step synthesis process at room temperature is elaborately described in chapter 6. UV-vis spectroscopy technique was used to monitor $HAuCl_4$ + P123 + water ternary mixture as a function of time and to investigate the final state of the solution DLS and TEM measurements were carried out. The results suggest that both the formation mechanism and final morphology (shape and size) of the nanostructure composed of AuNPs and P123 micelle strongly depend on the pH value of P123 aqueous solution. At low pH value (6.5 - 9), reduction rate of gold ion is slow and independent AuNPs of larger size are formed. On the other hand, at high pH value (9.5 - 12) the reduction of gold ion is accelerated and formation of smaller nanoparticles entrapped within the P123 micelles takes place.

Bibliography

[1] P. Buffat and J. P. Borel, *Phys. Rev. A*, 1976, **13**, 2287.

[2] I. P. Batra, S. Ciraci, G. P. Srivastava, J. S. Nelson and C. Y. Fong, *Phys. Rev. B*, 1986, **34**, 8246.

[3] V. T. Johna, B. Simmonsa, G. L. McPhersonb and A. Bose, *Current Opinion in Colloid and Interface Science*, 2002, **7**, 288.

[4] C. J. Brinker, Y. Lu, A. Sellinger and H. Fan, *Adv. Mater*, 1999, **11**, 579.

[5] P. Alexandris, *Chemical Engineering Technology*, 2011, **34**, 15.

[6] J. Z. Zhang, Z. l. Wang, J. Liu, S. Chen and G. yu Liu, *Self-Assembled Nanostructures*, Kluwer Academic, New York, 2004.

[7] R. Zana, *Dynamics of surfactant self-assemblies*, CRC Press, Taylor and Francis Group, 2005.

[8] Y. S. Lee, *Self-assembly and Nanotechnology: A Force Balance Approach*, John Wiley, NJ, 2008.

[9] G. J. de A. A. Soler-Illia, C. Sanchez, B. Lebeau and J. Patarin, *Chemical Reviews*, 2002, **102**, 4093.

[10] U. Ciesla and F. Schu, *Microporous and Mesoporous Materials*, 1999, **27**, 131.

[11] U. H. Lee, M. H. Kim and Y. U. Kwon, *Bull. Korean Chem. Soc*, 2006, **27**, 809.

[12] D. Grosso, F. Cagnol, G. J. de A. A. Soler-Illia, E. L. Crepaldi, H. Amenitsch, A. Brunet-Bruneau, A. Bourgeois and C. Sanchez, *Adv. Func. Mater.*, 2004, **14**, 309.

[13] S. Yua, T. K. S. Wonga, X. Hub and T. K. Goh, *Thin Solid Films*, 2004, **462463**, 306.

[14] L. Hench and J. K. West, *Chem. Rev.*, 1990, **90**, 33.

[15] C. J. Brinker and G. W. Scherer, *Sol-gel science: The physics and chemistry of sol-gel processing*, Academic press inc., USA, 1990.

[16] C. J. Brinker, A. J. Hurd, P. R. Schunk, G. C. Frye and C. S. Ashley, *Journal of Non-Crystalline Solids*, 1992, **147 and 148**, 424.

[17] Y. Y. Huang and K. S. Chou, *Ceramics International*, 2003, **29**, 485.

[18] S. Yua, T. K. S. Wonga, X. Hub and K. Pita, *Thin Solid Films*, 2004, **311**, 462463.

[19] C. Brinker and A. J. Hurd, *Journal de Physique III*, 1994, **4**, 1231.

[20] C. McDonagh, F. Sheridan, T. Butler and B. MacCraith, *Journal of Non-Crystalline Solids*, 1996, **194**, 72.

[21] S. P. Mukherjee, *Journal of Non-Crystalline Solids*, 1980, **42**, 477.

[22] E. J. A. Pope and J. D. Mackenzie, *Journal of Non-Crystalline Solids*, 1986, **87**, 185.

[23] C. Brinker, *Journal of Non-Crystalline Solids*, 1988, **100**, 31.

[24] R. A. Assink and B. D. Kay, *Journal of Non-Crystalline Solids*, 1988, **99**, 359.

[25] J. C. Pouxviel and J. P. Boilot, *Journal of Non-Crystalline Solids*, 1987, **89**, 345.

[26] J. Estella, J. C. Echeverria, M. Laguna and J. J. Garrido, *Journal of Non-Crystalline Solids*, 2007, **353**, 286.

[27] Y. Takata, T. Norisuye, S. Hirayama, T. Takemori, Q. T. C. Miyata and S. Nomura, *Macromolecules*, 2007, **40**, 3773.

[28] R. Gupta, S. Mozumdar and N. K. Chaudhury, *Biosensors and Bioelectronics*, 2005, **21**, 549.

[29] M. A. Fardad, E. M. Yeatman, E. J. C. Dawnay, M. Green and F. Horowitz, *Journal of Non-Crystalline Solids*, 1995, **183**, 260.

[30] P. M. Glaser and C. G. Pantano, *Journal of Non-Crystalline Solids*, 1984, **63**, 209.

[31] W. C. Ee and K. Y. Cheong, *Physica B*, 2008, **403**, 611.

[32] G. Wu, J. Wang, J. Shen, T. Yang, Q. Zhang, B. Zhou, Z. Deng, F. Bin, D. Zhou and F. Zhang, *Journal of Non-Crystalline Solids*, 2000, **275**, 169.

[33] M. M. Collinson, H. Wang, R. Makote and A. Khramov, *Journal of Electroanalytical Chemistry*, 2002, **519**, 65.

[34] P. Innocenzi, L. Malfatti, T. Kidchob and P. Falcaro, *Chem. Mater.Review*, 2009, **21**, 2555.

[35] J. S. Beck, J. C. Vartuli, W. J. Roth, M. E. Leonowicz, C. T. Kresge, K. D. Schmitt, C. T. W. Chu, D. H. Olson, E. W. Sheppard, S. B. McCullen, J. B. Higgins and J. L. Schlenker, *J. Am. Chem. Soc.*, 1992, **114**, 10834.

[36] C. T. Kresge, M. E. Leonowicz, W. J. Roth, J. C. Vartuli and J. S. Beck, *Nature*, 1992, **359**, 710.

[37] H. Yang, N. Coombs, I. Sokolov and G. A. Ozin, *Nature*, 1996, **381**, 589.

[38] H. Yang, A. Kuperman, N. Coombs, S. Mamiche-Afara and G. A. Ozin, *Nature*, 1996, **379**, 703.

[39] Y. Lu, H. Fan, A. Stump, T. L. Ward, T. Rieker and C. J. Brinker, *Nature*, 1999, **398**, 223.

[40] L. Nicole, C. Boissiere, D. Grosso, A. Quach and C. Sanchez, *J. Mater. Chem.*, 2005, **15**, 3598.

[41] Y. Wan and D. Zhao, *Chemical Reviews*, 2007, **107**, 2821.

[42] X. Zhang, W. Wu, J. Wang and C. Liu, *Thin Solid Films*, 2007, **515**, 8376.

[43] H.-P. Lin, C.-P. Kao, C.-Y. Mou and S.-B. Liu, *J. Phys. Chem. B*, 2000, **104**, 7885.

[44] H.-P. Lin and C.-Y. Mou, *Acc. Chem. Res.*, 2002, **35**, 927.

[45] D. A. Doshi, A. Gibaud, V. Goletto, M. Lu, H. Gerung, B. Ocko, S. M. Han and C. J. Brinker, *J. Am. Chem. Soc.*, 2003, **125**, 11646.

[46] S. Besson, T. Gacoin, C. Ricolleau, C. Jacquiod and J.-P. Boilot, *J. Mater. Chem.*, 2003, **13**, 404.

[47] M. Matheron, A. Bourgeois, A. Brunet-Bruneau, P. A. Albouy, J. Biteau, T. Gacoin and J.-P. Boilot, *J. Mater. Chem.*, 2005, **15**, 4741.

[48] F. Cagnol, D. Grosso, G. J. A. A. Soler-Illia, E. L. Crepaldi, F. Babonneau, H. Amenitsch and C. Sanchez, *J. Mater. Chem.*, 2003, **13**, 61.

[49] K. J. Edler, T. Brennan, S. J. Roser, S. Mann and R. M. Richardson, *Microporous and Mesoporous Materials*, 2003, **62**, 165.

[50] D. A. Doshi, A. Gibaud, N. Liu, D. Sturmayr, A. P. Malanoski, D. R. Dunphy, H. Chen, S. Narayanan, A. MacPhee, J. Wang, S. T. Reed, A. J. Hurd, F. Swol and C. J. Brinker, *J. Phys. Chem. B*, 2003, **107**, 7683.

[51] S. Liu, P. Cool, O. Collart, P. V. D. Voort, E. F. Vansant, O. I. Lebedev, G. V. Tendeloo and M. Jiang, *J. Phys. Chem. B*, 2003, **107**, 10405.

[52] A. Chougnet, C. Heitz, E. Sndergard, J. M. Berquier, P. A. Albouyb and M. Klotz, *J. Mater. Chem.*, 2005, **15**, 3340.

[53] S. H. Tolbert, T. E. Schaffer, J. Feng, P. K. Hansma and G. D. Stucky, *Chem. Mater*, 1997, **9**, 1962.

[54] H. Yang, N. Coombs, I. Sookolv and G. A. Ozin, *J. Mater. Chem.*, 1997, **7**, 1285.

[55] J. K. Bal and S. Hazra, *Phys. Rev. B*, 2007, **75**, 205411.

[56] P. Chatterjee, S. Hazra and H. Amenitsch, *Soft Matter*, 2012, **8**, 2956.

[57] P. Chatterjee and S. Hazra, *Soft Matter*, 2013, **9**, 9799.

[58] J. K. Bal and S. Hazra, *Phys. Rev. B*, 2009, **79**, 155412.

[59] J. K. Bal, S. Kundu and S. Hazra, *Phys. Rev. B*, 2010, **81**, 045404.

[60] J. K. Bal, S. Kundu and S. Hazra, *Chem. Phys. Lett.*, 2010, **500**, 90.

[61] J. K. Bal, S. Kundu and S. Hazra, *Eur. Phys. J. E*, 2012, **35**, 79.

[62] H. F. Okorn-Schmidt, *IBM J. Res. Dev.*, 1999, **43**, 351.

[63] X. G. Zhang, *Electrochemistry of Silicon and its Oxide*, Kluwer Academic, New York, 2004.

[64] Y. Dan, K. Seo, K. Takei, J. H. Meza, A. Javey and K. B. Crozier, *Nano Lett.*, 2011, **11**, 2527.

[65] S. Hazra, A. Gibaud, A. Desert, V. Gacem and N. Cowlam, *Physica B*, 2000, **283**, 45.

[66] M. K. Mukhopadhyay, M. K. Sanyal, A. Datta, J. Webster and J. Penfold, *Chem. Phys. Lett.*, 2005, **407**, 276.

[67] D. K. Schwartz, J. Garnaes, R. Viswanathan and J. A. Zasadzinski, *Science*, 1992, **257**, 508.

[68] R. J. Archer, *J. Electrochem. Soc.*, 1957, **104**, 619.

[69] F. Lukes, *Surf. Sci.*, 1972, **30**, 91.

[70] S. I. Raider, R. Fitsch and M. J. Palmer, *J. Electrochem. Soc.*, 1975, **112**, 413.

[71] H. R. Philip and E. A. Taft, *J. Appl. Phys*, 1982, **53**, 5224.

[72] E. A. Taft, *J. Electrochem. Soc*, 1988, **135**, 1022.

[73] D. J. Monk, D. S. Soane and R. T. Howe, *J. Electrochem. Soc*, 1993, **140**, 2339.

[74] K. Osseo-Asare, *J. Electrochem. Soc*, 1996, **143**, 1339.

[75] *Periodic Table of Elements*, `http://www.ptable.com`.

[76] *Wired Chemist*, `http://www.wiredchemist.com`.

[77] X. Zhang, E. Garfunkel, Y. J. Chabal, S. B. Christman and E. E. Chaban, *Appl. Phys. Lett.*, 2001, **79(24)**, 4051.

[78] G. W. Trucks, K. Raghavachari, G. S. Higashi and Y. J. Chabal, *Phys. Rev. Lett.*, 1990, **65**, 504.

[79] T. Miura, M. Niwano, D. Shoji and N. Miyamoto, *J. Appl. Phys.*, 1996, **79(8)**, 4373.

[80] H. Ikeda, Y. Nakagawa, M. Toshima, S. Furuta, S. Zaima and Y. Yasuda, *Appl. Surf. Sci.*, 1997, **117-118**, 109.

[81] K. A. Perrine and A. V. Teplyakov, *Chem. Soc. Rev.*, 2010, **39**, 3256.

[82] F. A. Soria, E. M. Patrito and P. Paredes-Oliverai, *Langmuir*, 2011, **27**, 2613.

[83] S. Rivillon, F. Amy, Y. J. Chabal and M. M. Frank, *Appl. Phys. Lett.*, 2004, **85**, 2583.

[84] S. Rivillon, Y. J. Chabal, L. J. Webb, D. J. Michalak, N. S. Lewis, M. D. Halls and K. Raghavachari, *J. Vac. Sci. Technol. A*, 2005, **23**, 1100.

[85] C. Y. Ruan, V. A. Lobastov, F. Vigliotti, S. Chen and A. H. Zewail, *Science*, 2004, **304**, 80.

[86] P. L. Silvestrelli, F. Toigo and F. Ancilotto, *J. Phys. Chem. B*, 2006, **110**, 12022.

[87] P. L. Silvestrelli, F. Toigo and F. Ancilotto, *J. Phys. Chem. C*, 2009, **113**, 17124.

[88] S. Rivillon, R. T. Brewer and Y. J. Chabal, *Appl. Phys. Lett.*, 2005, **87**, 173118.

[89] B. J. Eves and G. P. Lopinski, *Surf. Sci.*, 2005, **579**, L89.

[90] L. J. Webb, D. J. Michalak, J. S. Biteen, B. S. Brunschwig, A. S. Y. Chan, D. W. Knapp, H. M. Meyer, E. J. Nemanick, M. C. Traub and N. S. Lewis, *J. Phys. Chem. B*, 2006, **110**, 23450.

[91] S. Chen, C. Guo, G. H. Hu, J. Wang, J. H. Ma, X. F. Liang, L. Zheng and H. Z. Liu, *Langmuir*, 2006, **22**, 9704.

[92] X. Ji, X. Song, Y. Bai, W. Yang and X. Peng, *J. Am. Chem. Soc*, 2007, **129**, 13939.

[93] K. Rahme, F. Gauffre, J. D. Marty, B. Payre and C. Mingotuad, *J. Phys. Chem. C*, 2007, **111**, 7273.

[94] B. K. Pong, H. I. Elim, J. X. Chong, W. Ji, B. L. Trout and J. Y. Lee, *J. Phys. Chem. C*, 2007, **111**, 6281.

[95] H. Koerner, R. I. MacCuspie, K. Park and R. A. Vaia, *Chem. Mater*, 2012, **24(6)**, 981.

[96] T. S. Sabir, D. Yan, J. R. Milligan, A. W. Aruni, K. E. Nick, R. H. Ramon, J. A. Hughes, Q. Chen, R. Kurti and C. C. Perry, *J. Phys. Chem. C*, 2012, **116**, 4431.

[97] R. A. Caruso, M. Ashokkumar and F. Grieser, *Langmuir*, 2002, **18**, 7831.

[98] T. Ishii, H. Otsuka, K. Kataoka and Y. Nagasaki, *Langmuir*, 2004, **20**, 561.

[99] T. Sakai and P. Alexandris, *Langmuir*, 2004, **20**, 8426.

[100] T. Sakai and P. Alexandris, *J. Phys. Chem. B*, 2005, **109**, 7766.

[101] T. Sakai and P. Alexandris, *Langmuir*, 2005, **21**, 8019.

[102] D. Ray, V. K. Aswal and J. Kohlbrecher, *Langmuir*, 2011, **27**, 4048.

[103] S. Mandal, C. Ghatak, V. G. Rao, S. Ghosh and N. Sarkar, *J. Phys. Chem. C*, 2012, **116**, 5585.

[104] P. Khullar, V. Singh, A. Mahal, H. Kumar, G. Kaur and M. S. Bakshi, *J. Phys. Chem. C*, 2013, **117**, 3028.

[105] P. Khullar, A. Mahal, V. Singh, T. S. Banipal, G. Kaur and M. S. Bakshi, *Langmuir*, 2010, **26(13)**, 11363.

[106] P. Khullar, V. Singh, A. Mahal, H. Kaur, V. Singh, T. S. Banipal, G. Kaur and M. S. Bakshi, *J. Phys. Chem. C*, 2011, **115**, 10442.

[107] D. Ray, V. K. Aswal and D. Srivastava, *J. Nanosci. Nanotechnol.*, 2010, **10**, 6356.

[108] D. Ray and V. K. Aswal, *J. Macromol. Sci. B*, 2010, **49:4**, 810.

[109] Q. Shou, C. Guo, L. Yang, L. Jia, C. Liu and H. Liu, *J. Colloid Interface Sci.*, 2011, **363**, 481.

[110] A. G. Emslie, F. T. Bonner and L. G. Peck, *J. Appl. Phys*, 1958, **29**, 858.

[111] A. Acrivos, M. J. Shah and E. E. Petersen, *J. Appl. Phys.*, 1960, **31**, 963.

[112] D. Meyerhofer, *J. Appl. Phys.*, 1978, **49**, 3993.

[113] R. W. James, *The Optical Principles of the Diffraction of X-Rays*, Bell and sons, London, 1948.

[114] J. Daillant and A. Gibaud, *X-ray and Neutron Reflectivity: Principles and Applications*, Springer, London, 1999.

[115] L. D. Landau and E. M. Lifshitz, *Electrodynamics of continuous media: Course of Theoretical Physics: vol 8*, Pergamon, Oxfordon, 1960.

[116] M. Tolan, *X-ray Scattering from Soft-Matter Thin Films*, Springer, Berlin, 1999.

[117] T. P. Russel, *Mat. Sci. Rep.*, 1990, **5**, 171.

[118] A. Gibaud and S. Hazra, *Current Science*, 2000, **78**, 1467.

[119] J. A. Nielsen and D. McMorrow, *Elements of Mordern X-ray Physics*, Wiley, England, 2001.

[120] J. K. Basu and M. K. Sanyal, *Phys. Rep.*, 2002, **363**, 1.

[121] L. G. Parratt, *Phys. Rev.*, 1954, **95**, 359.

[122] S. K. Sinha, E. B. Sirota, S. Garoff and H. B. Stanley, *Phys. Rev. B*, 1988, **38**, 2297.

[123] M. Piecuch and L. Nevot, *Mat. Sci. Forum*, 1990, **59-60**, 93.

[124] T. A. Ezquerra, M. C. Garcya-Gutierrez, A. Nogales and M. A. Gomez, *Applications of Synchrotron Light to Scattering and Diffraction in Materials and Life Sciences*, Springer, 2009.

[125] H. Saisho and Y. Gohshi, *Applications of Synchrotron Radiation to Materials Analysis: vol 7*, Elsevier, 1996.

[126] W. Brown, *Dynamic Light Scattering: The Method and Some Applications*, Oxford, 1993.

[127] W. Brown, *Light Scattering: Principles and Development*, Oxford, 1996.

[128] B. J. Berne and R. Pecora, *Dynamic Light Scattering*, Dover Publications, New York, 2000.

[129] T. Young, *Philos. Trans. R. Soc. Lond.*, 1805, **95**, 65.

[130] Y. Yuan and T. Lee, *Surface Science Techniques*, Springer, 2013.

[131] C. D. Volpe, D. Maniglio, S. Siboni and M. Morra, *Oil and Gas Science and Technology Rev. IFP*, 2001, **56**, 9.

[132] R. Tadmor and P. S. Yadav, *J. Colloid Interf. Sci.*, 2008, **317**, 241.

[133] R. Tadmor, *Soft Matter*, 2011, **7**, 1577.

[134] R. Tadmor, *Langmuir*, 2004, **20**, 7659.

[135] A. M. Fox, *Optical Properties of Solids*, Oxford University Press, Oxford, 2003.

[136] C. N. Banwell and E. M. McCash, *Fundamentals of Molecular & Spectroscopy*, Tata McGraw-Hill, 2008.

[137] W. P. Halperin, *Rev. Mod. Phys.*, 1986, **58**, 533.

[138] U. Kreibig and M. Vollmer, *Optical Properties of Metal Clusters*, Springer, Berlin, 1995.

[139] C. Snnichsen, T. Franzl, T. Wilk, G. von Plessen and J. Feldmann, *New J. Phys*, 2002, **4**, 93.

[140] J. J. Mock, M. Barbic, D. R. Smith, D. A. Schultz and S. Schultz, *J. Chem. Phys.*, 2002, **116**, 6755.

[141] J. Muller, C. Sonnichsen, H. von Poschinger, G. von Plessen, T. A. Klar and J. Feldmann, *Appl. Phys. Lett.*, 2002, **81**, 171.

[142] P. Mulvaney, *Langmuir*, 1996, **12**, 788.

[143] K. Siegbahn, *Rev. Mod. Phys.*, 1982, **54**, 709.

[144] S. Hufner, *Photoelectron Spectroscopy: Principles and Application*, Springer, Heidelberg, 2003.

[145] B. Fultz and J. Howe, *Transmission Electron Microscopy and Diffractometry of Materials*, Springer, Berlin, 2008.

[146] L. Reimer and H. Kohl, *Transmission Electron Microscopy: Physics of Image Formation*, Springer, Berlin, 2008.

[147] Q. Liu, J. Zhang, Q. Liu, Z. Zhu and J. Chen, *Materials Chemistry and Physics*, 2009, **114**, 309.

[148] W. L. Warren, P. M. Lenahan, C. J. Brinker, C. S. Ashley, S. T. Reed and G. R. Shafferb, *American Institute of Physics*, 1991, **69(8)**, 4404.

[149] C. J. Brinker, G. C. Frye, A. J. Hurd and C. S. Ashley, *Thin Solid Films*, 1991, **201**, 97–108.

[150] M. Yamane, S. Inoue and A. Yasumori, *Journal of Non-Crystalline Solids*, 1984, **63**, 13.

[151] M. W. Colby, A. Osaka and J. Mackenzie, *Journal of Non-Crystalline Solids*, 1986, **82**, 37.

[152] H. Schmidt, H. Scholze and A. Kaiser, *Journal of Non-Crystalline Solids*, 1984, **63**, 1.

[153] J. S. Beck, J. C. Vartuli, W. J. Roth, C. T. K. M. E. Leonowicz, K. D. Schmitt, C. T. W. Chu, D. H. Olson and E. W. Sheppard, *J. Am. Chem. Soc.*, 1992, **114**, 10834.

[154] Y. Lu, R. Ganguli, C. A. Drewien, M. T. Anderson, C. J. Brinker, W. Gong, Y. Guo, H. Soyez, B. Dunn, M. H. Huang and J. I. Zink, *Nature*, 1997, **389**, 364.

[155] A. Gibaud, D. Grosso, B. Smarsly, A. Baptiste, J. F. Bardeau, F. Babonneau, D. A. Doshi, Z. Chen, C. J. Brinker and C. Sanchez, *J. Phys. Chem. B*, 2003, **107**, 6114.

[156] Q. Huo, D. I. Margolese and G. D. Stucky, *Chem. Mater.*, 1996, **8**, 1148.

[157] A. Gibaud, S. Dourdain, O. Gang and B. M. Ocko, *Phys. Rev. B*, 2004, **70**, 161403(R).

[158] M. Matheron, T. Gacoin and J.-P. Boilot, *Soft Matter*, 2007, **3**, 223.

[159] S. Manne, J. P. Cleveland, H. E. Gaub, G. D. Stucky and P. K. Hansma, *Langmuir*, 1994, **10**, 4409.

[160] S. Manne and H. E. Gaub, *Science*, 1995, **270**, 1480.

[161] L. M. Grant and W. A. Ducker, *J. Phys. Chem. B*, 1997, **101**, 5337.

[162] L. M. Grant, F. Tiberg and W. A. Ducker, *J. Phys. Chem. B*, 1998, **102**, 4288.

[163] J. F. Liu and W. A. Ducker, *J. Phys. Chem. B*, 1999, **103**, 8559.

[164] M. J. Rosen, *Surfactants and Interfacial Phenomena*, John Wiley, NJ, 2004.

[165] A. Imanishi, M. Suzuki and Y. Nakato, *Langmuir*, 2007, **23**, 12966.

[166] J. K. Bal and S. Hazra, *Phys. Rev. B*, 2009, **79**, 155412.

[167] M. Klotz, P.-A. Albouy, A. Ayral, C. Menager, D. Grosso, A. V. der Lee, V. Cabuil, F. Babonneau and C. Guizard, *Chem. Mater.*, 2000, **12**, 1721.

[168] Q. Huo, D. I. Margolese, U. Ciesla, D. G. Demuth, P. Feng, T. E. Gier, P. Sieger, A. Firouzi, B. F. Chmelka, F. Schuth and G. D. Stucky, *Chem. Mater.*, 1994, **6**, 1176.

[169] Y. Wan and D. Zhao, *Chem. Rev.*, 2007, **107**, 2821.

[170] Z. Hua, J. Shi, L. Wang and W. Zhang, *Journal of Non-Crystalline Solids*, 2001, **292**, 177.

[171] N. Chemin, M. Klotz, V. Rouessac, A. Ayral and E. Barthel, *Thin Solid Films*, 2006, **495**, 210.

[172] K. C. Hsu, K. J. Chao, S. F. Chen, H. K. Li and P. Y. Wu, *Thin Solid Films*, 2008, **517**, 686.

[173] J. Zasadzinski, R. Viswanathan, L. Madsen, J. Garnaes and D. Schwartz, *Science*, 2004, **263**, 1726.

[174] M. M. Stevens and J. H. George, *Science*, 2005, **310**, 1135.

[175] S. Koynov, M. S. Brandt and M. Stutzmann, *Appl. Phys. Lett.*, 2006, **88**, 203107.

[176] J. M. Buriak, *Chem. Rev.*, 2002, **102**, 1271.

[177] V. Derycke, P. G. Soukiassian, F. Amy, Y. J. Chabal, M. D. Dangelo, H. B. Enriquez and M. G. Silly, *Nat. Mater.*, 2003, **2**, 253.

[178] A. Bansal, X. Li, S. I. Yi, W. H. Weinberg and N. S. Lewis, *J. Phys. Chem. B*, 2001, **105**, 10266.

[179] P. G. de Gennes, *Rev. Mod. Phys.*, 1985, **57**, 827.

[180] J. Drelich, E. Chibowski, D. D. Meng and K. Terpilowski, *Soft Matter*, 2011, **7**, 9804.

[181] R. Tadmor, P. Bahadur, A. Leh, H. E. N'guessan, R. Jaini and L. Dangi, *Phys. Rev. Lett.*, 2009, **103**, 266101.

[182] J. K. Bal, S. Kundu and S. Hazra, *Chem. Phys.*, 2012, **406**, 72.

[183] J. K. Bal, S. Kundu and S. Hazra, *Mater. Chem. Phys.*, 2012, **134**, 549.

[184] M. J. Bedzyk, W. Gibson and J. A. Golovchenko, *J. Vac. Sci. Technol.*, 1982, **20**, 634.

[185] D. Ray, V. K. Aswal and D. Srivastava, *J. Nanosci. Nanotechnol.*, 2011, **11**, 1905.

[186] D. V. Goia and E. Matijevic, *Colloids and Surfaces A: Physicochemical and Enginnering Aspects*, 1999, **146**, 139.

[187] S. Wang, K. Qian, X. Z. Bi and W. Huang, *J. Phys. Chem. C*, 2009, **113**, 6505.

[188] I. O. Jimenez, F. M. Romero, N. G. Bsatus and V. Puntes, *J. Phys. Chem. C*, 2010, **114**, 1800.

[189] K. Torigoe and K. Esumi, *Langmuir*, 1992, **8**, 59.

[190] S. Ivanova, C. Petit and V. Pitchon, *Applied Catalysis A: General*, 2004, **267**, 191.

[191] L. Longenberger and G. Mills, *J. Phys. Chem.*, 1995, **99**, 475.

[192] J. K. Young, N. A. Lewinski, R. J. Langsner, L. C. Kennedy, A. Satyanarayan, V. Nammalvar, A. Y. Lin and R. A. Drezek, *Nanoscale Research Letters*, 2011, **6**, 428.

List of publications in journals

[1] Substrate and drying effect in shape and ordering of micelles inside CTAB-silica mesostructured films,

P. Chatterjee, S. Hazra and H. Amenitsch, *Soft Matter*, 2012, **8**, 2956.

[2] The hydrophilic/hydrophobic nature of a Cl-terminated Si surface,

P. Chatterjee and S. Hazra, *Soft Matter*, 2013, **9**, 9799.

[3] Time evolution of a Cl-terminated Si surface at ambient conditions,

P. Chatterjee and S. Hazra, *J. Phys. Chem. C*, 2014, **118**, 11350.

[4] pH effect on growth mechanism of gold nanoparticle in PEO- PPO - PEO triblock copolymer aqueous solution at ambient condition,

P. Chatterjee and S. Hazra, *communicated*.

List of corrections:

1 Page no. 80

With time, due to further polycondensation, those colloidal particles form an interconnected 3D network, called the gel. During film deposition by dip-coating or spin-coating, the polymeric or particulate inorganic precursors are concentrated on the substrate surface by a complex process involving gravitational draining with concurrent drying and continued condensation reactions.[149] The evaporation of the liquid phase during the drying of the layers of the film causes the colloidal particles to aggregate and form a network-like structure having some space, which is free from silica materials but usually filled up with low density water and/or hydrocarbon and thus can be referred as porous-like structure. Subsequent thermal treatment can remove the low density materials from the structure to form the actual porous silica film.

2 Page no. 89

The concentration of surfactant in the solution, which is kept below critical micellar concentration (cmc), changes with time due to evaporation to form aggregates (called micelles) of different shapes such as, spheres, cylinders, layers, etc.

3 Page no. 92

XR data of different mesostructured (for different CTAB/silica ratio) thick and thin films measured initially (after 15 h) are shown in Fig. 4.1.

4 Page no. 93

Figure 4.1: XR data of CTAB-silica 2D- and 3D-hexagonal mesostructured thick (a) and thin (b) films, for two different CTAB/silica ratio, deposited on OH-terminated Si(100) substrates, measured initially (after 15 h) (curves are shifted vertically for clarity).